



Scuola Politecnica e
delle Scienze di Base



Università degli Studi di Napoli Federico II
Dottorato di Ricerca in
Ingegneria Strutturale, Geotecnica e Rischio Sismico

THESIS FOR THE DEGREE OF DOCTOR OF PHILOSOPHY

Vibration-based SHM for structures and infrastructure: from damage assessment to optimal data management

by

ALESSANDRO LUBRANO LOBIANCO

Advisor: Prof. Marco Di Ludovico

Co-advisor: Ing. Marta Del Zoppo



SCUOLA POLITECNICA E DELLE SCIENZE DI BASE
DIPARTIMENTO DI STRUTTURE PER L'INGEGNERIA E L'ARCHITETTURA

*In the middle of difficulty
lies opportunity.*

VIBRATION-BASED SHM FOR STRUCTURES AND INFRASTRUCTURE: FROM DAMAGE ASSESSMENT TO OPTIMAL DATA MANAGEMENT

Ph.D. Thesis presented
for the fulfillment of the Degree of Doctor of Philosophy
in Ingegneria Strutturale, Geotecnica e Rischio Sismico
by

ALESSANDRO LUBRANO LOBIANCO

March 2023



Approved as to style and content by

Prof. Marco Di Ludovico, Advisor

Ing. Marta Del Zoppo, Co-advisor

Università degli Studi di Napoli Federico II

Ph.D. Program in Ingegneria Strutturale, Geotecnica e Rischio Sismico

XXXV cycle - Chairman: Prof. Iunio Iervolino



www.dist.unina.it/dottorati-di-ricerca/dottorati

Candidate's declaration

I hereby declare that this thesis submitted to obtain the academic degree of Philosophiæ Doctor (Ph.D.) in Ingegneria Strutturale, Geotecnica e Rischio Sismico is my own unaided work, that I have not used other than the sources indicated, and that all direct and indirect sources are acknowledged as references.

Parts of this dissertation have been published in international journals and/or conference articles

Napoli, March 10, 2023

Alessandro Lubrano Lobianco

Abstract

The aim of this thesis is to assess the impact of earthquake-induced damage on the modal properties of structures using experimental tests and numerical analysis, in order to quantify the damage through structural monitoring systems (SHM). The study covers various levels of structural complexity, ranging from reinforced concrete columns to 2D reinforced concrete frames with brick infills, as well as reinforced concrete buildings and bridge piles for monitoring bridges (BHM).

The thesis presents a methodology that correlates the variation of modal properties of a whole structure or a structural element with a pre-defined scale of damage, developed using both experimental and numerical approaches. The experimental approach is used to validate numerical models, in order to make a dataset of elements for estimating a matrix of correlation between frequency variation and damage level.

Additionally, the thesis proposes a methodology for managing, synthesizing, and transferring structural health monitoring data for bridges, which is validated through laboratory testing on a scale bridge and applied to seven existing viaducts.

The thesis constitutes a preliminary basis for the quantification of the damage seismic using structural vibration-based monitoring techniques and provides a methodological framework for managing data from the latter.

Keywords: Modal-based damage detection, frequency variation, OMA, Structural Health Monitoring.

Sintesi in lingua italiana

La tesi analizza la variazione delle proprietà modali delle strutture a seguito del danno indotto da sisma attraverso test sperimentali e analisi numeriche, al fine di quantificare il danno tramite sistemi di monitoraggio strutturale (SHM). Lo studio è condotto a diversi livelli di complessità strutturale, partendo da pilastri in cemento armato, per arrivare a telai piani in cemento armato con tamponature in laterizio, edifici in cemento armato e pile da ponte in cemento armato per il monitoraggio dei ponti (BHM). La tesi presenta una metodologia per correlare la variazione delle proprietà modali di una struttura o elemento strutturale con una predefinita scala di danno. La metodologia è sviluppata seguendo due diversi approcci: un approccio sperimentale e un approccio numerico. L'approccio sperimentale è utilizzato per validare i modelli numerici al fine di creare un dataset di elementi sui quali derivare una matrice di correlazione tra variazione di frequenza e livello di danno. Infine, la tesi propone una metodologia per la gestione, la sintesi e il trasferimento dei dati di monitoraggio dello stato di salute dei ponti. La metodologia di gestione dei dati è validata attraverso test di laboratorio su un ponte in scale e applicata a sette viadotti esistenti. La tesi costituisce una base preliminare per la quantificazione del danno sismico utilizzando tecniche di monitoraggio strutturale basate sulle vibrazioni, e offre un quadro metodologico per la gestione dei dati provenienti da quest'ultimo.

Parole chiave: Monitoraggio strutturale, Analisi Modale Operazionale, variazione delle frequenze, quantificazione del danno.

Contents

Abstract	i
Sintesi in lingua italiana	ii
Acknowledgements	vi
List of Figures	xiv
List of Tables	xvii
1 Introduction	1
1.1 Objectives	5
1.2 Outlines	5
2 An overview of vibration-based SHM	7
2.1 Modal identification and damage detection	18
2.2 Modal Identification Techniques	23
2.3 Output-only modal identification methods	27
2.3.1 Time Domain Methods	27
2.3.2 Frequency Domain Methods	29
3 Correlation between modal parameters and damage: methodology	37
3.1 Seismic damage scales for damage quantification	40
3.1.1 Structural damage	40

3.1.2	Non-structural damage	42
3.2	Experimental approach	43
3.2.1	RC Columns	44
3.2.2	RC Frame	47
3.3	Numerical approach	48
4	Correlation between modal parameters and damage: experimental tests and numerical analyses	51
4.1	RC Columns	51
4.1.1	Experimental study	51
4.2	Numerical study	57
4.3	RC Frame	70
4.3.1	Experimental study	70
4.3.2	Numerical study	79
4.4	RC Buildings	88
4.4.1	Numerical study	88
4.5	RC bridge piers	93
4.5.1	Numerical study	93
5	A proposal of SHM and data management for bridges	107
5.1	Introduction	107
5.2	Architecture of SHM and data management	109
5.3	Sensors for monitoring system	115
5.4	Accelerometers layout optimization	133
6	Bridge Health Monitoring: case studies	135
6.1	Laboratory test for validation	136
6.2	Brin bridge	138
6.3	Volturmo bridge	141
6.4	Viaduct n.1011	144
6.5	San Gennaro Viaduct	151

6.6	Sant'Eframo viaduct	157
6.7	Viaduct n.0080	162
6.8	Viaduct n.1028	166
6.9	Viaduct n.1026	169
6.10	Cassiodoro viaduct	170
7	Conclusions	179
	Bibliography	191

Acknowledgements

The author's work has been carried out in the framework of the PRIN 2017 (Progetti di Rilevante Interesse Nazionale) project "Life-long optimized structural assessment and proactive maintenance with pervasive sensing techniques", grant nr. 20172LHSEA

List of Figures

2.1	The collapse of the “Polcevera” viaduct	8
2.2	Example of under sampled signal (red line is original signal, blue line is measured signal)	25
2.3	Sample singular values plots	33
2.4	Sample of time domain free decay obtained by inverse FFT and estimated damping envelope	34
3.1	Methodological framework	39
3.2	Scheme of methodology framework for buildings	41
3.3	Experimental methodological framework	44
3.4	Experimental setup for the quasi-static cyclic loading tests (a) and displacement loading sequence (b).	45
3.5	Front view of one full-scale RC frame with the pseudo- dynamic test setup.	47
3.6	Assessment of the lateral stiffness for each imposed IDR. . .	49
3.7	Numerical methodological framework for RC columns/piers.	49
4.1	Geometry and reinforcement details of the tested specimens (A and B), dimensions in mm.	52
4.2	Seismic damage simulation: configurations C_1 (a) and C_2 (b).	53

4.3	Experimental setup for the cyclic pushover tests.	54
4.4	Uniaxial piezoelectric accelerometers layout for OMA tests in the strong (sensors S1 to S4) and weak direction (sensors 5 to 8), dimensions in mm	55
4.5	COMAC (a) and ECOMAC (b) for each control point of the experimental test of specimen B.	57
4.6	RC column modelling using distributed plasticity element.	58
4.7	Comparison between lateral stiffness from FEM model and experimental curves at $IDR = 0.40\%$	62
4.8	Comparison between numerical simulation and experimen- tal test for RC columns with plain rebars: (a) R300P-c, (b) R500P-c, (c) R500P-c-bis, (d) S300P-c.	63
4.9	Comparison between numerical simulation and experimen- tal test for RC columns with deformed rebars: (a) R300D-c, (b) R500D-c, (c) S300D-c.	63
4.10	Correlation between imposed IDR and Park and Ang dam- age index for the case-study columns (90 elements).	65
4.11	Distribution of period elongation for each damage level: a) DL1; b) DL2; c) DL3; d) DL4.	66
4.12	Ranges of variation of period elongation for each damage level.	67
4.13	Ranges of variation of residual drift ratios for each damage level and comparison with FEMA 356 thresholds.	67
4.14	Ranges of variation of stiffness degradation for each damage level.	69
4.15	Stiffness degradation from numerical analyses on the dataset and comparison with Di Ludovico et al. model for the stiff- ness modification factor	70
4.16	Modal shapes for the 2D RC frame specimens.	73
4.17	Accelerometers layout for OMA.	74

4.18	Damage condition at the end of the loading sequences for F2_3S_M and F2_4S_M.	75
4.19	a) 1st Singular value of PSD matrix and modal shape of test on F2_4S_M on undamaged configuration; b) 1st Singular value of PSD matrix and modal shape of test on F2_4S_M on damaged configuration	78
4.20	Schematic view of the FE model with 4-side infills walls . . .	83
4.21	Numerical vs experimental comparison of hysteretic curves.	84
4.22	Comparison of variation in natural frequency between bare and infilled frames with respect to peak ground acceleration.	87
4.23	Comparison between numerical and experimental frequencies for the in-plane vibration mode	88
4.24	a) Front view of the case study building and b) typical floor plant of the case study building.	89
4.25	Interstorey drift of each column for analysis with 150% intensity of ground shaking.	91
4.26	Correlation with the a) peak and b) averaged column DS and period variation of the building.	93
4.27	Structural scheme of examined bridge and loading scheme: longitudinal profile (a) and transverse profile (b).	95
4.28	Distribution of geometrical and mechanical parameters for the population of 200 RC bridge piers.	97
4.29	Comparison between numerical and experimental capacity curves for the selected eight tests.	101
4.30	Probability distribution of Δ_{f_1} as a function of the DR for the dataset of 200 piers.	103
4.31	a) Cumulative percentage of simulations for each damage level and b) number of simulations that reached a damage level in a certain range of frequency variation.	104

4.32	Probability of exceedance of each damage level as a function of Δ_{f_1}	105
4.33	COMAC (a) and ECOMAC (b) for control point at 0.3H from the base of the pier.	106
5.1	Scheme of architecture of the monitoring system	109
5.2	Example of management software interface of the main server	110
5.3	Example of time trend of damage characteristics of inclinometer's damage features time trend	112
5.4	Example of time trend of damage characteristics of accelerometer's damage features time trend.	112
5.5	Example of threshold estimated for piers bridge.	113
5.6	Capacitive accelerometer scheme	117
5.7	Operating principle of an accelerometer	118
5.8	Example of electroplating bars	121
5.9	Example of MEMS inclinometer	122
5.10	Examples of commercial ultrasonic thickness gauges	123
5.11	Linear Variable Differential Transducers	125
5.12	Internal structure of LVDT devices	126
5.13	Example of H-level sensors layout for monitoring subsidence in a building.	128
5.14	Picture of a typical weather station	129
5.15	Example of an analogue crackmeter.	130
5.16	Example of a digital crackmeter.	130
5.17	Example of a commercially available strain gauge.	131
5.18	Coupled configuration of strain gauges in order to purify errors due to temperature variations.	132
5.19	Accuracy on prediction of modal shapes with n.3 sensors.	133
5.20	Accuracy on prediction of modal shapes with n.5 sensors.	133
5.21	Accuracy on prediction of modal shapes with n.7 sensors.	134

5.22	Positioning and number of accelerometers taking into account the symmetry of the span.	134
6.1	Lateral view of the specimen bridge	136
6.2	Front view of the specimen bridge	137
6.3	Layouts of accelerometers for the OMA test of the specimen	137
6.4	Lateral view of the Brin viaduct	138
6.5	Cross section of the Brin viaduct, dimensions in cm	138
6.6	Layout of accelerometers for the BRIN bridge	139
6.7	Layout of inclinometers for the BRIN bridge	139
6.8	Layout of LVDTs for the BRIN bridge	140
6.9	Layout of pH sensor for the BRIN bridge	140
6.10	Accelerometers layout on the Volturno bridge	142
6.11	Inclinometers layout on the Volturno bridge	142
6.12	Extensometers layout on the Volturno bridge	143
6.13	Linear variable displacement transducers layout on the Volturno bridge	143
6.14	Picture of the viaduct n.1011	145
6.15	Lateral view of the viaduct n.1011	145
6.16	Plan view of the viaduct n.1011	146
6.17	Accelerometers layout on the viaduct n.1011 a) lateral view b) plan view	147
6.18	Inclinometers layout on the viaduct n.1011 a) lateral view b) plan view	148
6.19	Extensometers layout on the viaduct n.1011 a) lateral view b) plan view	149
6.20	LVDTs layout on the viaduct n.1011 a) lateral view b) plan view	150
6.21	Original project excerpts San Gennaro viaduct a) left lane b) right lane c) lateral section	152

6.22	Accelerometers layout for San Gennaro viaduct a) lateral view b) plan view	153
6.23	Inclinometers layout for San Gennaro viaduct a) lateral view b) plan view	154
6.24	Extensometers layout for San Gennaro viaduct a) lateral view b) plan view	155
6.25	LVDTs layout for San Gennaro viaduct a) lateral view b) plan view	156
6.26	Picture of Sant'Eframo Viaduct	157
6.27	Accelerometers layout of Sant'Eframo viaduct a) lateral view b) plan view.	158
6.28	Inclinometers layout of Sant'Eframo viaduct a) lateral view b) plan view.	159
6.29	Extensometers layout of Sant'Eframo viaduct a) lateral view b) plan view.	160
6.30	LVDTs layout of Sant'Eframo viaduct a) lateral view b) plan view.	161
6.31	Carpentry of the "Poggio di Capodimonte" viaduct.	162
6.32	Lateral view of the "Poggio di Capodimonte" viaduct.	163
6.33	Picture of the "Poggio di Capodimonte" viaduct.	163
6.34	Accelerometers layout of the "Poggio di Capodimonte" viaduct a) lateral view; b) plan view.	164
6.35	Inclinometers layout of the "Poggio di Capodimonte" viaduct a) lateral view; b) plan view.	164
6.36	Extensometers layout of the "Poggio di Capodimonte" viaduct a) lateral view; b) plan view.	165
6.37	LVDTs layout of the "Poggio di Capodimonte" viaduct a) lateral view; b) plan view.	165
6.38	Picture of Viaduct n.1028 "Manina".	166
6.39	Lateral and plan views of viaduct n.1028 "Manina".	166

6.40	Plan and lateral views of the accelerometers layout of the “Manina” viaduct.	167
6.41	Plan and lateral views of the inclinometers layout of the “Manina” viaduct.	167
6.42	Plan and lateral views of the extensometers layout of the “Manina” viaduct.	168
6.43	Plan and lateral views of the LVDTs layout of the “Manina” viaduct.	168
6.44	Picture of viaduct n.1026.	169
6.45	Lateral view of viaduct n.1026 from pier n.20 to pier n.44.	169
6.46	Lateral view of viaduct n.1026 from pier n.45 to pier n.49.	170
6.47	Plan view of viaduct n.1026.	170
6.48	Accelerometers layout of viaduct n.1026.(a) lateral view; (b)plan view	171
6.49	Inclinometers layout of viaduct n.1026.(a) lateral view; (b)plan view.	172
6.50	Extensometers layout of viaduct n.1026.(a) lateral view; (b)plan view.	173
6.51	LVDTs layout of viaduct n.1026.(a) lateral view; (b)plan view.	174
6.52	Picture of the “Cassiodoro” viaduct (from Google Earth).	175
6.53	Lateral views of the “Cassiodoro” viaduct.	175
6.54	Accelerometers layout of the “Cassiodoro” viaduct – lateral view.	176
6.55	Accelerometers layout of the “Cassiodoro” viaduct – plan view.	176
6.56	Inclinometers layout of the “Cassiodoro” viaduct – lateral view.	176
6.57	Inclinometers layout of the “Cassiodoro” viaduct – plan view.	177
6.58	Extensometer layout of the “Cassiodoro” viaduct – lateral view.	177
6.59	Extensometer layout of the “Cassiodoro” viaduct – plan view.	177

6.60	LVDTs layout of the “Cassiodoro” viaduct – lateral view. . .	178
6.61	LVDTs layout of the “Cassiodoro” viaduct – plan view. . . .	178

List of Tables

3.1	Damage scale and DI thresholds from Park et al. 1985	40
3.2	Correlation between IDR and damage level for RC columns	42
3.3	Description of damage levels for masonry walls considered in this study.	43
4.1	Summary of specimen configuration and relative damage. .	52
4.2	Seismic damage: experimental natural frequencies.	54
4.3	Geometric and mechanical parameters for selected tests on RC columns for model validation (*tests from Di Ludovico et al.	60
4.4	Load protocol for the cyclic pushover.	60
4.5	Variability of geometrical and mechanical properties in the dataset.	64
4.6	Parameters of lognormal distributions associated with the period elongation for DL.	66
4.7	Damage Levels classification based on the residual story drift ratio according to FEMA 356 and comparison with lower bound values from numerical results.	68
4.8	Test description for specimen F2.	72
4.9	Loading sequences.	73

4.10	Pseudo-dynamic test results and damage description for F2_3S_M (from Del Vecchio et al.)	76
4.11	Pseudo-dynamic test results and damage description for F2_4S_M (from Del Vecchio et al).	77
4.12	Summary of modal identification results via OMA for the first in-plane mode	80
4.13	Summary of modal identification results via OMA for the first out-of-plane mode	80
4.14	Beam-column joint backbone critical points.	81
4.15	Infill's backbone critical points.	82
4.16	Comparison between numerical and experimental frequencies for the in-plane mode.	85
4.17	Comparison between variation in frequencies in bare frame and infilled frame F2_3S_M.	87
4.18	Summary of global damage level and correlated period variation for the first loading scenario (1.00 X).	92
4.19	Summary of natural period variation ranges at different damage levels considering both peak and average value.	92
4.20	Statistics of relevant geometrical and mechanical properties of existing bridge piers.	96
4.21	Geometric and mechanical parameters of the RC columns for model calibration.	99
4.22	Comparisons between experimental and numerical natural frequencies.	100
4.23	Load protocol for the cyclic pushover.	102
4.24	Frequency variation probability functions parameters (μ and β) for each damage level.	105

5.1	Local space required for temporary storage of data to be processed for accelerometers, inclinometers, pH sensors and LVDTs.	115
5.2	Size of processed data to be transferred and archived, for accelerometers, inclinometers, pH sensors and LVDTs. . . .	115
5.3	Type of instruments and relative measurements	117
6.1	Summary of OMA test of specimen bridge	138

Chapter 1

Introduction

The science is a continuous spiral of discoveries. There are always new paths to tread, new things to observe, and new questions to ask.

Rachel Carson

Safety, durability and serviceability are requirements that a structure should meet during its lifetime. Damage in civil structures and infrastructure may occur from a plenty of causes. Structural damage can be associated with the deterioration of materials (i.e., ageing problems), fatigue, or extraordinary events such as fires, earthquakes, hurricanes, impact loads, among many others. The process of implementing a damage identification strategy is referred to as Structural Health Monitoring (SHM). SHM has become an important research discipline in several areas including civil engineering, with the goal of assessing the health condition of structures by monitoring their characteristics during the lifetime. The goal of SHM is to detect the structural damage, assessing the presence of damage, the location of damage, the damage severity, and estimating the remaining service life of a structure. A proper implementation of a SHM system can help in detecting the structural performance deterioration at an early stage, increasing the safety level, and bringing efficiency and effectiveness in maintenance operations. A current challenge in SHM is to correctly identify when variations obtained from monitoring data can be associated to a structural damage rather than to environmental noise, and to corre-

late such variations with a damage level associated to the serviceability of the structure. The recent advances in SHM make possible the remote assessment of the performance and health state of structures under service loads (traffic, wind, temperature, and so on) as well as exceptional loads, such as earthquakes, at the expenses of a moderate financial investment in measurement equipment and data processing software. Compared to traditional visual inspections, SHM offers attractive advantages, such as timely and remote detection of incipient damage conditions, and detection of hidden damage (e.g., possible cracks caused by an earthquake in the core concrete of columns in retrofitted bridges which are hidden by their jackets). Moreover, if global approaches are applied, damage can be detected even at locations characterized by limited accessibility. In addition, since the structural health assessment is based on real measures data and, another relevant pitfall of traditional inspections, i.e. the influence of the subjectivity of the expert judgement, is limited. The aim of Structural Health Monitoring (SHM) is to detect and monitor changes of a specific features of a building to assess the presence of damage and its location, severity and type [1]. The proper implementation of a monitoring system can help to detect the damage of structures at an early stage, increase the safety level and improve the efficiency and effectiveness of maintenance work, as well as identify the best option for the decision-maker [2]. Timely detection of degradation phenomena by SHM systems can provide a valuable contribution to shift the maintenance paradigm for bridges from scheduled (time based) to proactive (condition based) maintenance. In addition, SHM systems in earthquake prone regions can provide significant data and information to remotely assess the health state and serviceability of critical buildings and bridges right after the occurrence of a seismic event and, whenever they are severely damaged, they can support emergency management and quick decision making to reduce the risk of secondary losses. In particular, bridges are critical components of transportation infrastructure networks, and unattended damage or degradation phenomena can result in severe economic losses as well as consequences on public safety. In order to ensure that bridges are able to sustain the design loads (dead and live loads as well as extreme ones, such as those generated by earthquake) over their entire lifespan, appropriate maintenance to ensure structural integrity is required. The latter is typically evaluated by means of regular

visual inspections carried out by appropriately trained technical personnel. Results of inspections are usually collected into Bridge Management Systems (BMS) and used to make informed decisions regarding intervention strategies and can be complemented by detailed physical and mechanical measures taken according to the Structural Health monitoring (SHM) paradigm. In this thesis, a vibration-based SHM have been investigated to correlate the seismic damage features to a damage scale. In vibration-based SHM, the dynamic properties of a structure (i.e., mode shapes, natural periods) are monitored for the structural damage identification, localization and quantification. A widespread damage detection technique consists in processing the acceleration acquired through operational modal analysis (OMA) in the frequency domain (i.e., Fourier analysis). Indeed, dynamic properties are extremely sensitive to changes in the lateral stiffness of structures, and are commonly used as predictors for damage detection systems. In the context of vibration-based seismic damage quantification, the elongation of fundamental period is a widely adopted damage indicator to estimate the overall inelastic structural performance after earthquakes. In reinforced concrete (RC) structures, the period elongation is a function of the ground motion parameters as well as the materials and geometry of the structure and the presence of infill walls. Some studies experimentally assessed the changes in dynamic properties on a few structures affected by seismic damage using OMA data [3], and proposed period elongation ranges as a function of the level of damage experienced by such structures during a specific earthquake. However, a detailed framework for assessing the changes in dynamic properties as a function of the experienced damage level is currently missing, due to epistemic and aleatory uncertainties in the structural geometry and ground motion characteristics. The fundamental assumption is that damage affects the mass or stiffness properties of the monitored structure, so that it can be detected from the variations of the dynamic properties, that is to say, natural frequencies, mode shapes and modal damping ratios, over time. To this aim, the small amplitude operational response of the structure is automatically processed to extract selected damage sensitive features, and it is assumed that damage occurs as a discrete event, so that anomalies can be detected by comparing damage features before and after damage occurrence. When vibration based SHM is considered, modal properties are used as damage features either directly

or in the form of derived quantities, such as modal strain energy, mode shape curvature, dynamic flexibility, and so on. Natural frequencies have been extensively used for vibration-based SHM because they can be more easily and accurately measured than other modal-based damage sensitive features. However, while natural frequencies are effective in anomaly detection, they are of limited value for damage location. In addition, natural frequency estimates are sensitive to environmental and operational effects, that might jeopardize the reliability of damage detection in the absence of effective procedures for their compensation. In order to overcome the limitations associated with the use of natural frequencies as damage sensitive features, mode shapes (and derived parameters) are also considered for damage detection and localization. In this perspective, damage features based on mode shapes are particularly attractive because they are less influenced by environmental effects than natural frequencies, and they hold spatial information exploitable for damage localization. The first attempts of using mode shapes as damage sensitive features relied on the evaluation of the Modal Assurance Criterion (MAC) between couples of corresponding modes before and after damage occurrence. However, the MAC index is not very sensitive to local deviations of modal displacements and to small changes or small magnitude of modal displacements; so, the Coordinate Modal Assurance Criterion (CoMAC) has been introduced as an alternative. Applications of MAC and CoMAC to damage detection of structures revealed that they can detect most structural changes and locations, but also identify spurious damage. Even if CoMAC may yield false damage detections, it is still widely applied to SHM, sometimes in combination with other methodologies to improve performance. The literature review points out two main challenges in the application of vibration-based SHM: the first concerns the limited availability of monitoring data over wide time scales holding information about damage effect under varying environmental/operational conditions; the second challenge, instead, concerns the possibility of exploiting modal information not only for damage detection and localization, but also to get quantitative information about the structural performance and safety of the monitored structure. This aspect, rarely addressed by the scientific community, is of particular interest for SHM applications in earthquake prone regions, when prompt serviceability assessment of critical structures and infrastructure hit by the seismic

input might be critical for emergency management and shortening downtime implies significant economic savings.

1.1 Objectives

The thesis deals with the damage quantification for structures and infrastructure through SHM data. In detail, the objective of the thesis is to investigate a correlation between a damage scale that represents in a quantitative manner a state of damage in a generic structure and the variation of modal parameters of the structure itself (i.e., fundamental period or frequency, mode shapes, etc.). For this purpose, a methodology is developed to assess the variation in modal parameters of reinforced concrete (RC) buildings and bridges after seismic events of different intensities. Full-scale experimental tests on different structural components (e.g. RC columns and infilled RC frames) are carried out for validating finite element models in order to replicate the damage observed experimentally. This allows to create a dataset of numerical models with different geometrical and mechanical properties to define threshold values or ranges of variation of modal properties of buildings, building components and bridges for increasing seismic damage levels.

1.2 Outlines

A brief overview of Structural Health Monitoring (SHM) is presented in Chapter 2 to show the benefits and limitations of such a process, with particular emphasis on the aspect of damage quantification. Chapter 3 discusses the proposed methodology for estimating the correlation between the variations in the modal properties of structures and the seismic damage levels. Chapter 4 deals the results of the proposed methodology applied to RC columns, frames and buildings and bridge piers. As a conclusive part of the research activities, Chapter 5 outlines the design and testing of a long-term monitoring system on existing bridges, while the Chapter 6 shows an application on existings buildings managed by Nazionale Volturmo (EAV) and Tangenziale di Napoli (TaNA).

Chapter 2

An overview of vibration-based SHM

Experience is the hardest kind of teacher: it gives you the test first and the lesson afterward.

Oscar Wilde

Damage can be defined as a change introduced into the system that adversely affects its current and future performance. Implicit in this definition, the concept of damage is not meaningful without a comparison between two different states of the system, one of which is assumed to be the initial undamaged state. The changes introduced into the system involve changes in materials, geometric properties, boundary conditions boundary and constraint configuration, all of which adversely affect the performance of the system. In all structures, damage begins at the material level. Although it is not a universally accepted terminology, such damage is referred to as a defect or imperfection and is present, to varying degrees, in all materials. Such inherent defects in materials grow when the system is subjected to operating loads, so they can cause loss of efficiency of the structure. The term damage does not necessarily indicate a total loss of functionality of the structure but, rather, that the system is no longer operating optimally. With the growth of the damage will reach a situation where its effects are no longer acceptable to the users of the structure; this situation is referred to as structure collapse. Figure 2.1 shows



Figure 2.1. The collapse of the “Polcevera” viaduct

one of the most important collapses of our days, namely the collapse of a span of the bridge over the “Polcevera” River (Genova). From the point of view of time, the damage may accumulate incrementally over long periods, as with cases associated with corrosion or fatigue phenomena; or it can occur the short time lapses, as in the case of earthquakes. The process that implements damage identification in aerospace, mechanical, and civil engineering is referred to as Structural Health Monitoring (SHM). This process involves observations on structures or on mechanical systems, carried out through the periodic collection of measurements that allow the extraction of damage-sensitive features and the statistical analysis of these characteristics in order to determine the current health status of the system. The results of the analyses are updated periodically in order to be able to provide indications of how well the structure is able to perform the performance for which it was designed, even with the inevitable aging.

As discussed in Farrar and Worden [4], the structural monitoring process can be divided into four stages: operational evaluation; data acquisition, normalization and cleansing; feature selection and information condensation; statistical model development for feature discrimination. In particular, the operational assessment aims to answer four questions concerning the ability to identify damage and its future development. These questions are used to establish what is the most important damage that may affect the structure, what are the conditions, operational and environmental, faced by the monitoring system and any limitations and whether there are safety or economic reasons such as to perform a monitoring system. The operational evaluation begins to set limits on what is to be monitored and how monitoring is to be accomplished. This assessment begins

to characterize the process of damage identification, based on the peculiarities of the system to be monitored, seeking to gain knowledge about the characteristics of the damage that will need to be detected. Data acquisition involves the operational part of structural monitoring, which will have to deal with the selection of the excitation method, the type of sensors to be installed, their number and location, and data acquisition in hardware drive. At this stage, economic evaluations play an important role in the decisions that will be made. Another aspect to be considered is the data acquisition interval, which, of course, goes to influence the amount of storage space required for acquisition. Since data are collected under different conditions, it is essential to normalize them to uniquely identify the damage process. Since data can be measured under varying conditions, the ability to normalize the data becomes very important to the SHM process [5]. Normalization is the process of separating the changes introduced into the data collected by sensors caused by damage from those caused by environmental and operational variations. Various kinds of regression and interpolation analyses can be performed to relate measurements relevant to structural damage and those associated with environmental and operation variation of the system [6, 7, 8, 9]. When environmental and operational conditions are a problem, the need arises to normalize data in time frames subject to the same operational cycles and similar environmental conditions so that comparisons of measurements made can be made. It should be noted that not all sources of variability can be removed so not all data can be normalized. Even when normalization of data is not possible, a statistical study of how operating and environmental conditions affect the responses of the monitoring instrumentation should still be carried out [10, 11]. Data cleaning is a process of selectively choosing data to go through the process of extracting structure characteristics. Cleanliness depends on the mode and experience of those performing the acquisitions. The structural monitoring field of study of major interest in literature is the identification of features, which allow to define the difference between undamaged and damaged structures. One of the most common methods of feature extraction is based on the correlation of quantities measured by the system, such as frequency or modal shapes, with first-hand observation of the state of degradation. Another method of feature extraction for damage identification is to apply engineering defects, similar to those

expected in the structure under operating conditions, to dummy systems and develop an initial understanding of the parameters sensitive to the expected damage. The damaged system can be used to verify that the diagnostic measurements are sufficiently sensitive in distinguishing between damaged and undamaged systems. The use of experimentally validated analytical tools such as finite element models can be a great advantage in this process. In many cases, analytical tools are used to run simulations where defects are introduced to perform numerical experiments. Damage accumulation tests, during which significant structural elements are subjected to degradation under real loading conditions, can also be used to identify specific features. Understanding of the appropriate features can be gained from different types of both analytical and experimental studies, and usually, the results are combined to obtain even more reliable information. Statistical model development deals with the implementation of algorithms that work in feature extraction to quantify the damaged level of the structure. The algorithms used in this phase are of two types. When data are available referring to known damage conditions that have been uniquely identified, that means that a labelling is possible the algorithms are called supervised learning. While unsupervised learning is algorithms applied when no data are available from training so one can assess only the consistency of the new data with those of reference. The damaged state of a system can be described in five steps by answering four questions as proposed by Rytter [12]:

- i. Detection - Is the structure damaged?
- ii. Localization - Where is the damage?
- iii. Quantification - How severe is the damage?
- iv. Prognosis - What is the remaining service life of the structure?

The answer to these questions in the proposed order represents an increment of knowledge of the damage level. When applying unsupervised learning algorithms, statistical models answer questions regarding the existence and location of the damage. An answer as to the type, extent, and prognosis involved in the damage is provided by the use of supervised learning algorithms coupled with the use of analytical models. Structural

monitoring involves several steps, each of which must be carefully designed. First, the instrumentation step concerns the choice of transducers to be placed and their location according to the quantities that are decided to be measured. In long-term structural monitoring with repeated measurements, the instrumentation used is permanent type, although other solutions are also possible. Usually, wired sensors are used, but wireless sensor types and sensor networks are being developed and researched, especially in applications to historic buildings where low invasiveness of the monitoring intervention is required. For example, Barsocchi et al. [13] shows an application of the WSN (Wireless Sensor Network) technology to the long-time monitoring of historic masonry tower. The advantage of wireless sensors lies in the fact that there is no need to lay cables for their installation, which is a very important aspect in the case of very extensive and complex monitoring systems using a large number of sensors; in addition, cables and connectors are subject to wear and tear. In the other hand, the main disadvantages of wireless sensors are high power consumption, and slow data transfer and synchronization, so characteristic algorithms must be designed and applied for such systems, although with the advancement of technology these problems are less felt. The number of sensors can vary from one to several hundred depending on the complexity of the structure and the features that need to be detected. The type of sensors depends on the purpose of monitoring and on the type of the structure. Usually, they are accelerometers, velocimeters, strain gauges, fibre optics and lasers. The measurements require the instrumentation to have high sensitivity, for example, in the case of the Ambient Vibration Test (AVT) the vibrations induced on the structure are of small amplitude. Sensor locations can be determined using a finite element model of the structure to dynamically characterize the structure and predict damage scenarios using heuristic optimization methods. Excitation can be environmental, in this case the dynamic identification process is called Operational Modal Analysis (OMA), or artificial for the dynamic identification process called Experimental Modal Analysis (EMA). In typical structural monitoring applications on civil engineering systems, excitation cannot be measured and vibrations can be caused by wind, traffic, ice, or seismic events. The advantage of having artificial excitation is that it can be controlled and measured. Having artificial excitation is useful because in this way the entire band of

frequencies of interest can be investigated. One can achieve these results by using vibrodynes, impact devices or an actuator already in the machine. Artificial excitation can be used for small structures or in the laboratory. It should be kept in mind, however, that in most civil engineering structures, with low natural frequencies, artificial excitation is difficult to apply and very expensive and requires extensive use of hydraulic actuators and a lot of power. Artificial excitation makes it possible to monitor the structure under extraordinary conditions, but it should not be forgotten that data on operating conditions must also be acquired. Often, structures are subject to disturbances due to wind, environmental vibrations due to traffic, or other sources that cannot be measured and monitored. The advantages of environmental excitation lie in its cost-effectiveness, the constant presence of loads and excitation even at low frequencies, as already mentioned, the disadvantages concern the inability to quantify the strength of the excitation and the range of frequencies investigated is small, in fact often only the first modes of vibration can be identified. Sensors convert a measured quantity into an analogue electrical signal. The objective of the acquisition system is to collect the time series of data in a computer for post-processing analysis in order to extract the features. If the features depend on more than one sensor, then those sensors must be sampled simultaneously. The sampling rate and length of the recordings must be matched to the needs of the features to be extracted. The acquisition of automatic data can be clock-based or trigger-based. Digitization of the signal must be done carefully. According to the Nyquist-Shannon sampling theorem [14, 15, 16], if the sampling rate is f_s , the maximum frequency that can be observed is $f_{max} = f_s/2$. If the sampling frequency is low, above $f_s/2$, any signals cannot be perfectly reconstructed from the sampled signal, and are called undersampled and when a signal is undersampled aliasing phenomenon occurs. After the analogue to digital (A/D) conversion, the aliasing phenomenon can no longer be corrected, so it is always necessary to apply an analogue anti-aliasing filter before A/D conversion. The analogue signal is converted (quantized) to the nearest discrete value of the converter A/D. Typically, A/D converters have a resolution of 10 to 24 bits. In the field of measurements, it is divided into $2n$ uniform intervals. For better resolution, it should be used the entire dynamic range. In any case, the signal should not exceed the limits, which leads to overloading and consequently

to signal to clip. The acquisition system must be capable of detecting the overload and rejecting measurements. The dynamic range can be found in preliminary measurements of the monitored structure. Signal processing is used to extract features directly or to operate a data pre-processing step for feature extraction. Typically signal processing extracts some useful information from time series using properties stochastic or by relying on some assumptions. A filter is often applied to limit the range of signal frequencies. In vibration measurement, the mean value is usually removed since it does not contain useful information. The Fourier Transform is the tool that allows the signal to be converted from the time domain to the frequency domain. This method is fast and involves no loss of information in the transformation. The transform of Fourier Transform assumes periodic time series; if the signal is not periodic, it causes a loss of energy for the adjacent time series. The loss can be decreased but not eliminated through the use of windowing techniques. Several functions are extracted from the time series. Some of the most commonly used functions are the correlation functions, power spectral density functions, impulse response functions (IRF) and frequency response functions (FRF). These can be directly used as features or as a step-in pre-processing in the extraction of other features. Monitoring systems that measure vibration are based on data collected during the useful life of the structure. It is therefore important to identify possible faulty sensors to maintain the reliability of the system. Monitoring systems include several sensors that measure the motion global, or minor modes, of the structure. The cross-correlation of sensors can be used to detect malfunctioning sensors and to correct the signal of such sensors. Time series includes a lot of data, which must be compressed to be processed and be able to derive the characteristics of the structure. These features are regarded as the "fingerprints" of the system and are extracted from the time series measurements. The goal is to find features that are sensitive to damage but not sensitive to normal variations of the environment (loads, temperature, etc.). A change in features is a symptom of the presence of damage. Since the monitoring system performs repeated measurements during the life of the structure, feature extraction must be automatic. Some characteristics are easy to extract automatically, while others need supervision and rules to be automated. Feature extraction is classified into parametric and non-parametric. Other classification

methods are input/output or output-only, depending on the measurability of the excitation. In many civil engineering applications, the only identification possible is output-only. The characteristics should be independent of the amplitude of excitation, which makes some features less interesting for monitoring structures. The size of the characteristic vector compared with the time series is significantly smaller. Each characteristic can be used for damage prevention, alternatively, a multi-variable statistic could be used. The first step is to select data from the structure undamaged which represents the reference structural condition. The implicit concept is that damage is meaningless unless one compares two different configurations of the system, one of which is the default level (i.e., the undamaged level), and the other is the damaged one. The initial data must include the full range of environmental or operational conditions since they affect the characteristics and can provide false indications of damage if not properly analysed. The goal of damage identification is to determine if the damage is present in the structure. The decision must be made using statistical methods since all the characteristics vary according to the measurements made so decisions must be made only on significant changes. Building a control chart is one of the primary techniques in the statistical process of control and can also be used in the application of structural monitoring. Qualitative characteristics are plotted as functions of the number of sampling, lower and upper limits are established, which are calculated only from the samplings in which the process is deemed to be under control. When sources of unusual variability, statistical samples will be reported outside the control limits and therefore produced an alarm signal. Multiple control charts can be created, which can have either a single variable or multiple variables (data fusion); from the reading that is taken on these graphs, one can determine the damage level of the structure. The monitoring system must be connected to a network to transfer data of the condition of the structure on the other edge of the network. The monitoring system must be able to send alarm signals as soon as it is established that there is a possibility that damage may occur of damage to the structure. Studies carried out over the past decades in the field of structural monitoring have led the authors to formulate a set of axioms to be applied to the field of SHM. In the practice of structural monitoring the axioms are not sufficient to provide a methodology. As discussed by

Worden et al. [1] the axioms of structural monitoring are:

1. All materials have inherent flaws or defects;
2. The assessment of damage requires a comparison between two system states;
3. Identifying the existence and location of damage can be done in an unsupervised learning mode, but identifying the type of damage present and the damage severity can generally only be done in a supervised learning mode;
4. Sensors cannot measure damage. Feature extraction through signal processing and statistical classification is necessary to convert sensor data into damage information;
5. Without intelligent feature extraction, the more sensitive a measurement is to damage, the more sensitive it is to changing operational and environmental conditions. The length- and time-scales associated with damage initiation and evolution dictate the required properties of the SHM sensing system;
6. There is a trade-off between the sensitivity to damage of an algorithm and its noise rejection capability;
7. The size of damage that can be detected from changes in system dynamics is inversely proportional to the frequency range of excitation;

According to Worden et al. [1], there are two methods for detecting the presence of damage in a structure: Model Driven Approach and Data-Driven Approach. The first method considers damage identification as an inverse problem; a high-fidelity model (e.g. Digital-Twin) of the structure is first created, based on physical laws assuming it to be as undamaged reference condition. Changes in the acquired data are then related to changes in the physical parameters of the structure. The second method considers damage identification as a problem of recognizing a reference model. The interesting data measured by the system are assigned to a class of damage through a pattern recognition algorithm. Such algorithms can be either unsupervised learning or supervised learning. In the case of

supervised learning algorithms are required examples of all damage classes. In the data-driven approach, the damage is identified by identification of a reference model of the structure. Algorithms are implemented to identify the model to assign a damage level to the data collected by the system. These algorithms are based on comparative assessments of the health status of the systems under control with that of other known events. As long as the behaviour of the monitored structure is similar to that of the reference system, the presence of damage in the structure can be excluded, while if the behaviour begins to deviate from that of the reference system, then, the presence of damage in the structure. In the data-driven approach have following procedural steps [17]:

1. Acquisition, where the sensors provide an electrical signal proportional to the structure response and environment of interest. The sampling rate of the signal depends on the data that are to be measured.
 2. Pre-processing: the collected data are prepared for future processing to the extraction of system characteristics, especially data cleaning that reduces the size of the data. The cleaning phase includes the removal of noise, spikes, and outliers and scattered data. The dimension reduction seeks to eliminate redundancy in the data.
 3. Feature extraction: patterns are identified from the literature based on characteristic typology. The purpose is to separate the normal behaviour of the structure from any change in properties which can be attributed to a given level of damage. This can be based on statistical data or engineering evaluations
 4. Post-processing: is the final stage for preparing a reference model, often included in the feature extraction. Normalization of the feature vectors as required by the pattern recognition algorithm. More in-depth processing can be addressed to obtain a probability distribution.
 5. Pattern recognition: is the most critical stage of the process. Characteristic vectors go through an algorithm that can classify the data. There are three types of algorithms based on the desired diagnosis: novelty detection, classification, and regression.
-

6. Decision: based on the results of the previous stage of making decisions. This phase can be performed by humans or it can be automated.

The model-based approach makes it easier to deal with new or unexpected situations since this technique can integrate and replicate a wide range of behaviours, even if not previously observed in real systems, this is because this approach is based on numerical models and not on available data collections. When the state of a structure deviates from the expected operational behaviour, can continue with updating the numerical model and the physical parameters that describe the new situation. Because of this capability, this method does not use the historical information that is required by the data-driven approach. Compared with the data-driven approach, in the model-based approach the model updating stage is added, replacing the pattern recognition stage. In the model updating process, a numerical model (e.g., FEM) is updated based on the identified parameters. Model updating can be direct (single-step correction) or indirect (recursive minimization of a penalty). The monitoring strategy that can be applied includes a distinction between monitoring static, aimed at the continuous detection of gradual, slow changes in certain parameters over periods of rather long periods, and dynamic monitoring, oriented to the control of dynamic properties of the monitored structure both under operational conditions and during extraordinary events (e.g. earthquakes). Static monitoring requires measurement of small variations over long periods. A few measurements per minute, in some cases per hour, may be sufficient to obtain indications of the parameter subject to the variation that may be caused by climatic cycles. Dynamic monitoring is intended to provide a dynamic or seismic response characterization of the structure. Dynamic monitoring can be carried out punctually or periodically through instruments capable of performing dynamic tests by measuring vibration properties of the structure induced by external loads or natural phenomena. Another possibility is to install permanent systems capable of self-activating and capturing the motion of the structure whenever an earthquake occurs or a significant source of vibration exceeds a certain threshold (trigger-based monitoring). Continuous dynamic monitoring requires extensive data availability to collect the acquired data. Monitoring dynamics has been highly developed both to implement damage detection

based on algorithms that deal with changing of modal properties of structural system (such as natural frequency, mode shapes and damping ratio) that can be related to the damage and both to control the dynamic behaviour during exceptional events (strong winds or earthquakes). In the design phase of automatic and long-term monitoring systems, it is necessary that the choice of instrumentation should be made after a detailed analysis of the environmental conditions so that the necessary protection of the instrumentation can be ensured, the absence of electrical noise, and the accessibility for installation and maintenance of the sensors must be evaluated, the latter being of critical relevance to ensure the reliability of the system. It is also necessary to consider all types of errors (systematic or causal) that may intervene on the data collected by the instrumentation, making sure that possible faulty sensors or possible system malfunctions are automatically detected.

2.1 Modal identification and damage detection

Modal identification of a structure means all those techniques that allow the dynamic response of the structure itself to be identified in terms of its self-frequencies, corresponding modal shapes and damping coefficients from the design of the structure to the operating conditions. During the operating condition, especially for strategic buildings (dams, bridges, large industrial plants, nuclear power plants, etc.) or historical ones, the analysis is implemented through a series of periodic or continuously measurements. Through the monitoring it is possible to diagnose ongoing degradation phenomena. Knowledge of the modal parameters of a structure also makes it possible to predict the response it will have when subjected to stresses environmental stresses such as earthquakes. Thus, allowing one to go in and intervene in a preventive manner on any weaknesses encountered. So, the structural monitoring of civil structures is not only to identify damage sudden or progressive but also in monitoring the performance of the building under operating conditions operation or during particular events. A monitoring consists of sensors that can measure both environmental stresses and the structural response to those. The aim is not only to assess the resistance to an earthquake of a building, but is also to monitor the functionality of the structure in the operating conditions, to possibly

design effective retrofitting seismic or reinforcement of critical structures. Thus, structural monitoring involves a large number of applications in the field of civil engineering such as design, assessment of damage, maintenance and reinforcement of existing structures, structural monitoring during earthquakes [18, 19]. Advances in the field of communication systems allow real-time monitoring of the structure. Data are processed to detect anomalies or for evaluations of long term. For earthquake risk analyses, monitoring systems can be used to create a database of measurements taken during the entire life cycle of the structure. It is therefore essential to identify the modal parameters of the structures under operating conditions and of the technique for damage detection, which explains the fundamental role of operational modal analysis in the field of structural monitoring. To determine the dynamic behaviour of a structure, two different approaches are possible:

- The analytical approach: starting from the knowledge of the geometrical and mechanical properties of the structure, the boundary conditions, the distribution of masses, of stiffness and damping, it is possible, by solving an eigenvalue problem, compute the modal parameters of the system (natural frequencies, factors damping and modal forms);
- The experimental approach: starting from a modal identification, the frequency response functions are calculated and, from its, the dynamic parameters of the structure.

The various experimental identification techniques initially studied in aeronautics field [20], have since been extended to others, from the automotive industry to robotics, to civil construction. Modal identification, in general, means all those techniques, analytical and experimental, that make possible to identify the dynamic behaviour of the structure (frequencies, modes of vibration and damping coefficients). This is based on the idea that the dynamic behaviour of the structure is a "fingerprint", and depends on intrinsic properties like masses, stiffness, damping, degree of buckling, etc. and not on the magnitude and/or type of applied load. Therefore, if there are no internal changes in the building (e.g., structural damage), the dynamic behaviour of the structure remains unchanged, conversely, in the presence of damage phenomena, changes will

be noticed in the modal parameters of the structure. If we consider only the diagnostics function of the structural health monitoring can say that is a new and improved method for performing non-destructive assessment [21]. In addition, the application of various modal identification techniques in models subjected to laboratory testing makes it possible to determine the structural damage that may be present, as well as information about the influence of reinforcement techniques in dynamic behaviour. With the advent of transducers, sensors and acquisition, the first modal tests were introduced Ewins [22]. It was not until the 1980s that this methodology was also adopted for the characterization of civil structures [23]. In particular, several methodologies were tested, based mainly on the analysis of the response of a structure subjected to the application of an external forcing (input-output methodology), or on the study of its natural vibrations (output-only methodology). These analyses lead to the identification of fundamental frequencies, modal shapes, ratios damping and other modal parameters. Based on their variation, the following can be identified and localized structural damage. In the past as in the present day, numerous applications in the field of civil engineering involve steel or reinforced concrete structures. A comprehensive overview of these topics and application methodologies is provided by [24], while further and more recent research, such as the application of structural damage identification and localization in R.C. structures, the variation of dynamic characteristics in different structural elements structural elements as damage increases, and the determination of damage in P.R.C. elements [25], also delve into the effects of the procedures of early retirement in facilities. The studies and research just mentioned demonstrate how dynamic testing represents a potentially very effective methodology of investigation, capable of obtaining multiple information regarding both the whole structure and local damage. The application of such methodologies to the built heritage and, more generally, to historic buildings, is a topic that has only begun to be developed in recent decades, and is still in the midst of an evolutionary stage. Casarin et al. [26] conducted an experimental study on the assessment of the vulnerability structural of the Cathedral of Reggio Emilia, to identify its dynamics. In addition, the results obtained were used to develop and calibrate a complex finite element model (FEM). This study emphasizes the possibility, through the use of dynamic monitoring systems, to deter-

mine both global and local behaviours. Such knowledge leads to a choice of the most appropriate intervention, if necessary, and enables the analysis of the effectiveness of reinforcement techniques on the structures under consideration. A further and important study [27] deepens and develops a methodology of damage identification to be applied specifically to masonry structures. They were conducted experimental laboratory tests on masonry arches and panels, through the application of induced vibrations, in order to assess damage propagation. This method was then applied to some real case studies, including the Clock Tower in Mogadouro and the Church-Jerònimo Monastery, in Lisbon. Some authors [28, 29] performed a series of laboratory experiments on masonry panels, stone pillars and slabs, and R.C. beams. In addition, the simplicity of the experiments performed made it possible to demonstrate the validity of the dynamic evaluation of structural elements. It was also conducted extensive numerical simulation to reproduce the actual conditions. The combination of these analyses is suitable for studying the correlation between the occurrence of damage and the variation of the dynamic properties of some structural elements considered. Finally, the methodology has been validated through its application on the components of historic masonry buildings in Spain and Belgium. In addition to these researches, which are completely aimed at the development of a new methodology of identification and correlation with the mechanical characteristics of structures, numerous other studies have been developed regarding the application of dynamic identification on buildings made of masonry. Many of these applications are case studies in which monitoring was performed dynamics and modal parameters were identified. The dynamic behaviour of an existing masonry building was examined by De Sortis et al. [30]. In particular, low levels of vibration were studied, as in Ramos [27]. The use of different types of vibrations allowed the determination of structural damage. Interesting and excellent connections were found between the frequency response functions numerical and experimental, thus allowing the conclusion that a good technique of identification can provide useful information on the dynamic properties of existing structures made of masonry. An interesting application of operational modal analysis for damage assessment was carried out by Ramos et al. [27]. The identification method was applied to a model of a one-story masonry building subjected to shaking tests [31]. In addition to the

identification and localization of structural damage, one of the main objectives of this study was the comparison of classical modal analysis with "environmental" modal analysis. This has allowed the validation of the use of the latter technique in particular for the detection of damage in its early stages of development. Some environmental vibration tests were conducted to define the dynamic properties of the minaret in Qutb, India [32]. The analysis conducted allowed the identification of seven different modal shapes. In addition, several types of finite element models were created to simulate the structural response, and the results obtained manifested a good relationship with the values derived from modal identification. These models were then used to evaluate the overall performance of the structure, and to define the maximum allowable seismic stress. Further applications on the wide use of dynamic monitoring are those presented by Rinaldis et al. [33]. The subject of the studies was the use of wireless systems and sensors with fiber optics for structural monitoring of historic buildings. In particular, the authors emphasize the great advantages, low cost and the possibility of acquiring high quality information and in real time on the dynamic behaviour of the structures under consideration, allowing an highly effective safety assessment and structural monitoring. Still, other important experiments on real case studies have been presented by various authors [34, 35, 36]. In all cases the aim main purpose has been to study the dynamic characteristics of damaged structures, mainly frequencies and modal forms. Starting from the results obtained from these analyses, the authors were able to draw observations on the structural conditions of the examined elements, and this enabled the design of the most appropriate reinforcement interventions for the respective needs. The continuous monitoring, finally, provided a way to evaluate the effectiveness and usefulness of such interventions. As can be seen from the previously mentioned research, the application of identifying modal to historic buildings represents a difficult issue because of the great variability in the mechanical properties of masonry, unlike other more homogeneous materials, such as R.C. or steel. However, it is evident how this technique can be very useful, and how it can be effectively applied in the survey of historic buildings. Currently, this methodology makes it possible to obtain global information about the structure examined, in an absolutely non-destructive way, providing moreover information that cannot be obtained from other NDT.

2.2 Modal Identification Techniques

In the field of engineering, modal identification techniques are steadily increasing; in fact, although the development in the IT (Information Technology) field has led to computers with higher performance, allowing increasingly complex finite element models to be built in order to study the static and dynamic properties of structures, it often happens that the properties dynamics differ from the actual properties of the structure. This difference can be attributed to several causes: - Finite element analysis is based on a discretization of reality, by which is meant that displacement fields are approximated through predefined shape functions within each element; while mass and stiffness properties are easily evaluated based on the material properties and the geometry of the elements, it is much more difficult to take properly account for the damping properties of the structure within the model, in fact, damping related not only to material properties but also to a number of other mechanisms that are difficult to model analytically (opening and closure of microcracks, interaction with other non-structural elements, etc.). The actual geometry may be different from that considered in the model. To bridge the differences between the real structure and the finite element model, it is necessary to use experimental techniques in order to check the results of the model with those obtained from measurements, the measurements obtained make it possible to update the model so that it adheres to reality. Dynamic identification tests of fall into two categories in relation to the knowledge or less of the stress to which the structure is subjected: - Input-output techniques where both the exciting forces and the response are measured. structural. The structural is stressed at one or more points; as a result of the stress, the structural response is measured. In this case, the dynamic analysis carried out is called. Experimental Modal Analysis (EMA): these procedures allow the determination of the dynamic properties of the structure in terms of natural frequencies, damping ratios and modal shapes; these parameters will be used to calibrate the model of the structure. It is, in addition, possible to determine the modal parameters of the frequency response function of the input signal response. Output-only techniques where only the response of the system is measured. Modal analysis can also be carried out in the case of ambient excitation, which is considered to be white noise, so

the input on the structure is not known, in which case the techniques of analysis modal take the name Operational Modal Analysis (OMA). OMA techniques lead to the same results as EMA techniques, with the difference that it is impossible to determine the modal participation factors by not knowing the input to which the structure is subjected. Experimental modal analysis, based on applying a known input to the structure, is not easily applicable to most buildings, so it is preferred to work through operational modal analysis, exploiting ambient noise for structural identification, thus avoiding the use of special equipment (such as vibrodynes, instrumental hammers, exciters hydraulic or electrodynamic) that directly excite the structure. This translates into a number of advantages:

- The test is quick and inexpensive, since no equipment is needed to stress the structure;
- Measurements are made under the actual operating conditions of the structure, so the dynamic parameters obtained are representative of the dynamic behaviour of the structure under actual operating conditions;
- The test does not interfere with the operation of the structure.

The correctness of the results provided by OMA may, however, be affected if white noise is superimposed on non-random excitation. The signal processing of acquired data is a key step in which it is important to avoid errors in data analysis. In this regard, it is noted that, normally, acquired signals, such as acceleration, displacement or forces, are contained in the time domain, while the most common analysis methods process data in the frequency domain. The first step in signal analysis is the conversion of the signal itself, collected in analogue form, into digital form, in this way the collected data are processed in the form of discrete values and not continuous functions. It is noted that a signal can be defined as analogue or digital in the following manner:

- Analogue signal: a signal represented by a continuous function over time, it is a signal analogous to the physical signal it represents;
 - Digital signal: a signal represented by a sequence of numbers, each of which represents the value of the signal at a given instant of time (the signal is discretized).
-

At this early stage of conversion, several types of problems inherent in the mode of data acquisition and the mode of signal transformation are identified: these problems are related to the occurrence of aliasing and leakage errors, and which are attempted to be remedied by windowing and overlap averaging procedures. To digitize a continuous signal, usually, the sampling of the signal is done at equal time intervals; the problem is, therefore, to define the sampling interval Δt . It must combine the requirements of reducing the computational burden and obtaining an effective representation of the signal. Thus, sampling at points that are very close together will lead to an overabundance of data, increasing the computational burden; conversely, a sparse sampling with points far apart will lead to confusing low and high frequencies in the original data. This problem defined as aliasing constitutes a potential source of error that affects any process that is preceded by a signal conversion from analog to digital.

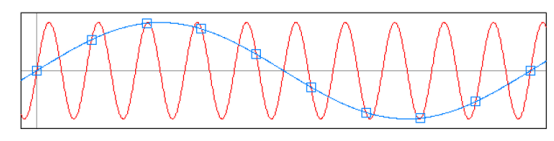


Figure 2.2. Example of under sampled signal (red line is original signal, blue line is measured signal)

Defined the sampling interval Δt to it will correspond a certain sampling frequency equal to $1/\Delta t$, which in turn defines the number of samplings made within one second. It is important to note that at least two samplings of the original signal frequency are required to detect a cycle. Therefore, the highest frequency that can be defined by a sampling ratio of $1/\Delta t$ samples per second is $1/2\Delta t$. Frequencies in the original signal above $1/2\Delta t$ will be folded back into the 0 and $1/2\Delta t$ frequency range and confused with the data already in this interval. The cutoff frequency $f_c = 1/2\Delta t$ is called the Nyquist frequency. To avoid the cut-off of higher frequencies, the problem can be solved in two ways. The first is to have denser sampling (but increasing the computational burden). The second is to filter the signal before sampling it with respect to a maximum frequency of interest. If one chooses the Nyquist frequency f_c equal to the maximum frequency of interest, one will aliasing-free results will be ob-

tained for frequencies below f_c . Leakage is a problem related to the length of the time-history that is of finite size, associated to the assumption of periodicity of the signal. If one considers a signal stretch of length T equal to an integer multiple of the signal itself, there is no problem; otherwise, the assumption of periodicity is not strictly valid particularly near the ends of the interval, this results in a dispersion of the spectral energy. Windowing is a method employed to solve the leakage problem of filtering the signal initial $x(t)$ through a filter function $W(t)$. The windowing operation, in the domain of the time, returns a signal $\hat{x}(t) = x(t) - W(t)$ in which the spectral energy dispersion is contained. The signal is divided into several sections; this is necessary, first of all, because of the assumptions of applicability of the Fourier transform, which require that the input function be defined over a limited interval finite amount of time (whereas a random signal, such as may be that of a white noise used, is temporally infinite); moreover, this expedient averts the inevitable risk that, if the period of the signal and the windowing interval do not coincide, a error in the reconstruction of the signal when applying the Fourier transform, which involves the repetition of the selected window; the Fourier transform thus recomposes a signal different from the original one, resulting in the distribution of information over a band of frequencies, rather than on a single line. The types of windows used in signal analysis are:

- Box Window
- Hanning Window
- Cosine Taper Window
- Exponential Window

Each window generally refers to one type of signal. In the analysis of random signals, it is not enough to calculate the Fourier transform, strictly speaking this does not exist for a random signal, one must instead obtain an estimate of the density spectral and autocorrelation function used to characterize this type of signal. However, since these quantities are obtained by the Fourier transform, it is necessary to perform an averaging operation [37, 38] covering a good number of samples. For a random signal the averaging operation can be performed on sequential or overlapping samples.

2.3 Output-only modal identification methods

Output-only modal identification or ambient vibration testing techniques have been developed in mechanical and aerospace engineering, but they have also become very important in civil engineering works, such as bridges and skyscrapers, in which external excitation and the determination of applied forces is a problem. The techniques are based on measuring of the dynamic response of a virtual system under natural loading conditions (both environmental and operational) and on the assumption that the external excitation is random in nature in the domain of the time and in the physical space of the structure. In this type of identification techniques, the fundamental assumption about the excitation forces of the virtual system is to consider the environmental stress as a process stochastic white noise in the frequency range of interest. Because of the nature of the acquired data, the response includes modal contributions from the environmental forces, the contribution of the structural system and the contribution of signal noise from unwanted sources. In addition, the measured response highlights the peak amplitudes of the spectral density function, coming from both the structural system and the environmental forces, consequently the techniques of output-only identification must be able to separate such modal forms. The techniques can be divided into two groups, depending on the type of data collected, which may be in the frequency domain or in the time domain. In the following section will be analysed the main time domain and frequency domain methods.

2.3.1 Time Domain Methods

The time domain methods are based on the calibration of the model through functions of correlation or time series (time history), of each point, measured in the time domain; such techniques are called parametric methods. Generally, methods that exploit the time domain have longer data processing processes and are more complex for users to use than methods that are based in the frequency domain. As an advantage, however, methods in the frequency domain have less difficulty in identifying values of close frequencies, since they overcome the limitations for the resolution of close frequencies due to the FFT process.

Stochastic Subspace Identification (SSI)

The dynamic behaviour of a discrete mechanical system consisting of a number of masses connected through springs and dampers can be obtained by the equation of motion, that is a second order differential equation:

$$[M]\ddot{U}(t) + [C]\dot{U}(t) + [K]U(t) = F(t) = [\bar{B}]u(t) \quad (2.1)$$

where $[M]$, $[C]$, $[K]$ are the mass, damping and stiffness matrices of the mechanical system, $F(t)$ is the forcing vector and $x(t)$ is the displacement vector at continuous time t . How it can observe the forcing vector $F(t)$ is factorised into a matrix $[\bar{B}]$ describing the inputs in space and a vector $u(t)$ describing inputs in time. By defining the state vector $x(t)$ as:

$$x(t) = \begin{Bmatrix} \dot{U}(t) \\ U(t) \end{Bmatrix} \quad (2.2)$$

And by defining the state matrix $[A_c]$ and the input matrix $[B_c]$ as follows:

$$A_c = \begin{bmatrix} -[M]^{-1}[C] & -[M]^{-1}[K] \\ [I] & [0] \end{bmatrix} \quad (2.3)$$

$$B_c = \begin{bmatrix} -[M]^{-1}[\bar{B}] \\ [0] \end{bmatrix} \quad (2.4)$$

The equation 2.1 can be transformed into the state equation [39]:

$$\{\dot{x}(t)\} = [A_c]\{x(t)\} + [B_c]\{u(t)\} \quad (2.5)$$

Theoretically, a real structure is characterized by an infinite number of DOFs. In practice, not all the degrees of freedoms are monitored. If it is assumed that the measurements are evaluated at only 1 sensor locations, and that these sensors can be accelerometers, velocity or displacement transducers, the observation equation is:

$$\{y(t)\} = [C_a]\{\ddot{U}(t)\} + [C_v]\{\dot{U}(t)\} + [C_d]\{U(t)\} \quad (2.6)$$

where $\{y(t)\}$ are the outputs and $[C_a], [C_v], [C_d]$ are the outputs matrices for acceleration, velocity and displacement respectively. This equation can

be transformed into:

$$\{y(t)\} = [C_c]\{x(t)\} + [D_c]\{u(t)\} \quad (2.7)$$

where the output matrix $[C_c]$ and direct transmission matrix $[D_c]$ are defining as follows:

$$[C_c] = [[C_d] - [C_a][M^{-1}[K] \quad [C_v] - [C_a]] \quad (2.8)$$

$$[D_c] = [C_a][M^{-1}][\bar{B}] \quad (2.9)$$

Equation 2.5 and 2.7 constitute a continuous-time determinist state-space model.

However, it is worth mentioning that among time domain methods, it is also important to mention ARMA methods and Next-Type procedures, although they will not be described in detail in this thesis for the sake of brevity.

2.3.2 Frequency Domain Methods

The frequency domain methods are based on the analysis of the signal of each measurement point (in the frequency domain through the application of the FFT) and the correlation between the signals; these techniques are called non parametric. In general, frequency domain methods process data faster and are easier for users to use than time domain methods. As a disadvantage, however, methods in the frequency domain have greater difficulty in identifying values of nearby frequencies, as they have limitations in regarding the resolution of nearby frequencies due to the FFT process. There is no single method to be used in modal identification, in fact, each method offers accurate results when conveniently applied; moreover, each method has its own advantages and limitations. The main frequency domain methods are the Basic Frequency Domain (BFD) method, the Frequency Domain Decomposition (FFD) and the poly-reference Least Squares Complex Frequency Domain (p-LSCF) which will be described in the following.

Basic Domain Method (Peak-Picking)

The simplest method for output-only modal identification is the Basic Frequency Domain (BFD) also known as Peak-Picking method. The classical approach is based on simple signal processing using a discrete Fourier transform, and uses the fact that well separated modes can be estimated directly from the power spectral density matrix at the peak [40]. This method can be classified as a SDOF method for Operational Modal Analysis [41], indeed, the assumption of the method is that only one mode is dominant around the resonance, consequently, there are no contributions from the other modes not in resonance. In this case, the structural response is approximately equal to the modal response:

$$y(t) = \{\phi_r\}p_r(t) \quad (2.10)$$

Where $p_r(t)$ is the modal coordinate related to the r -th mode. As a consequence, the correlation function is approximately given by:

$$[R_{yy}(\tau)] = E[\{y(t+\tau)\} + y(t)^T] = R_{p_r p_r}(\tau)\{\phi_r\}\{\phi_r\}^T \quad (2.11)$$

Where $R_{p_r p_r}(\tau)$ is the modal auto-correlation function given by:

$$R_{p_r p_r}(\tau) = E[p_r(t+\tau)p_r(t)] \quad (2.12)$$

And the spectral density matrix is given by:

$$G_{yy}(\omega) = G_{P_r P_r}(\omega)\{\phi_r\}\{\phi_r\}^T \quad (2.13)$$

Where $G_{P_r P_r}(\omega)$ is the auto-spectral density function of the modal coordinate. As discussed in Rainieri and Fabbrocino [41] the BFD method is effective when the damping is low and when the natural frequencies and mode shapes of the modes are well separated. It can lead to erroneous results, if these conditions are violated. In fact, the method identifies Operational Deflection Shapes (ODS) instead of actual mode shapes, and these are generally a combination of all mode shapes; they are good approximations of the actual mode shapes if only one mode is dominant at the frequencies considered. In the case of closely spaced modes, the respective contributions are significant and the ODS is the superposition of

multiple modes. The method is very simple and computationally undemanding, so it is a useful analysis tool for field tests to get a quick result of dynamic identification.

Frequency Domain Decomposition

To introduce the Frequency Domain Decomposition (FDD) method, it is important to highlight a feature about the measurement of the FRF function in the context of output-only identification. As the stress is considered a Gaussian stationary process with white noise, the PSD function of the stress is considered constant, thus $S_{jj}(\omega) = C$, this assumption indicates that the peaks of the FRF in the vicinity of the resonant frequencies of the structural system can be obtained directly from the peaks of the PSD function by evaluating they're only the response measure. The FDD method can be seen as an extension of the Peak-Picking method, which assumes that the resonance frequencies are well spaced in frequency and that the contribution of modes in the vicinity of the resonant frequencies is zero. The method was presented by Brincker et al. [40] and can be seen as an extension of the PP method, which assumes that the resonant frequencies are well spaced in frequency and that the contribution of modes in the vicinity of the resonant frequencies is zero. The basis of the FDD method are represented by the Singular Value Decomposition (SVD) method of the PSD matrix at a certain frequency ω that leads to following factorization.

$$[G_{YY}(\omega)] = [U][\Sigma][U]^H \quad (2.14)$$

Where $[U]$ is the unitary matrix holding the singular vectors and $[\Sigma]$ is the diagonal matrix with the singular values, the positive and real eigenvalues of the matrix $[G_{YY}(\omega)]$ arranged in descending order. The subscript H is for the complex conjugate transpose matrix. The next step is to analyse the spectrum of singular values of $[\Sigma]$ to select the resonance peaks and the corresponding modes and the evaluation of model components on the measured degrees of freedom. For each set of recorded measurements, a spectral density matrix of power of size $m \times m$, where m is the number of measurement instruments (accelerometers) at available for each test setup:

$$\begin{bmatrix} G_{Y_1 Y_1}(\omega) & \cdots & G_{Y_1 Y_m}(\omega) \\ \vdots & \ddots & \vdots \\ G_{Y_m Y_1}(\omega) & \cdots & G_{Y_m Y_m}(\omega) \end{bmatrix} \quad (2.15)$$

Where $G_{Y_i Y_i}$ and $G_{Y_i Y_j}$ are the auto-spectral density function and cross-spectral density function. The one-side auto-spectral density function $G_{XX}(\omega)$ and one-side cross-spectral density function $G_{XY}(\omega)$ are given by:

$$G_{XX}(\omega) = 2S_{XX}(\omega) = 2 \lim_{T \rightarrow \infty} \frac{1}{T} E[|X_k(\omega, T)|^2] \quad 0 < \omega < +\infty \quad (2.16)$$

$$G_{XY}(\omega) = 2S_{XY}(\omega) = 2 \lim_{T \rightarrow \infty} \frac{1}{T} E[|X_k(\omega, T)Y_k(\omega, T)|] \quad 0 < \omega < +\infty \quad (2.17)$$

Where $X_k(\omega, T)$ and $Y_k(\omega, T)$ are the Fourier transforms of a pair sample records $x_k(t)$ and $y_k(t)$ of finite duration T , respectively, defined as:

$$X_k(\omega, T) = \int_0^T x_k(t) e^{-i2\pi\omega t} dt \quad (2.18)$$

$$Y_k(\omega, T) = \int_0^T y_k(t) e^{-i2\pi\omega t} dt \quad (2.19)$$

For each power-spectral density matrix $G_{X_i Y_j}(\omega)$ performs the SVD (Singular Value Decomposition) into a matrix $[\Sigma]$ made from the singular values and a matrix of singular vectors $[U]$:

$$G_{YY}(\omega_k) = [U_k][\Sigma_k][U_k]^H \quad (2.20)$$

From the graphical representation of the spectrum of singular values, it is possible to identify the peaks to which the modes to be identified correspond.

The FDD method was improved by Brincker et al. [40] with the EFDD method (Enhanced Frequency Domain Decomposition). Basically, the steps of the EFDD method are the same of that of FDD but the esti-

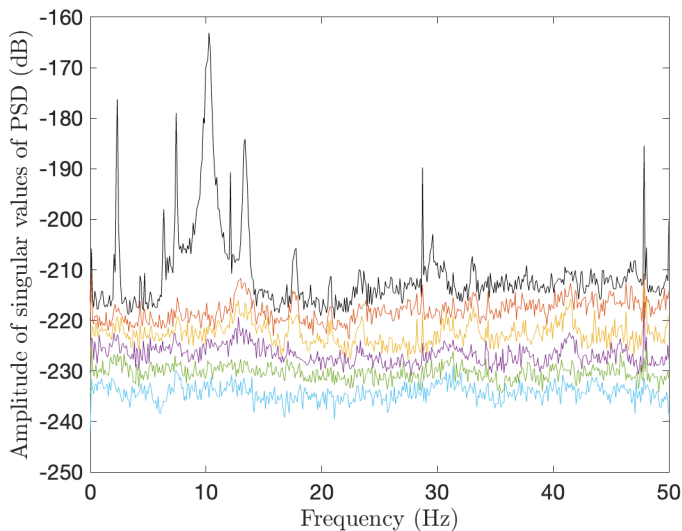


Figure 2.3. Sample singular values plots

mation of frequency values and damping coefficients are calculated by applying the IFFT (Inverse Fast Fourier Transform) function of each spectral density function for each vibrational mode. The obtained auto-correlation response function is now a typical response of a single-degree-of-freedom system with a dynamic response in free vibrations. The intersection with the x-axis gives the natural frequencies for each system, and the damping coefficients are calculated through decrements logarithmic.

The implementation of the FDD/EFDD method is simple. However, this method evaluates frequencies of resonance with discrete frequency values of limited accuracy due to the fact that the method is based on signal analysis through the FFT function. In particular, difficulties are found in estimating frequencies that have values close to the resonance frequencies. To increase the resolution of frequencies, very long time series must be used for the analysis modal. Alternatively, the EFDD method is used, which overcomes these problems because it uses the inverse function FFT for the evaluation of resonance frequencies and coefficients of damping.

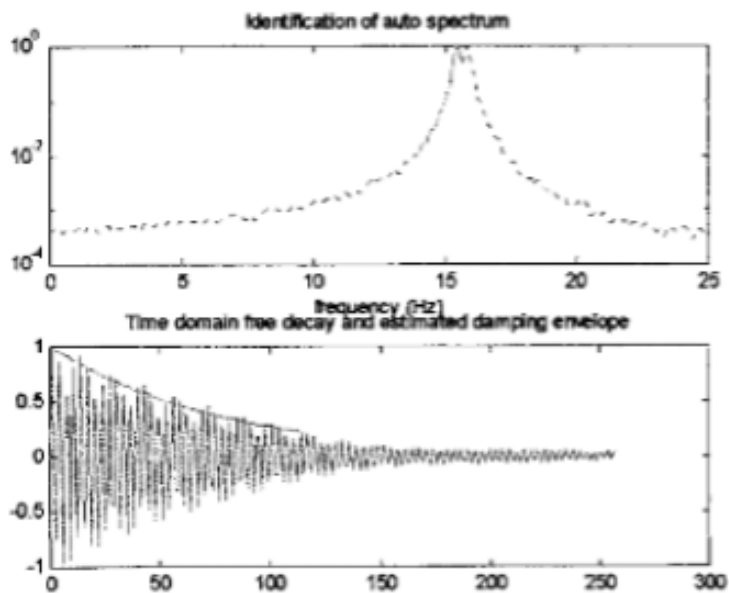


Figure 2.4. Sample of time domain free decay obtained by inverse FFT and estimated damping envelope

Frequency Domain Parametric Procedure

The poly-reference Least Squares Complex Frequency Domain (p-LSCF), also known as PolyMAX (LMS), is a parametric technique developed in the frequency domain, initially developed as input-output methods to perform identification of modal parameters from FRFs. However, for a system excited by white noise, there are some of the similarities between the FRF and mid-spectrum modal decomposition. Therefore, this technique was also exported into the field of output-only identification by Peeters and Van der Auweraer [42]. The LMS PolyMAX method uses the FRF as the starting data. As is usually the case with time domain methods, it requires impulsive responses as the primary data (obtained with the inverse Fourier transform of the FRF). In the poly-reference LSCF method, the right matrix fraction is assumed to represent the measured FRF:

$$[H(\omega)] = [B(\omega)][A(\omega)]^{-1} \quad (2.21)$$

where $[H(\omega)]$ is the FRF matrix containing the FRFs between all inputs and all outputs; $[B(\omega)]$ is the numerator matrix polynomial and $[A(\omega)]$ is the denominator matrix polynomial. Each row of the right matrix-fraction model can be written as:

$$[H_o](\omega) = [B_o(\omega)][A(\omega^{-1})] \quad \forall o = 1, 2, \dots, l \quad (2.22)$$

Where l is the number of the outputs. The enumerator row-vector polynomial of output and the denominator matrix polynomial are defined as:

$$[B_o(\omega)] = \sum_{r=0}^p \Omega_r(\omega)[\beta_{or}] \quad (2.23)$$

$$[A(\omega)] = \sum_{r=0}^p \Omega_r(\omega)[\beta_{or}] \quad (2.24)$$

Where $\Omega_r(\omega)$ are the polynomial basis function and p is the polynomial order. In the polyMAX method, a z-domain model is used (i.e., a frequency-domain model that is derived from a discrete-time model) and, by consequence, the basis function is:

$$\Omega_r(\omega) = e^{j\omega\Delta t r} \quad (2.25)$$

Where Δt is the sampling time. The polynomial coefficient $[\beta_{or}]$ and $[\alpha_r]$ are assembled in following matrices:

$$[B_0] = \begin{Bmatrix} \beta_{o0} \\ \beta_{o1} \\ \vdots \\ \beta_{op} \end{Bmatrix} \quad [\alpha] = \begin{Bmatrix} \alpha_0 \\ \alpha_1 \\ \vdots \\ \alpha_p \end{Bmatrix} \quad [\theta] = \begin{Bmatrix} \beta_1 \\ \beta_2 \\ \vdots \\ \beta_l \\ \alpha \end{Bmatrix} \quad (2.26)$$

The FRF model is now written as function of the coefficients $[H(\omega_{k,\theta})]$. Note that in the polyMAX method real-valued polynomial coefficient are assumed. This procedure allows a stabilization diagram to be constructed to increase the order of the model and use stability criteria for frequencies, damping ratios and factors of modal participation. Theoretically, modal shapes can be derived from the coefficients $[\alpha_r]$ and $[\beta_{or}]$, but can be also found by considering the so-called pole-residue model:

$$[H(\omega)] = \sum_{j=1}^n \frac{\{v_i\}[l_i]^T}{j\omega - \lambda_i} + \frac{\{v_i^*\}[l_i]^H}{j\omega - \lambda_i^*} + \frac{[LR]}{\omega^2} + [UR] \quad (2.27)$$

Where n is the number of modes; H denotes the complex transposed conjugate of the matrix; $\{v_i\}$ are the modal forms; $[l_i]^T$ are the modal participation factors; and λ_i are the poles. [LR] and [UR] are the lowest and highest residuals, respectively, which model the influence of the out-of-band modes with respect to the considered frequency band. The interpretation of the stabilization diagrams indicates a series of poles λ_{i} at corresponding participation factors. Since the only unknowns are the modal forms, $\{v_i\}$ and the lower and upper residuals, they can be obtained by solving the equation linearly by the method of least squares. This step is called the Least Squares Frequency Domain (LSFD). The p-LSCF algorithm is considered one of the most accurate in the field of OMA techniques in the domain frequencies. The stabilization diagram obtained is extremely clear and makes it much easier the selection of physical poles.

Chapter 3

Correlation between modal parameters and damage: methodology

As described in the previous sections, many studies in the literature explain how to perform the operational modal analysis (OMA). There are also many techniques to extract the modal parameters of a structure and read the variation after damage, but there are very few studies that correlate the modal parameters variation to a damage level. This chapter presents the methodological framework adopted for estimating a correlation between variations in modal features of structures and the experienced damage levels. The study is conducted for different levels of structural complexity, starting from a portion of a structure like a column or a bridge pier, passing to a 2D frame of a real case-study building and finally to the entire 3D case-study building. This aim is achieved following two different approaches, a numerical one and an experimental one. For the numerical approach, the methodology is the same for all levels of structural complexity and can be divided into three steps. The first step is the numerical modal analysis of the FE model of the structure at the initial condition, i.e. the condition of no damage. The second is a cyclical procedure that aims to simulate the damage of the structure for different damage levels and for each level, the modal properties are computed with a new eigenanalysis to evaluate the variation of these properties, fixed the damage

level, with the stiffness matrix updated to the fixed condition. The last step provides the quantification of the damage index. The experimental approach has two objectives: the first is to validate the FEM model of the structure and to verify the variation of modal properties derived from the numerical simulation. Specifically, once the geometry of the structure and the loading protocol are fixed, the structure is damaged through experimental tests in the laboratory. In this phase, two operational modal analyses are performed, one on the undamaged condition of the specimen and the other on its damaged condition at the end of the test. From the experimental test, the FEM model is generated and validated on both the static part (hysteretic or pushover curves) and the dynamic part, in terms of frequency. Once the model has been validated, the evaluation of the dynamic properties is extended to a more extensive database of structures, generated by varying the main geometric and mechanical characteristics. For each sample, the variation of modal properties is evaluated for different damage levels, thus obtaining a correlation matrix between the variations of its modal properties (e.g. frequency) and the damage level reached. As previously mentioned, the thesis focuses on seismic damage quantification. However, the proposed methodological framework can be easily extended to different types of structural damage. In the following paragraphs, the damage scales adopted for seismic damage quantification are first presented and, hence, the experimental and numerical approaches are briefly illustrated.

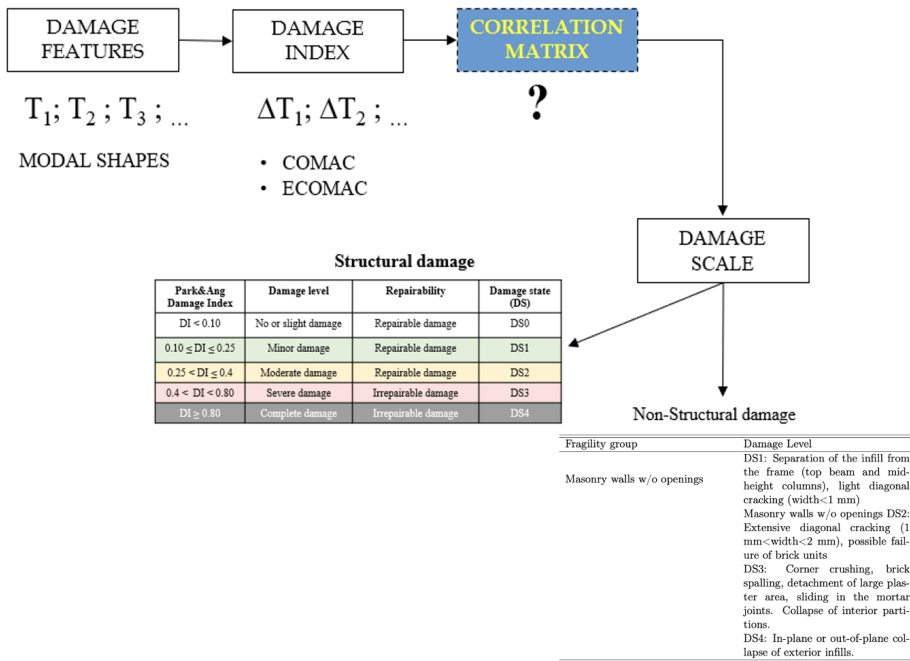


Figure 3.1. Methodological framework

3.1 Seismic damage scales for damage quantification

3.1.1 Structural damage

The level of seismic damage of structural components (RC columns or piers) and its reparability is herein classified adopting the Park and Ang damage index (DI) [43], which is defined as the linear combination of ductility and dissipated energy as follows:

$$DI = \frac{\delta_m}{\delta_u} + \frac{\beta}{Q_y \delta_u} \int_0^t dE \quad (3.1)$$

in which δ_m is the maximum deformation experienced during the seismic event, δ_u is the ultimate deformation capacity under monotonic loading, Q_y is theoretical yield strength and dE is incremental absorbed hysteretic energy. The constant parameter β is taken equal to 0.25 for slightly reinforced structures [44]. The classification of damage levels and structural reparability as a function of the Park and Ang DI is reported in 3.1 (Young-Ji Park et al. [43]).

Table 3.1. Damage scale and DI thresholds from Park et al. 1985

Name	Index	Damage Level	Reparability
$DI < 0.10$	DS0	No or slight damage	Reparable damage
$0.10 \leq DI \leq 0.25$	DS1	Minor Damage	Reparable damage
$0.25 \leq DI \leq 0.40$	DS2	Moderate Damage	Reparable damage
$0.40 < DI < 0.80$	DS3	Severe damage	Irreparable damage
$DI \geq 0.80$	DS4	Collapse	Irreparable damage

For the whole building an approach is proposed to correlate local and global structural damage after a seismic event. Indeed, the relationship between the local damage of single structural members and the global structural damage is not well assessed for damage levels definition. The approach adopted herein consists in two phases: (i) assess the local damage level of single structural members (i.e., columns) by using the IDR_{max} (Maximum Interstorey Drift Ratio) and (ii) correlate the global damage of the building with the local damage of structural members (DL). The

approach is depicted in Fig. 3.2 where the ΔT is the variation of period between the building's undamaged and damaged configurations.

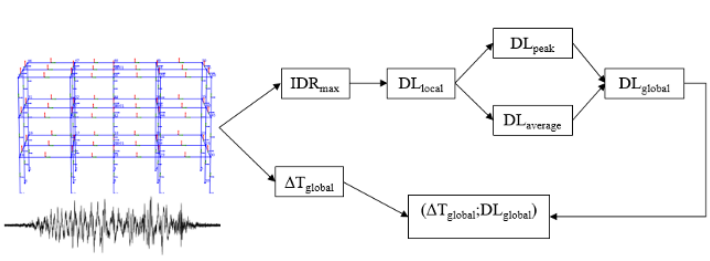


Figure 3.2. Scheme of methodology framework for buildings

The local damage level of each column is evaluated based on the maximum interstorey drift ratio (IDR_{max}) according to the relationships derived in this thesis for columns and reported in Table 3.2. Knowing the local damage level of each column, the global damage level (DL_{global}) is estimated as: (i) the peak damage level experienced by the columns (DL_{peak}), representing the highest DL among all columns, and (ii) the average DL ($DL_{average}$), evaluated as the weighted average damage level of the whole building. In detail, the average damage μ_d is obtained by the following expression:

$$\mu_d = \sum_{i=1}^4 \gamma_i DL_i \quad (3.2)$$

where DL_i is the i -th level of damage that changes from 1 to 4 and γ_i is the ratio between the number of columns in each DL_i and the total number of the columns. If μ_d is lower or equal to 0.5, the average global damage level is classified as DL0, for $0.5 < \mu_d \leq 1.5$ the average global damage level is classified as DL1, a $1.5 < \mu_d \leq 2.5$ corresponds to a DL2, a $2.5 < \mu_d \leq 3.5$ corresponds to a DL3 and $\mu_d > 3.5$ is classified as a DL4.

Table 3.2. Correlation between IDR and damage level for RC columns

IDR [%]	Damage Level
< 0.5	DL0
0.5-1.2	DL1
1.2-1.9	DL2
1.9-3.8	DL3
3.8-4.8	DL4

3.1.2 Non-structural damage

The level of seismic damage for non-structural components in RC buildings (i.e., masonry infill walls) is classified adopting the Cardone and Perrone [45] damage scale. In particular, the damage states are described as follows:

- DL1 (Light Cracking). At DL1, damage results in detachment of the masonry panel from the RC frame, at the intrados of the top beam and along the upper half-height of the columns. Light diagonal cracking of the infill (1-2 cracks with width <1 mm) in both directions may also occur.
- DL2 (Extensive cracking). At DL2, the cracks developed at DL1 widen ($1\text{ mm} < \text{width} < 2\text{ mm}$). In addition, new diagonal cracks are expected to form in both directions (25-35% of the panel area is assumed to be affected by cracks at DL2). Possible failure of some brick units, located on the upper corners and top edge of the infill (corresponding to 10% of the panel area), is expected.
- DL3 (Corner crushing). At DL3, detachment of large plaster area and significant sliding in the mortar joints are expected to occur. In addition, crushing and spalling of brick units are more widespread on the panel (30% of the panel area is assumed to be affected by crushing/spalling of bricks). The wall is not repairable at reasonable costs (it is more convenient to demolish and reconstruct the entire wall). Frames (if any) are not damaged and can be retrieved and re-installed.

- DL4 (Collapse). DL4 corresponds to the in-plane or out-of-plane (whichever occurs first) global collapse of the wall. Frames (if any) are damaged and cannot be retrieved and used again. It is worth noting that, in the first approximation, the same damage states have been assumed for interior partitions, with the only exception of DS4 that has been assumed coincident with DS3, due to the inherent higher fragile behaviour of partitions at collapse. Damage states for exterior infills and interior partitions are summarized in Table 3.3.

Table 3.3. Description of damage levels for masonry walls considered in this study.

Fragility group	Damage Level
Masonry walls w/o openings	DS1: Separation of the infill from the frame (top beam and mid-height columns), light diagonal cracking (width < 1 mm) Masonry walls w/o openings DS2: Extensive diagonal cracking (1 mm < width < 2 mm), possible failure of brick units DS3: Corner crushing, brick spalling, detachment of large plaster area, sliding in the mortar joints. Collapse of interior partitions. DS4: In-plane or out-of-plane collapse of exterior infills.

3.2 Experimental approach

The methodological framework consists in four steps, as shown in 3.3. The first step consists in performing an OMA (Operational Modal Analysis) test of the structure of interest in its undamaged configuration. In the second step an experimental laboratory test is carried out to simulate the

seismic damage on the structure for an imposed damage. A new OMA test is then carried out, in the third step, for evaluating the modified modal periods of the damaged structure at the end of the experimental test. Finally, in the last step, structural damage levels are experimentally observed and measured and ranges of variation of the selected damage features are derived from operational modal analyses results.

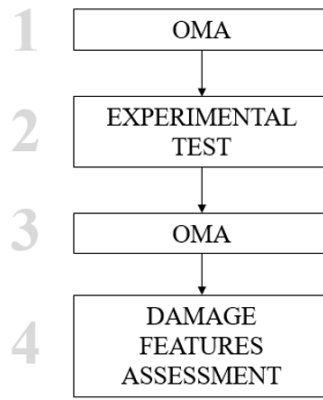
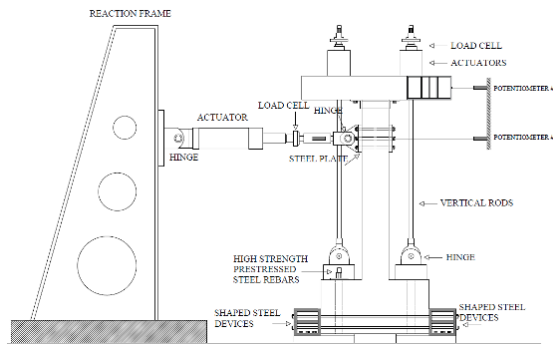


Figure 3.3. Experimental methodological framework

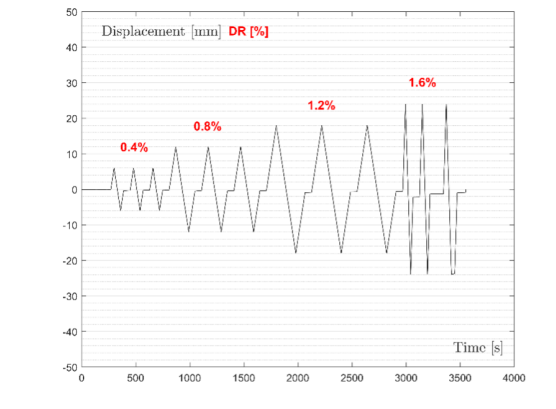
In the following sections will discuss the details of experimental tests conducted for full-scale R.C. columns subjected to static cyclic testing and the test for a full-scale R.C. frame stressed with a pseudo-dynamic test.

3.2.1 RC Columns

The structural damage induced by seismic excitation is experimentally simulated in the laboratory on full-scale cantilever RC columns. Seismic damage is simulated through quasi-static cyclic testing in displacement control. In details, specimens are pushed up to a selected drift ratio (DR) to induce a certain damage level in the column. The axis of the horizontal actuator, shown in Fig. 3.4(a), is located at a distance of 1500 mm from the base of the column. The setup and displacement protocol adopted for the tests are shown in Fig. 3.4(a) and Fig. 3.4(b), respectively. A more detailed description can be found in Di Ludovico et al. [46].



a)



b)

Figure 3.4. Experimental setup for the quasi-static cyclic loading tests (a) and displacement loading sequence (b).

Output-only modal identification tests are carried out on the specimens before and after the quasi-static cyclic tests in order to assess the influence of damage on the modal properties and obtain additional experimental results exploitable for model refinement and validation. The foundation block of the specimens was fixed to the strong floor during the tests in order to simulate a cantilever scheme for the column. Before performing the OMA, the set-up instrumentation (i.e., actuators) was removed to avoid interferences with the modal properties of the cantilever column. Four uniaxial piezoelectric accelerometers (10 V/g sensitivity, $\pm 0.5g$ full-scale range, 0.000008 g rms resolution) were installed along the strong as well as weak direction of the column at different elevations (600 mm, 900 mm, 1200 mm and 1500 mm from the column base. Signals were acquired by a 24-bit digitizer equipped with analog anti-aliasing filter and sampled at 200 Hz. The adopted sampling frequency was sufficient to ensure the identification of the fundamental frequency in each direction. In order to enhance the signal-to-noise ratio, the columns were randomly (spatially and temporally) excited during the tests.

3.2.2 RC Frame

OMA are performed before and after pseudo-dynamic sequences on 2D full-scale RC frames with masonry infill walls, as shown in Fig. 3.5. The purpose of pseudo-dynamic sequences is to simulate non-structural damage and only minor structural damage.



Figure 3.5. Front view of one full-scale RC frame with the pseudo-dynamic test setup.

A strong RC reaction wall is adopted to contrast two actuators for the application of storey displacement histories. Two hydraulic jacks are installed at the top of the frame to apply the axial load on columns. OMA are performed at the beginning of the loading sequences, representing the undamaged condition, and at the end of the loading sequences, representing the damaged condition. It should be noted that the OMA is performed on the specimen without actuators and jacks to avoid undesired constrain effects. OMA is performed by using unidirectional piezoelectric accelerometers having sensitivity 10 V/g and full scale of ± 0.5 g. The layout of sensor is defined based on preliminary modal analyses performed with the software SAP2000, as further discussed in Chapter 4. Data from OMA in terms of natural frequencies and mode shapes are compared before and after damage.

3.3 Numerical approach

The methodological framework for the numerical approach consists of four steps. The first step consists in the development of a non-linear FEM model for the structure of interest, validated on experimental results both in terms of capacity curves and modal properties. In the second step, the fundamental periods and mode shapes of the structure in the undamaged condition are assessed through modal analysis. In the third step, the seismic damage is simulated through numerical analyses. A new modal analysis is then carried out for evaluating the modal properties of the damaged structure. Differently from the experimental approach, the numerical one allows to simulate different levels of damage in structural and non-structural components for increasing IDR or PGA, essential to monitor the variation of modal properties as a function of the damage level. Then, threshold values associated to each damage level can be defined for the structural system under investigation. For RC columns and bridge piers, a cyclic pushover analysis is carried out to simulate the seismic damage for an imposed IDR. Lateral stiffness and residual drift for the imposed IDR are estimated from the pushover curve. The residual drift ratio is computed as the permanent deformation that the structure exhibits when the applied loads go to zero during the last cycle of the analysis. The initial lateral stiffness, k_0 , is computed as the secant stiffness at 70% of maximum lateral force on the envelope curve, as shown in Fig. 3.6. The lateral stiffness at a generic imposed IDR (k_i) is computed as the ratio between peak force at that IDR and related displacement in the positive load direction. This coincides with the peak-to-peak stiffness on the FEM curve.

As shown in Fig. 3.7, the same methodology is adopted for 2D RC frames, but in this case the quasi-static pushover is replaced by nonlinear time history (NLTH) analyses with increasing ground motion intensity. This to replicate the effective displacement history of a frame in a real case-study building during ground motion. Conversely, for 3D RC buildings nonlinear dynamic analyses are performed to simulate seismic damage.

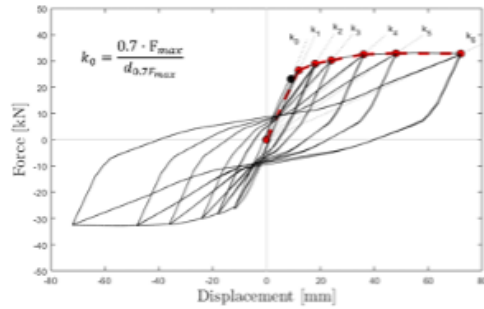


Figure 3.6. Assessment of the lateral stiffness for each imposed IDR.

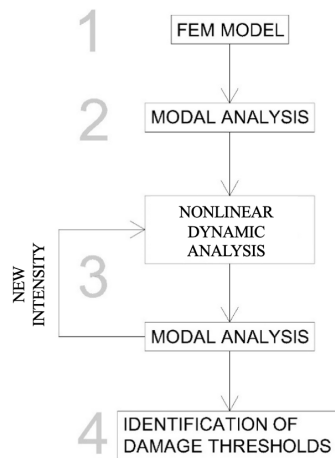


Figure 3.7. Numerical methodological framework for RC columns/piers.

Correlation between modal parameters and damage: experimental tests and numerical analyses

4.1 RC Columns

4.1.1 Experimental study

An experimental program has been carried out to assess the influence of the considered seismic damage on selected damage features for column-type structural members. The structural damage induced by seismic excitation is experimentally simulated on two identical RC columns governed by a flexural behaviour. The specimens (termed A and B) are cantilever columns with a rectangular cross section ($300 \times 500 \text{ mm}^2$) and are reinforced with 12 $\phi 12$ smooth steel rebars, as shown in Figure 4.1. Mechanical properties of materials are derived from experimental testing on cubic concrete specimens and steel bars samples. The mean concrete compressive strength of the specimens at the time of testing is 28.8 MPa; the steel mean yielding strength is 330 MPa.

Three different damage configurations are simulated, as reported in Table 4.1, where C_0 represents the undamaged configuration; C_1 and

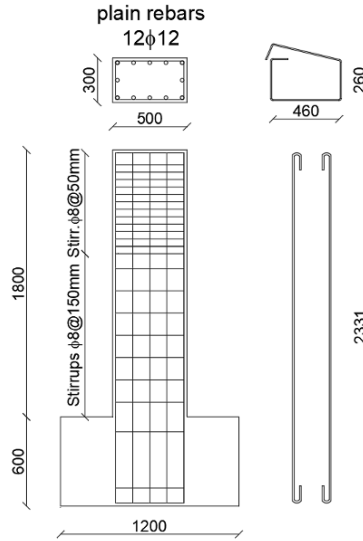


Figure 4.1. Geometry and reinforcement details of the tested specimens (A and B), dimensions in mm.

C_2 are representative of a moderate seismic damage for a seismic loading along the strong and weak directions of the column, respectively.

Table 4.1. Summary of specimen configuration and relative damage.

Damage configuration	Specimen	Seismic damage
C_0	A and B	Undamaged
C_1	A	Moderate damage along strong direction
C_2	B	Moderate damage along weak direction

The horizontal axis of the actuator, shown in Figure 4.3, is located at a distance of 1500 mm from the base of the column. Both specimens A and B are pushed up to a drift ratio (DR) of 1.6%, corresponding to a 24 mm top displacement. The specimens are subjected to a constant axial load equal to 428 kN, corresponding to a dimensionless axial load ratio ν of 0.1. A more detailed description of the setup and instrumentation can

be found in Di Ludovico et al. [46] and in Del Zoppo et al. [44], and are not reported herein for the sake of brevity. Specimen A, damaged along its strong direction, experienced a P&A DI of 0.334; similarly, specimen B achieved a DI of 0.336 along its weak direction. Hence, both specimens are representative of a moderate seismic damage condition, according to the damage level classification reported in Figure 4.2. Capacity curves of both specimens are shown in Figure 4. Both specimens reached the yielding of internal steel rebars, as visible from the capacity curves. At the end of the tests, the specimens showed only hairline cracks on the concrete cover.

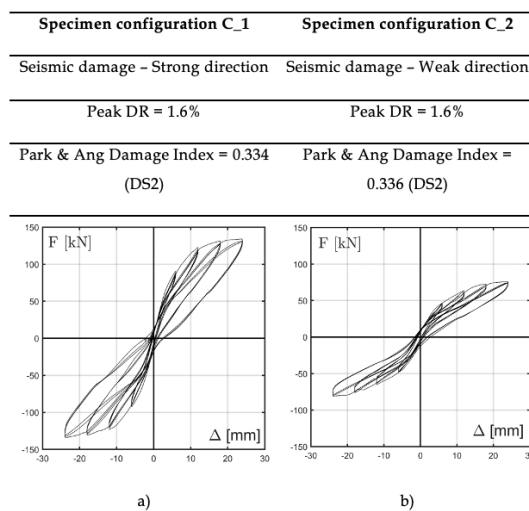


Figure 4.2. Seismic damage simulation: configurations C_1 (a) and C_2 (b).

The layout of accelerometers for OMA on RC columns is shown in Fig. 4.4.

The collected data have been processed according to the Basic Frequency Domain method [41], also known as peak picking method, since closely spaced modes were not expected. The frequency resolution in Power Spectral Density (PSD) estimation was 0.1 Hz. PSDs have been computed according to the Welch’s method by applying 50% overlap and Hanning window. The natural frequencies in the strong and weak directions of the tested specimens in the undamaged and damaged configuration



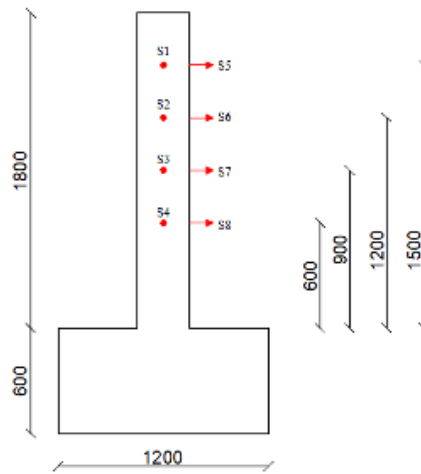
Figure 4.3. Experimental setup for the cyclic pushover tests.

are summarized in Table 4.2. It should be noted that output-only modal identification tests on the undamaged configuration have been performed only for specimen B due to acquisition issues during the tests on specimen A. However, being the specimens identical in geometry, mechanical properties, casting and curing procedures, and base constrain, the values reported in Table 4.2 for the undamaged configuration C_0 can be considered representative of the dynamic properties of both specimens. The first natural frequency for the configuration C_1 is also not reported in Table 4.2 due to some disturbances affecting the measurements that prevented a clear identification of the fundamental frequency.

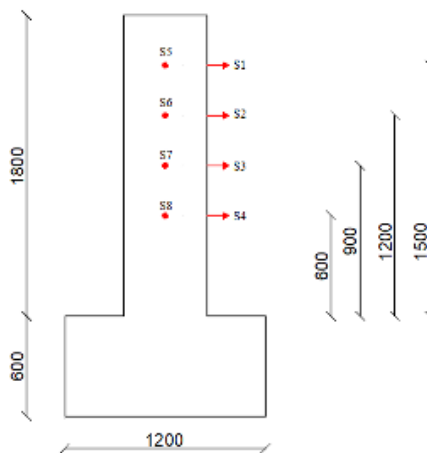
Table 4.2. Seismic damage: experimental natural frequencies.

Configuration	Specimen	Fundamental Frequency	
		Weak direction	Strong direction
C_0	B	31.9 Hz	49.5 Hz
C_1	A	N.D.	26.3 Hz
C_2	B	17.9 Hz	28.2 Hz

It is possible to observe that the damage along the strong direction (corresponding to the second mode of vibration) of the column C_1 has a significant impact on the natural frequency with respect to the undamaged condition C_0, resulting in 47% frequency reduction. A similar frequency



a)



b)

Figure 4.4. Uniaxial piezoelectric accelerometers layout for OMA tests in the strong (sensors S1 to S4) and weak direction (sensors 5 to 8), dimensions in mm

reduction (44%) is achieved also for the column damaged along the weak direction (C_2) with respect to the undamaged natural frequency in the same direction. Furthermore, for test C_2 is also possible to compute the variation in fundamental frequency along the strong direction due to damage occurred in the weak one, corresponding to a frequency reduction of 43%. Corresponding mode shapes before and after damage were also analysed, and the CoMAC and Enhanced CoMAC (ECoMAC) indices were computed. Such indices provide a measure of the correlation (CoMAC) or of the average scatter (ECoMAC) of modal displacements at a given position. The CoMAC ranges between 0 and 1, where 0 indicating a perfect correlation (no changes between the compared mode shapes). Conversely, a value of 1 for the ECoMAC means that the modal displacement of interest remained unchanged for the considered modes in the two datasets under comparison. In the case of real-valued mode shapes and a set of N_m couples of paired experimental mode shapes, the CoMAC associated with the r -th Degree Of Freedom (DOF) can be computed as follows:

$$COMAC_r = \frac{\sum_{s=1}^{N_m} |\phi_{r,s}^{und} \phi_{r,s}^{dam}|^2}{\sum_{s=1}^{N_m} (\phi_{r,s}^{und})^2 \sum_{s=1}^{N_m} (\phi_{r,s}^{dam})^2} \quad (4.1)$$

Where $\phi_{r,s}^{und}$ and $\phi_{r,s}^{dam}$ denote the r -th component of the s -th mode shape in the undamaged and damaged state, respectively. The ECoMAC associated to the r -th DOF can be instead computed as follows:

$$ECoMAC_r = \frac{\sum_{s=1}^{N_m} |\phi_{r,s}^{und} - \phi_{r,s}^{dam}|}{2N_m} \quad (4.2)$$

Experimental results show that mode shapes before and after damage are very similar to each other, denoting a minor influence of the considered damage scenario on the fundamental mode shapes of columns and related CoMAC and ECoMAC, as depicted in Fig. 4.5 for test C_2 along the weak direction. In detail, the ECoMAC is equal to 1 for all the monitored points, indicating that no significant variations occurred in the mode shapes before and after damage. Similarly, the CoMAC values are close to 0 at each control point, with only minor variations close to the base of the column, where the potential plastic hinge zone is located. The experimental results attest a slight sensitivity of both indices to the simulated damage, probably

due to the limited extent of concrete deterioration.

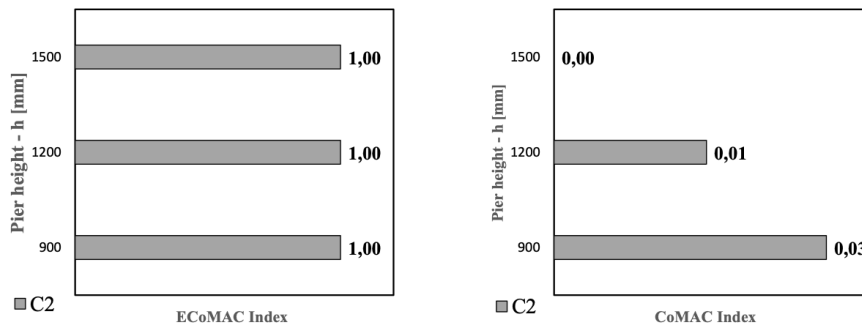


Figure 4.5. COMAC (a) and ECOMAC (b) for each control point of the experimental test of specimen B.

4.2 Numerical study

Variations in fundamental period of RC columns due to seismic damage are then assessed on a dataset of 90 members through extensive numerical analyses on experimentally validated FEM models. Residual drift ratios, commonly used as seismic damage indicator during visual inspections, are also monitored during the analyses. The DMs (Damage Measures) selected for the cantilever columns subject to seismic damage are fundamental period (T), residual drift ratio (d_r) and lateral stiffness (k). The seismic excitation is simulated through cyclic nonlinear static analysis (i.e., pushover analysis) and the interstorey drift ratio (IDR) is assumed as the seismic demand parameter. Thus, the DMs are computed as a function of the imposed IDR (i.e., DM(IDR)) to correlate the changes in those parameters with the seismic damage level. Uncertainties related to the ground motion selection are herein neglected. A refined FEM model for simulating the performance of cantilever RC columns subject to seismic damage is developed. The software OpenSees [47] is adopted to model the nonlinear behaviour of columns through a distributed plasticity model. In distributed plasticity models, the interaction of moments and axial forces is considered simultaneously, and the plasticity is spread along the entire

element length. The BeamWithHinges command is used to build a force-BeamColumn element, which allows distributed plasticity to be spread also beyond the plastic hinge region. For the cantilever column-type element, a single hinge is defined at the base section, and its length is computed as follows [48]:

$$L_{pl} = 0.08L_s + 0.022f_{ym}d_b \quad (4.3)$$

where L_s is the shear length, d_b the longitudinal bars diameter, and f_{ym} the average yield strength of steel. The cross-section of the beam-column element is uniformly discretized into thirty fibres to represent closely small stress-strain variations. The concrete nonlinear behaviour is simulated with the Concrete01 material, which implements the Kent-Scott-Park stress-strain model [49], while the longitudinal steel reinforcement is modelled with the uniaxial Hysteretic material. The parameters adopted for both stress-strain models are calibrated against experimental data, as discussed in detail in the next paragraph. The fixed-end rotation due to bond slip resulting from strain penetration effects is modelled using a zero-length section element at the end of the beam-column element, as reported in Fig. 4.6. The Bond_SP01 material is assigned to the steel fibres of the zero-length section element for taking into account the cyclic bond slip law proposed by Zhao and Sritharan [50].

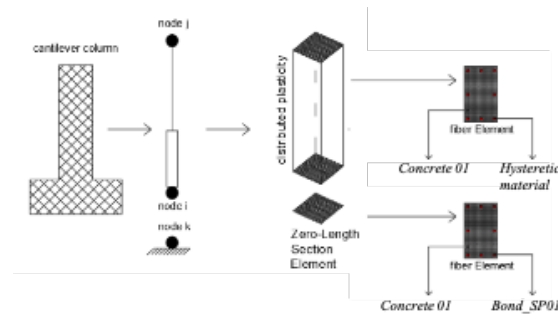


Figure 4.6. RC column modelling using distributed plasticity element.

For the material parameters definition, the yield slip s_y is determined as follows:

$$s_y(mm) = 2.54 \left(\frac{d_b}{8437} \frac{f_{ym}(MPa)}{\sqrt{f_{cm}(MPa)}} 2\alpha + 1 \right) + 0.34 \quad (4.4)$$

where f_{cm} is the average compressive strength of concrete, and α is taken as 0.4 in accordance with the CEB-FIB Model Code 90 [51]. The ultimate slip s_u is taken as $40s_y$, the initial hardening ratio is assumed equal to 0.4 and the pinching factor is 0.6. A fixed restraint is adopted at the base node. Geometric nonlinearities are considered in the model by means of the PDelta geometric transformation. The mass is concentrated at the top of the piers for the modal analyses. The Newton-Raphson solution algorithm is adopted to solve the model nonlinear equations. The FE model has first been calibrated against the results of quasi-static cyclic tests. To perform a robust calibration, the results of the quasi-static cyclic tests described in Section 3 have been complemented with six additional tests on similar structural elements collected from the literature and presented in Di Ludovico et al. [46]. The results of eight experimental tests on cantilever RC columns subjected to constant axial load and cyclic quasi-static lateral loads have been employed for model calibration. Geometrical and mechanical properties of the selected columns are summarized in Table 4.3. Square as well as rectangular columns, reinforced either with plain or deformed bars, were considered. All the columns were tested following the cyclic load protocol reported in Di Ludovico et al. [46], and the observed failure mode was in each case controlled by flexure.

The load protocol adopted for the numerical simulations is reported in Table 4.4 in terms of imposed DR and number of repetitions for each cycle up to a DR=4.8%, which is assumed to represent a limit value for the complete damage of the pier. This loading protocol is widely adopted for quasi-static testing of structural components and equally represent all the identified damage level. A constant axial load ratio equal to of 0.1ν , where ν is the normalized axial load with respect to the area of the cross-section multiplied for compressive strength of the concrete, derived from the tributary mass assigned to the pier, is applied in the model during the numerical cyclic loading analyses

The specimens consisted of a foundation block and a column with shear length of 1500 mm. Columns with three different cross section are herein considered: (1) square 300 x 300 mm; (2) rectangular 300 x 500 mm; and

Table 4.3. Geometric and mechanical parameters for selected tests on RC columns for model validation (*tests from Di Ludovico et al.

Specimen	*R300P-	*R500P-	*R500P-	*S300P-	R300D-	*R500D-	S300D-
	c	c	c-bis	c	c	c	c
b (mm)	500	300	300	300	500	300	300
h (mm)	300	500	500	300	300	500	500
f_{cm} (MPa)	18.8	18.8	28.8	18.8	18.8	18.8	18.8
f_{ym} (Mpa)	330	330	330	330	520	520	520
Type of bars	P	P	P	D	D	D	D

Table 4.4. Load protocol for the cyclic pushover.

Pushover cycle	IDR (%)	Imposed displacement (mm)	Number of repetitions for each cycle
I	0.40	6.0	3
II	0.80	12.0	3
III	1.20	18.0	3
IV	1.60	24.0	3
V	2.40	36.0	3
VI	3.20	48.0	3
VII	4.80	72.0	3

(3) rectangular 500 x 300 mm. Bars with 12 mm diameter were used as longitudinal reinforcement, and 8 mm diameter ties spaced at 150 mm were adopted as transverse reinforcement. Information on specimens' geometry and mechanical properties of steel and concrete are reported in Table 4.4. In details, Table 4.4 reports: the cross-section base, b ; the cross-section height, h ; the compressive strength of concrete, f_{cm} ; the yielding strength of steel reinforcement, f_{ym} ; the type of rebars (plain or deformed). The original notation of specimen is XNY-z, where X refers to the columns cross section shape (S for square and R for rectangular), N denotes the cross-section depth, Y identifies the type of reinforcement (D for deformed bars and P for plain rebars), and z identifies the type of horizontal action applied to the column (c for cyclic test). Parameters for the steel stress-strain relationship adopted in the FEM are generalized from mean experimental values of mechanical properties reported in [46]. The peak hardening strength is taken as $1.3 f_{ym}$, the elastic modulus is assumed equal to 200 GPa, the strain at peak strength is taken as $11 \varepsilon_y$, and the post-hardening strain corresponding to a strength degradation of 20% is taken as 6 times the strain at peak strength (i.e., $66 \varepsilon_y$). For the concrete, the strain at peak strength is assumed as 0.004 while the ultimate strain is set to 0.03. These values are set to provide a good accuracy of the FEM model predictions in terms of lateral stiffness against the experimental data for the first cycle ($IDR = 0.40\%$). The comparison between experimental and numerical lateral stiffness is shown in Fig. 4.7 for the seven specimens used for validation. The FEM model is able to provide on average a good estimate of the initial lateral stiffness of the columns. This is fundamental for computing the undamaged fundamental period. The effect of confinement is neglected in the FEM model, due to the lack of detailing of transverse reinforcement in typical existing RC columns considered for the study.

The comparison between numerical and experimental results in terms of base shear vs. imposed displacement for specimens with plain reinforcement and for those with deformed reinforcement are depicted in Fig. 4.8 and Fig. 4.9, respectively. The numerical curves fit quite well with the experimental ones, providing a reliable simulation of the cyclic performance of RC columns. To further investigate on the accuracy of the FEM model with respect to the experimental results, statistics of the error in the es-

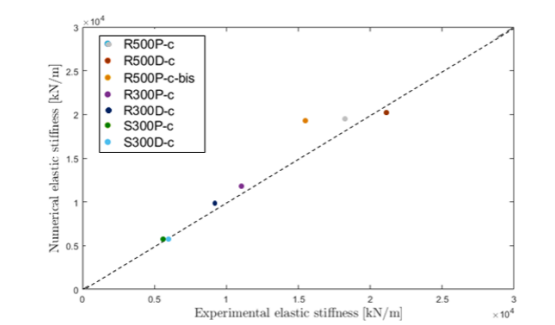


Figure 4.7. Comparison between lateral stiffness from FEM model and experimental curves at IDR = 0.40%.

timated most critical parameters (i.e., peak force, lateral stiffness, energy dissipation, residual drift) have been analysed. Indeed, numerical models provide an approximate representation of real word phenomena and, thus, simulations invariably suffer from a certain level of inaccuracy. In terms of peak force evaluated for each cycle of the pushover, the error between numerical and experimental test has a mean value of 9% with a covariance (CoV) of 3.6%. The comparison of numerical and experimental lateral stiffness (taken as the peak-to-peak stiffness at each cycle of the pushover) gives an average error of 19% (CoV 15%). The average error associated to the residual drift ratios is 40% with a CoV of 26%. Finally, the average error on the hysteretic energy is 29% with a CoV of 18%.

The methodology discussed before is adopted to derive ranges of variation of damage measures (DMs) for a dataset of RC columns through the experimentally validated FEM tool previously presented. The dataset consists of RC columns with cross-section dimensions of 300 x 300 mm and a height of 1500 mm. Five different values of concrete compressive strength (f_{cm}), three values of steel yielding strength (f_{ym}), and six layouts of longitudinal rebars (comprising both numbers of rebars in the cross-section and their diameter) are considered, as reported in Table 4.5. All possible combinations of the selected parameters are analysed, resulting in 90 column configurations. The longitudinal reinforcement ratio ρ is also reported for each geometric configuration. All combinations of random variables have been considered for populating the dataset. For this preliminary applica-

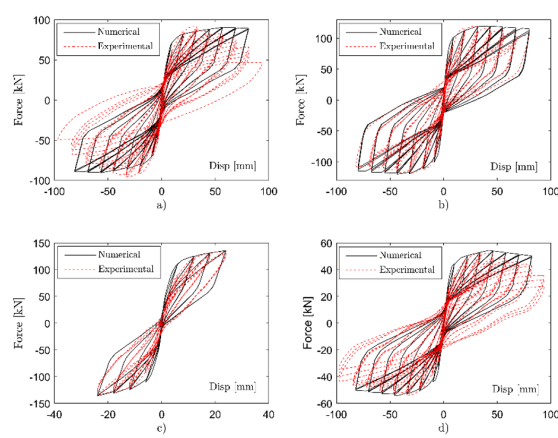


Figure 4.8. Comparison between numerical simulation and experimental test for RC columns with plain rebars: (a) R300P-c, (b) R500P-c, (c) R500P-c-bis, (d) S300P-c.

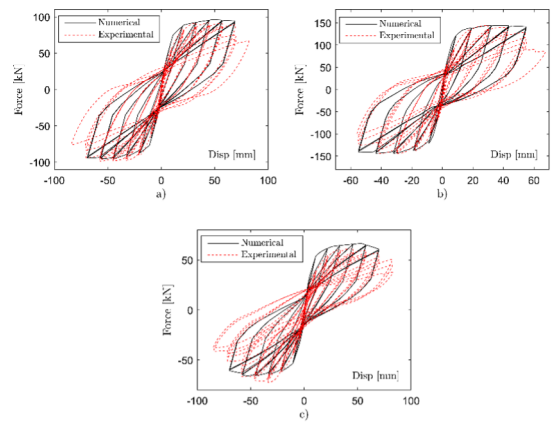


Figure 4.9. Comparison between numerical simulation and experimental test for RC columns with deformed rebars: (a) R300D-c, (b) R500D-c, (c) S300D-c.

tion, variations of DMs for the dataset are considered for a constant axial load ratio of 0.1. According to the methodological framework proposed, a FEM model is generated for each column of the dataset. Modal analysis is carried out to identify the modal periods in the undamaged configuration. Then, a first cyclic pushover is performed for the first imposed IDR according to the load protocol discussed in the experimental section (i.e., IDR = 0.4%). At the end of the pushover, a new modal analysis is carried out to assess the fundamental period (i.e., $T(\text{IDR})$). Furthermore, the residual drift ratio and the lateral stiffness are also estimated (i.e., $dr(\text{IDR})$ and $k(\text{IDR})$). The dissipated hysteretic energy is also computed to define the Park and Ang DI associated with each imposed IDR. Then, a new cyclic pushover is performed up to the second IDR (i.e., IDR = 0.8%), following the load protocol in Table 4.5, and the variation of DMs associated with the imposed IDR is again evaluated. The sequence of analysis is repeated up to an imposed drift ratio of 4.8%, which is herein assumed as an IDR threshold for the structural collapse.

Table 4.5. Variability of geometrical and mechanical properties in the dataset.

Geometry			
(mm x mm)	n.bars [-]	φ [mm]	ρ [%]
300x300	4	6.0	0.5
	6+2	12	1.0
	6+2	14	1.4
	6+2	16	1.8
	2.40	6+2	2.3
	3.20	6+2	2.8
f_{cm} [MPa]	10-15-20-25-30		
f_{ym} [MPa]	315-375-430		

The variation of the selected DMs as a function of the imposed IDR and the damage level is investigated for the dataset of 90 RC columns. Reports the computed Park and Ang DI for all columns in the dataset as a function of the imposed IDR (e.g., Minor Damage = DL1, Moderate Damage = DL2, Severe Damage = DL3, Collapse = DL4). The figure shows that the Park & Ang DI is similar for all numerical simulation at

the same imposed IDR, and it is not significantly affected by variations in section geometry or mechanical properties of materials. For interstorey drift ratios smaller than 0.8% the columns experience a slight or minor damage and is repairable. When the interstorey drift is greater than 1.2%, the damage level is moderate but still repairable, whereas drift ratios exceeding 2.4%, the structural damage is severe and not repairable. In terms of fundamental period elongation (ΔT) derived from natural periods, the numerical data collected for each damage level can be well approximated with a right skewed lognormal distribution for DL1 and DL2, as shown in Fig. 4.10. Conversely, this approximation is less effective for DL3 and DL4. Mean and lognormal standard deviations for the distributions associated with the period elongation are reported in Table 4.6. The period elongation is computed as the percentage of variation of the fundamental period in the damaged condition for a certain IDR with respect to the undamaged (i.e., elastic) fundamental period.

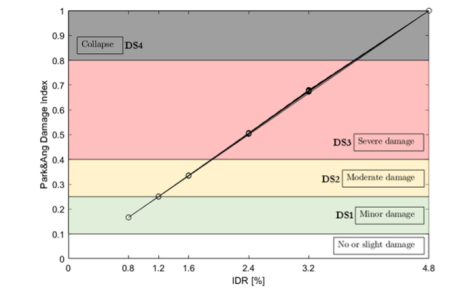


Figure 4.10. Correlation between imposed IDR and Park and Ang damage index for the case-study columns (90 elements).

Ranges of variation of period elongation derived for the dataset are depicted in Fig. 4.12 for each damage level. In detail, the range of variation defined as the 16th – 84th percentiles are reported in the plot along with the mean value. The plot indicates that a period elongation less than 13% with respect to the elastic period can be associated to a minor damage for RC columns. Conversely, period elongation up to 40% can represent a moderate to severe structural damage. Period elongation greater than 40% can be associated to severe damage or collapse. However, a significant overlap among ranges of variation of the period elongation for different damage

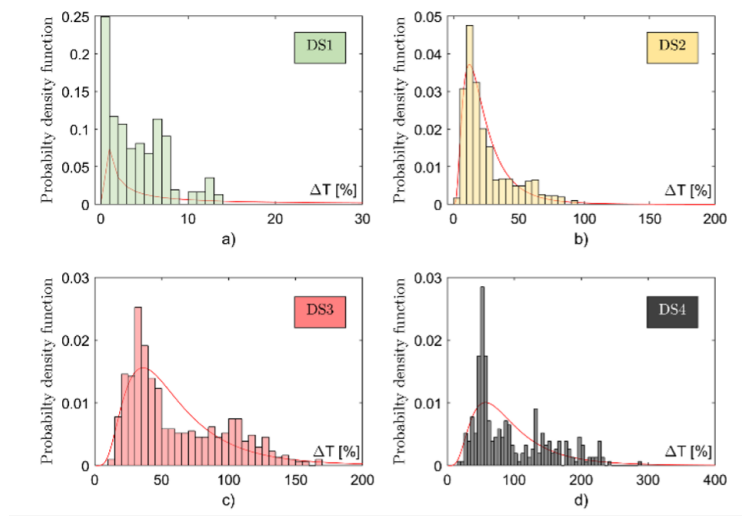


Figure 4.11. Distribution of period elongation for each damage level: a) DL1; b) DL2; c) DL3; d) DL4.

Table 4.6. Parameters of lognormal distributions associated with the period elongation for DL.

Damage Level	Probability distribution	Variable	Value of fitting parameters
DL1	Lognormal	ΔT	$\mu = 1\%$, $\sigma = 5.30$
DL2	Lognormal	ΔT	$\mu = 11\%$, $\sigma = 0.69$
DL3	Lognormal	ΔT	$\mu = 30\%$, $\sigma = 0.59$
DL4	Lognormal	ΔT	$\mu = 49\%$, $\sigma = 0.58$

levels is generally observed for the dataset of columns herein investigated. This, along with the large scatter of results, can prevent the correct identification of the damage level based on the monitoring of such DM. The range of variation of residual drift ratios has been also analysed and plotted in Fig. 4.13 for each defined damage level. It is observed that the ranges of variation for each damage level are not overlapped for the case of residual drift ratios, allowing for an unbiased damage quantification. Fig. 4.13 also reports thresholds for the classification of damage levels identified by the FEMA 356 [52]. The standard identifies four damage levels associated with the residual drift, as reported in Table 6. DL1 corresponds to a residual drift of 0.2%, DL2 corresponds to a residual drift of 0.5%, DL3 is achieved for a residual drift of 1% and, finally, for DL4 the range of residual drift is between 1% and 4% depending on the inelastic capacity of the system.

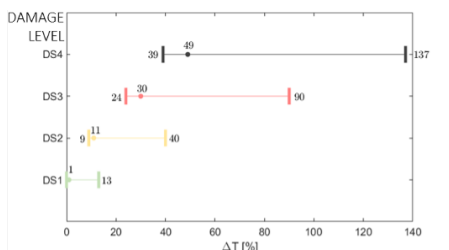


Figure 4.12. Ranges of variation of period elongation for each damage level.

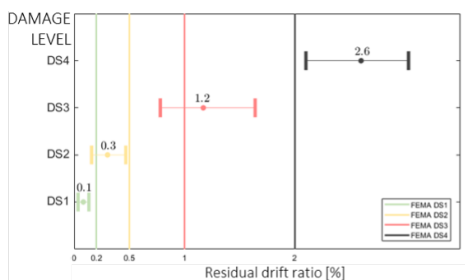


Figure 4.13. Ranges of variation of residual drift ratios for each damage level and comparison with FEMA 356 thresholds.

For DL4, the threshold on residual drift is assumed equal to 2%, assuming a moderate ductility for the selected non-conforming columns adopted

as case-study. The lower bounds (16th percentile) of the range of variation of residual drift from the numerical analysis is also reported in Table 4.7. The comparison between numerical results and FEMA thresholds shows that the numerical model generally provides a safe estimation of residual drifts associated to each damage level. Only for the collapse damage level, the FEMA threshold is slightly lower than the 16th percentile of the numerical data distribution. It should be noted that the definition of damage classification is different between FEMA and Park and Ang, as the latter refers to structural damage only. However, a quite good agreement between the two damage level classifications is recognised, attesting the soundness of the proposed methodological framework.

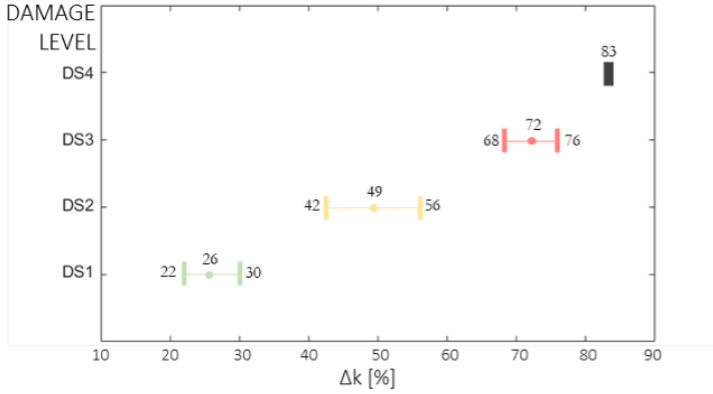
Table 4.7. Damage Levels classification based on the residual story drift ratio according to FEMA 356 and comparison with lower bound values from numerical results.

Damage Level	Residual drift ratio	Lower bounds of residual drift ratios (numerical analysis)
	FEMA	
DL1	0.20%	0.08%
DL2	0.50%	0.20%
DL3	1.00%	0.80%
DL4	High ductility systems	-
	4.00%	
	Moderate ductility systems	2.10%
	2.00%	
Low ductility systems	-	
1.00%		

The columns' lateral stiffness degradation is computed as $\Delta k = 1 - k_i/k_0$, where k_0 is the initial lateral stiffness and k_i the lateral stiffness at the i -cycle (i.e., $k(\text{IDR})$), as shown in Fig. 4.14. Ranges of variation of stiffness degradation for each damage level are plotted in Fig. 4.15. As previously observed for residual drift ratios, no overlap among ranges of variation of the stiffness degradation at different damage levels is found. Based on numerical results, a stiffness degradation ranging between 22-30% can be associated to a minor structural damage, while a stiffness degradation from 42% to 56% indicates a moderate damage level. A stiffness reduction in the range between 68%-76% means a severe damage, and

degradation greater than 83% is associated with the structural collapse for the dataset of RC columns.

Figure 4.14. Ranges of variation of stiffness degradation for each damage level.

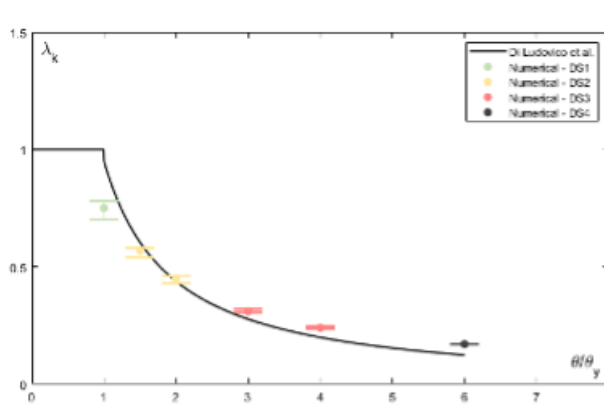


The trend of lateral stiffness degradation herein derived is compared with the stiffness degradation model proposed in Di Ludovico et al. [53]. The authors proposed an empirical model that relates the stiffness degradation factor, $\lambda_k = k_i/k_0$, with the ductility experienced by RC columns, as follows:

$$\lambda_k = 1 - \left[1.07 - 1.15 \left(\frac{\theta}{\theta_y} \right)^{-0.92} \right] \text{ for } 1.1 < \frac{\theta}{\theta_y} \leq \theta_u/\theta_y \quad (4.5)$$

where θ is the columns chord rotation θ_y is the chord rotation at yielding; θ_u is ultimate chord rotation. The model proposed by Di Ludovico et al. [53] is compared with the stiffness degradation ranges derived from numerical analyses in Fig. 4.15 as a function of the ratio θ/θ_y . The comparison shows a perfect agreement between the empirical model and the results derived from numerical analyses on the dataset of RC columns herein considered, confirming the goodness of the numerical simulation for assessing the changes in DMs associated with the increasing seismic damage.

Figure 4.15. Stiffness degradation from numerical analyses on the dataset and comparison with Di Ludovico et al. model for the stiffness modification factor



4.3 RC Frame

4.3.1 Experimental study

The present section investigates the effect of seismic damage experienced by structural and non-structural components on the modal properties (i.e., fundamental frequencies and periods) of full-scale 2D two-storey reinforced concrete (RC) frames through experimental pseudo-dynamic tests. Operational Modal Analysis (OMA) is performed on full-scale two-storey 2D RC frames with masonry infill walls tested under pseudo-dynamic tests simulating seismic excitation [54]. The frame represents the perimeter frame of a real building located in the L'Aquila municipality that was heavily damaged during the 2009 earthquake. Two frame configurations are considered, with different infill walls boundary conditions (i.e., three-side and four-side). OMA is performed before and after the pseudo-dynamic tests to catch variations in modal properties due to damage. The specimens adopted for the OMA are presented in Del Vecchio et al. [54] as F2_3S_M and F2_4S_M. The geometrical and mechanical properties of the specimens are briefly reported herein. The specimens are 6.86 m high and 4.50 m long. The interstorey height is 3.10 m and the foundation block

is 0.56 m high. The square columns, $400 \times 400 \text{ mm}^2$, are reinforced with 8 ϕ 16 mm longitudinal bars and ϕ 8 mm transverse reinforcement 250 mm spaced. The beams cross-section has a 500 mm height and 400 mm width, and is reinforced with 6 ϕ 16 mm and 4 ϕ 16 mm bars at top and bottom, respectively. The beam-column joint panels have no transverse reinforcements as commonly observed in existing buildings in the Mediterranean area. For the beam-column joints in contact with the actuators (left side of the frame), cross-section enlargement and steel profiles reinforcement are locally adopted to avoid punching failure due to the concentrated loads, as visible in Fig. 4.18. The frame F2 adopted for the OMA has been casted and cured in laboratory conditions and it has been tested twice with different infill wall configurations, as discussed in detail in the next. The main characteristics of the frame are summarised in Table 4.8. The frame has been built with a medium quality concrete. Results from compressive tests revealed an average concrete compressive strength of about 19 MPa at first storey and 14 MPa at second storey [54]. Hollow clay brick infill walls are used at both floors. Square bricks with 250 mm side and 200 mm thick are adopted. A 10 mm joints of M10 class mortar are used to build the infill walls simulating a three-sides boundary condition with a 5 mm gap between the wall and the upper beam. The test has been named F2_3S_M, where F2 is the name of the frame, 3S stays for three-side boundary condition, M stays for mortar only. In test F2_3S_M the specimen has been tested up to a ground motion intensity of 125%. At the end of the test, the masonry infill walls have been demolished and re-built with a four-sides boundary condition. A third pseudo-dynamic test sequence, named F2_4S_M, is then performed on the frame up to a ground motion intensity of 150%. The same steel is adopted for longitudinal and transverse reinforcement, having an average yielding strength of 535 MPa. The mechanical characterization tests on infill wall samples showed a shear strength of about 0.35 MPa and a shear modulus of 1063 MPa, a compressive strength of 2.59 MPa in the direction parallel to the holes and a compressive strength of 1.91 MPa in the orthogonal direction to the holes [54].

The pseudo-dynamic tests on the frame are performed as discussed in detail in Del Vecchio et al. [54]. Imposed storey displacement histories are derived from numerical analyses on the whole RC building subject

Table 4.8. Test description for specimen F2.

Test ID	Infill walls	Notes
F2_3S_M	Connected to frame with mortar on three sides, with a gap between the upper beam and the wall	After pseudo-dynamic test, the infill walls are demolished and re-built
F2_4S_M	Connected to frame on four sides with mortar	The frame is the same of previous test, with new infill walls

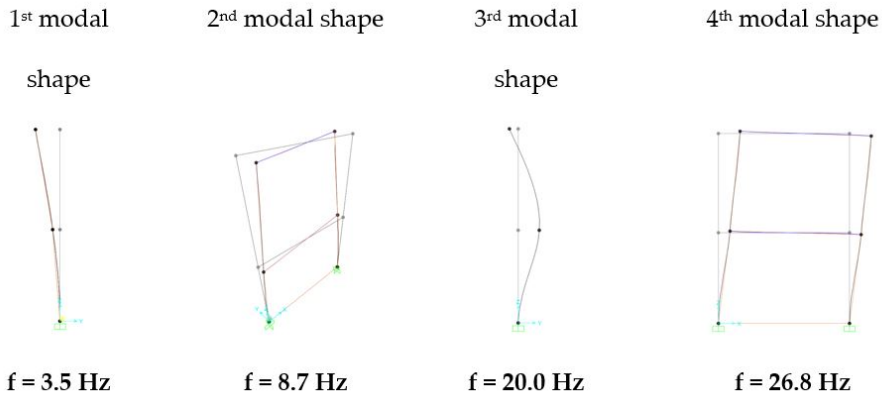
to ground motion of increasing intensity. Further details of the pseudo-dynamic tests can be found in the reference paper and are not reported herein for the sake of brevity. The AQG record in the Est direction (peak ground acceleration $PGA=0.45$ g) of the 2009 L’Aquila earthquake is used as input acceleration. The loading sequence consists of pseudo-dynamic tests of increasing intensities (i.e., 10%, 25%, 50%, 60%, 75%, 100%, 125%, 150%), as reported in Table 4.9. OMA are performed at the beginning of the loading sequence, representing the undamaged condition, and at the end of the loading sequence, representing the damaged condition. It should be noted that the OMA is performed on the specimen without actuators and jacks to avoid undesired constrain effects. This makes not possible the monitoring of dynamic properties variation at different earthquake intensities. For test F2_3S_M, an additional OMA is performed after the demolition of the infill walls to record the dynamic properties of the bare frame

OMA is performed by using unidirectional piezoelectric accelerometers having sensitivity 10 V/g and full scale of $\pm 0.5g$. For the design of the sensor’s layout, modal analysis is performed on a sample specimen with the software SAP2000. The modal shapes of the specimen are shown in Fig. 4.16, along with the associated fundamental frequencies. In detail, the first three modal shapes for the 2D specimen are related to out-of-plane mechanisms, while the fourth mode is in-plane. Based on this preliminary analysis, both in-plane and out-of-plane modes are monitored.

The sensors layout adopted for the tests is depicted in Fig. 4.17 along

Table 4.9. Loading sequences.

Intensity [%]	PGA [g]	F2_3S_M	F2_42_M
0	-	OMA	OMA
10	0.045	-	-
25	0.112	-	-
50	0.223	-	-
75	0.335	-	-
100	0.558	OMA + OMA without infill walls	-
150	0.669	-	OMA

**Figure 4.16.** Modal shapes for the 2D RC frame specimens.

with their recording direction. A total of six accelerometers are used, three for the in-plane direction and three for the out-of-plane direction respectively. Sensors are located at the two storey levels and the mid-height of the second storey column to further catch the experimental modal shapes.

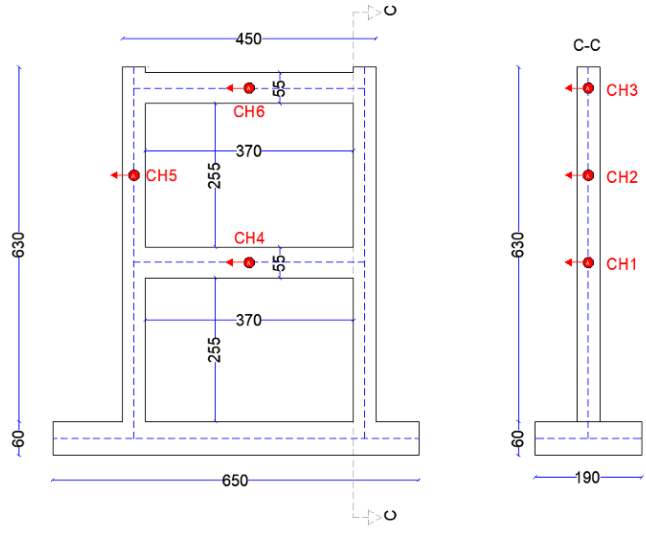


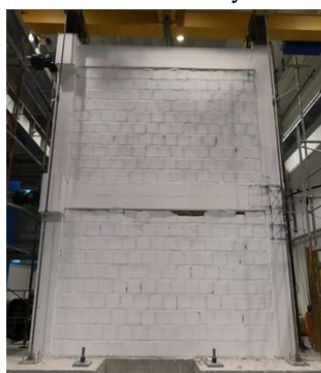
Figure 4.17. Accelerometers layout for OMA.

The damage experienced by the specimens at the end of the two loading sequences is shown in Fig. 4.18. A detailed description made by Del Vecchio et al. [54] of the damage occurred during the loading sequences is also reported in Table 4.10 and Table 4.11, along with the peak drift ratio reached at each storey level in the positive and negative loading directions, respectively. The damage observations have been also correlated by Del Vecchio et al. [54] to the damage scale proposed by Cardone and Perrone for non-structural components [45]. In test F2_3S_M only damage to non-structural components is achieved. The infill walls cracking started at a ground motion intensity of 50% (DL1), and the crushing of corner bricks has been observed at 125% AQG (DL2), when the test was stopped and the infill wall was demolished and rebuilt. Similarly, in test F2_4S_M the major damage was concentrated on non-structural components. The infill walls diagonal cracking started at a 75% intensity (DL1) and reached the

crushing of almost all bricks in contact with the upper beam at a 150% intensity (DL2/DL3). At 125% AQG, a minor sub-horizontal cracking at the top of first storey right column was also observed, probably due to the full development of the infill action in the four-sides boundary condition [54].



F2_3S_M



F2_4S_M

Figure 4.18. Damage condition at the end of the loading sequences for F2_3S_M and F2_4S_M.

Table 4.10. Pseudo-dynamic test results and damage description for F2_3S_M (from Del Vecchio et al.)

ID (-)	Intensity (%)	PGA	Floor	Peak Drift		Observed damage	Damage Level
				+	-		
F2_3S_M	10%	0.045	1	0.01	0.01	No damage	DL0
			2	0.01	0.00		
	25%	0.112	1	0.02	0.02	No damage	DL0
			2	0.01	0.02		
	50%	0.223	1	0.09	0.11	Infill-frame separation	DL1
			2	0.06	0.06	Light diagonal cracking of infill	DL0
	75%	0.335	1	0.18	0.13	No damage	DL1
			2	0.19	0.10	Infill-frame separation Light diagonal cracking of infill	DL1
	100%	0.446	1	0.30	0.19	Infill-frame separation Significant diagonal cracking of infill	DL2
			2	0.31	0.20	and crushing of corners Significant diagonal cracking of infill	DL2
	125%	0.558	1	0.37	0.26	and crushing of corners Crushing of some bricks	DL2
			2	0.41	0.35	Crushing of some bricks	DL2

Table 4.11. Pseudo-dynamic test results and damage description for F2_4S_M (from Del Vecchio et al).

ID (-)	Intensity (%)	PGA	Floor	Peak Drift + -		Observed damage	Damage Level
F2_4S_M	10%	0.045	1	0.00	0.00	No damage	DL0
			2	0.00	0.01		
	25%	0.112	1	0.01	0.01	No damage	DL0
			2	0.01	0.01		
	50%	0.223	1	0.03	0.03	Hairline cracking at the infill-to-beam connection	DL1
			2	0.05	0.03	Infill-frame separation	DL0
	75%	0.335	1	0.07	0.09	Light diagonal cracking of infill	DL1
			2	0.09	0.10	Light diagonal cracking of infill	DL1
	100%	0.446	1	0.14	0.13	Significant diagonal cracking of infill	DL2
			2	0.16	0.16	Significant diagonal cracking of infill	DL2
	125%	0.558	1	0.33	0.22	Significant diagonal cracking of infill Column cracking due to infill action	DL2
			2	0.40	0.26	Significant diagonal cracking of infill Wide diagonal cracking of infill and crushing of some bricks	DL2
	150%	0.669	1	0.52	0.41	Concrete cracking at beam-to joint interface	DL2/DL3
			2	0.62	0.40	Wide diagonal cracking of infill and crushing of some bricks	DL2

Data acquired through output-only modal identification tests before and after damage have been processed using the singular value decomposition of PSD matrix according to the Frequency Domain Decomposition method. As an example, tests records in terms of frequency are plotted in Fig. 4.19 for test F2_4S_M for the in-plane direction before Fig. 4.19(a) and after damage Fig. 4.19(b).

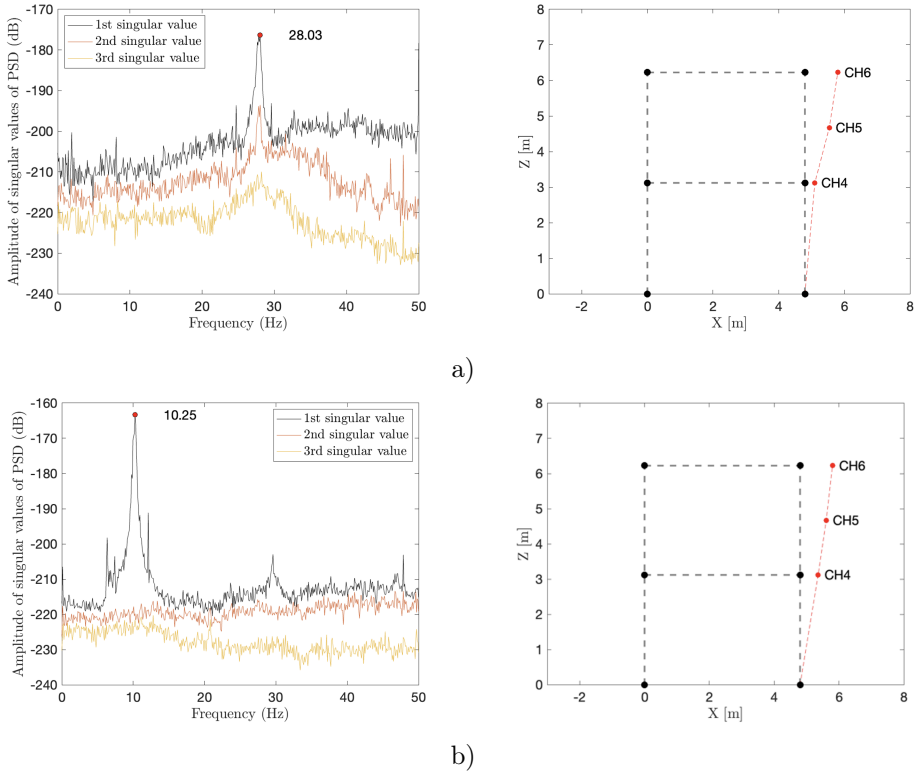


Figure 4.19. a) 1st Singular value of PSD matrix and modal shape of test on F2_4S_M on undamaged configuration; b) 1st Singular value of PSD matrix and modal shape of test on F2_4S_M on damaged configuration

In the plots, the experimental fundamental frequency is highlighted for the two configurations (i.e., 28.03 Hz and 10.25 Hz, for the undamaged and damaged configurations respectively). The experimental modal shape derived from the processing of modal identification tests data are also plotted

for the two configurations. The figure points out the effect of damage experienced by the specimen both in terms of fundamental frequency and modal shape. Same observations can be made for the other records, that are not reported herein for the sake of brevity.

Results from OMA are summarized in Table 4.12 and Table 4.13 for the in-plane and out-of-plane directions, respectively. In detail, fundamental frequency, frequency variation and modal shape parameters are reported in the tables. OMA records for tests F2_3S_M and F2_4S_M allow to effectively point out the effect of seismic damage on dynamic properties in relation with the damage level. For test F2_3S_M, the in-plane mode is significantly affected by damage. The fundamental frequency in the undamaged configuration, equal to 17.6 Hz, is reduced after the loading sequence, reaching a value of 9.5 Hz. This means that the damage occurred in infill walls, classified as DL2, reduces the fundamental frequency by 63%. The OMA performed on the frame after the demolition of damaged infill walls allows to assess the contribution of the structural components to the overall fundamental frequency. From OMA records, the fundamental frequency of the bare frame is 6.5 Hz. Given the absence of observed damage to the structural components in F2_3S_M, this frequency can be considered as the frequency of the undamaged bare frame which represents 25% of the frequency of the undamaged infilled frame. Hence, it could be derived that the infill walls contribute to 75% of the undamaged frame fundamental frequency. For test F2_4S_M, the fundamental frequencies for the in-plane mode are 28.0 Hz and 10.2 Hz, respectively for the undamaged and damaged configuration. Hence, the damage of infill walls, classified as DL2/DL3, reduces the frequency by 63% as previously observed for test F2_3S_M.

For the first out-of-plane mode, test records from the two tests show that a DL2 damage to infill walls causes a reduction of fundamental frequency ranging from 19% to 23%. For test F2_3S_M, the bare frame frequency, equal to 2.6 Hz, is 77% of the overall frequency of undamaged infilled frame for the out-of-plane mode.

4.3.2 Numerical study

A non-linear FE model with distributed plasticity is developed in OpenSees [47] to simulate the seismic performance of tested frames. A schematic

Table 4.12. Summary of modal identification results via OMA for the first in-plane mode

ID	Configuration	IP 1st Frequency (Hz)	Frequency variation with respect to undamaged frequency [%]	Modal Shape	Peak Drift [%]	Observed damage	Damage Level
F2_3S_M	Undamaged	25.4	-	1.00;0.78;0.49		Significant diagonal cracking of infill and crushing of corners	DL2
	Damaged	9.5	-63	1.00;0.82;0.53	0.41		
	Bare	6.5	-74	1.00;0.83;0.50			
F2_4S_M	Undamaged	28.0	-	-		Diagonal cracking of infills and crushing of some bricks	DL2/DL3
	Damaged	10.2	-63	1.00;0.81;0.56	0.62		

Table 4.13. Summary of modal identification results via OMA for the first out-of-plane mode

ID	Configuration	OOP 1st Frequency (Hz)	Frequency variation with respect to undamaged frequency [%]	Modal Shape	Peak Drift [%]	Observed damage	Damage Level
F2_3S_M	Undamaged	3.4	-	1.00;0.10;0.03		Significant diagonal cracking of infill and crushing of corners	DL2
	Damaged	2.6	-23	1.00;0.70;0.11	0.41		
	Bare	2.6	-23	-			
F2_4S_M	Undamaged	3.4	-	-		Diagonal cracking of infills and crushing of some bricks	DL2/DL3
	Damaged	2.6	-19	1.00;0.69;0.12	0.62		

summary of the numerical model is reported in Fig. 4.20 where the adopted constitutive models of each element and material are depicted, including the rotational spring for the beam-column joint and the truss element for the infill walls for the four-sides configuration. The BeamWithHinges command is used to build forceBeamColumn elements, which allow distributed plasticity to be spread also beyond the plastic hinge region. The solid cross-section of RC elements is uniformly discretised into fibres to closely represent small stress-strain variations. The concrete nonlinear behaviour is simulated with the Concrete01 material, while the longitudinal steel reinforcement is modelled with the OpenSees uniaxial Hysteretic material. The parameters adopted for both stress-strain models are calibrated against experimental data reported in Del Vecchio et al. [54]. The beam-column joints are modelled as rotational springs with a *Pinching4* material, adopting the model proposed by De Risi et al. [55]. According to the model, the backbone of the beam-column capacity curve is represented as a four linear branches curve defined by the critical points reported in Table 4.14 in terms of shear stress (τ_j) and rotation (γ).

Table 4.14. Beam-column joint backbone critical points.

Backbone point	$\tau_j [MPa]$	γ [%]
Cracking	$\tau_{j,cr} =$ $0.29\sqrt{f_c}\sqrt{1 + 0.29\frac{P}{A_j}}$	0.04
Pre-peak	$0.85\tau_{j,max}$	0.17
Peak	$\tau_{j,max} = 0.5\sqrt{f_c}$	0.19
Residual	$0.43\tau_{j,max}$	4.41

Where f_c =concrete compressive strength, P= axial load, A_j =beam-column joint panel area. Equivalent moments for the rotational spring characterization are then computed adopting the following expression:

$$M_j = \tau_j A_j \frac{1}{\frac{1-h_c/2L_b}{jd_b} - \frac{1}{2L_c}} \quad (4.6)$$

with h_c the column cross-section height, L_b the beam length, jd_b the beam internal level arm, L_c the column height. For the beam-column nodes in contact with the actuators, an indefinitely elastic law is used to

account for the cross-section enlargement and steel profiles reinforcement locally adopted in the test specimens to avoid local punching failure due to the concentrated loads. The FE model neglects the shear behavior of RC beams and columns given the negligible damage occurred during the tests due to shear. The nonlinear behavior of the infill panels is reproduced by adopting the three-strut model suggested by Chrysostomou et al. [56] in both directions, with struts acting in compression only. Truss elements with Pinching4 material are used both for central and off-struts. The overall lateral performance of the infill wall is assessed following the multilinear model proposed by Panagiotakos and Fardis [57], as reported in Table 4.15. The unloading branch has a slope K_1 up to force equal to $0.1F_u$, while the shape and the width of full unloading-reloading loops is controlled by parameters $\gamma = 0.8$ and $\alpha = 0.15$. The overall lateral capacity is distributed among the three struts as proposed by Chrysostomou et al. [56] and Verderame et al. [58]. For F2_3S_M specimen, the upper off-strut is removed from the model to take into account the 5mm gap between the infill wall and the upper beam as suggested in Del Vecchio et al. [54].

Table 4.15. Infill's backbone critical points.

Backbone of infills	K [MPa]	F [%]
Cracking	$K_1 = GLt/H$	$F_{cr} = \tau_{cr}Lt$
Pre-peak	$K_2 = 0.03K_1$	$F_{peak} = 1.3Lt$
Peak	$K_3 = -0.01K_1$	$F_u = 0.1F_{peak}$

*with L, H and t the length, height, and thickness of the infill panel and G and τ_{cr} the shear modulus and cracking stress experimentally measured.

Nonlinear time-history analyses (NLTH) are carried out imposing as input data the displacements recorded at the two storey levels during the pseudo-dynamic tests. A mass of 5 tons is applied at the first storey level of the model, whereas a mass of 2.5 tons is applied on second storey to simulate the mass distribution of test specimens. The results of NLTH analyses in terms of hysteretic capacity-curves for the two frames are plotted in Figure 4.21 in terms of base shear and first storey interstorey drift ratio (IDR). In Figure, numerically derived curves are compared with the experimental results from pseudo-dynamic tests (black lines). The com-

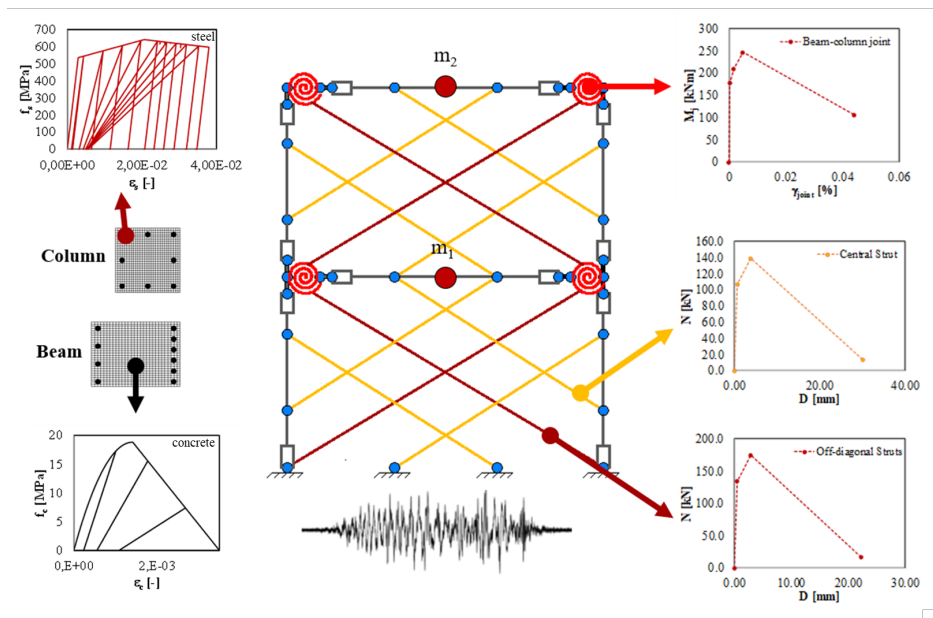


Figure 4.20. Schematic view of the FE model with 4-side infills walls

parison shows a very good agreement between numerical and experimental curves in terms of lateral stiffness, lateral strength, and pinching. Markers are also reported in Figure 4.21 representing the achievement of selected damage mechanisms for the infill walls, namely the infill cracking and crushing. In F2_3S_M, the diagonal cracking and crushing of the first storey infill panel are achieved in the numerical model for IDR=0.06% and IDR=0.26%, respectively. These results are in agreement with the experimental damage observed during the 50% and 125% AQG sequences, respectively. No damage to the RC frame is recorded in the FE model, in agreement with the experimental observations. Similarly, in test F2_4S_M the infill walls cracking and crushing are recorded respectively at IDR=0.07% and IDR=0.40%, compatibly with the observed damage in 75% AQG and 150% AQG experimental sequences. The comparison attests the reliability of the FE models in catching the experimental damage experience by both structural and non-structural components, other than the lateral stiffness degradation due to occurred damage.

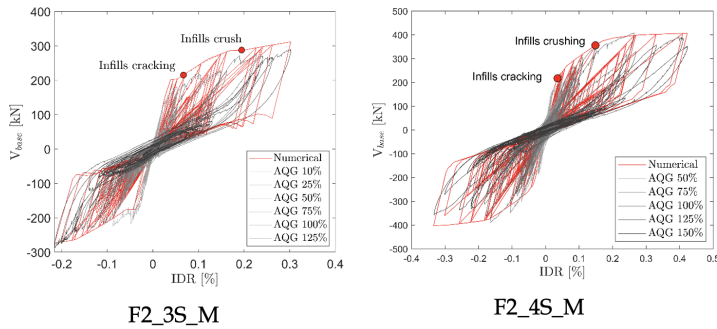


Figure 4.21. Numerical vs experimental comparison of hysteretic curves.

In terms of fundamental frequencies, numerical and experimental results are compared in Table 4.16 for all the configurations where the OMA has been performed. Data are reported for the first in-plane mode, which is more sensitive to the imposed loading condition. Table 4.16 also reports the error between numerical and experimental records. For the undamaged infilled configuration, the numerical model provided fundamental frequencies that underestimates the experimental data by 1-2%. In the damaged configuration, the model underpredicts the experimental data by 5-10%.

For the bare frame configuration (F2_3S_M) the numerical model slightly underestimates the fundamental frequency by 4%. Hence, the FE model is also able to capture the variation on fundamental frequency due to damage occurred during the shaking sequences.

Table 4.16. Comparison between numerical and experimental frequencies for the in-plane mode.

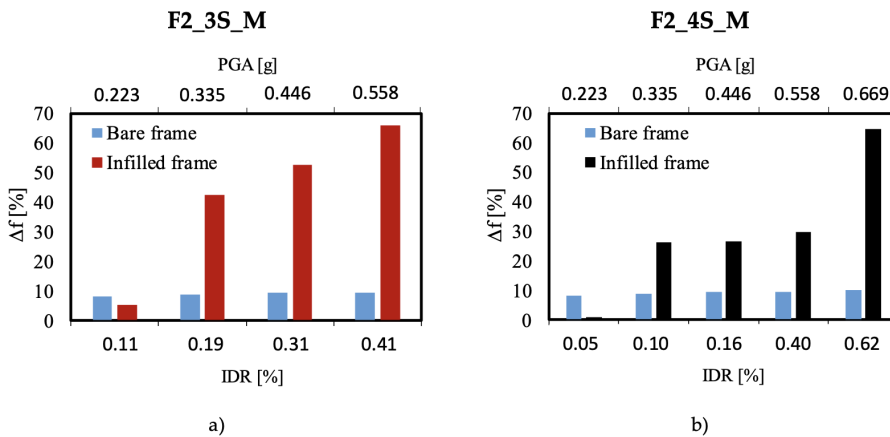
ID	Configuration	Experimental frequency (Hz)	Numerical frequency (Hz)	Δ (%)
F2_3S_M	Undamaged	25.4	24.9	-2
	Damaged	9.5	8.5	-1
	Bare	6.5	6.3	-4
F2_3S_M	Undamaged	27.9	27.4	-1
	Damaged	10.2	9.7	-5

The validated FE model has been used to assess the variation of fundamental frequencies due to structural and non-structural damage in tested specimens for increasing ground shaking intensity. Indeed, OMA records only provide information for the damaged configuration at the end of all the pseudo-dynamic sequences. Numerical analyses are adopted to complete the missing information from experimental tests in terms of frequency variation for each earthquake intensity. In detail, the frequency at damaged condition is extrapolated from the numerical model after each NLTH analysis. Furthermore, the analyses are performed both on the infilled and bare frame configurations to independently assess the contribution of structural and non-structural damage to the overall frequency variation. Table 4.17 summarises the results achieved for test F2_3S_M and F2_3S_M for the first in-plane mode, which has been demonstrated to be more sensitive to the imposed loading condition. In the Table 4.17, the numerical results are associated to the experimentally observed damage level for that earthquake intensity. Fig. 4.22 also depicts the comparison of variation in fundamental frequency for bare and infilled frames as a function of the PGA and of the IDR. The analysis on the bare frame attests that a ground shaking up to an intensity of 150% (PGA=0.669g) induces in the frame a variation in fundamental frequency less than 10% (i.e., 0.7 Hz) with

respect to the undamaged frequency, attesting a very minor structural damage. Furthermore, a variation of 8.3% in fundamental frequency is observed even for an earthquake intensity of 50% (PGA=0.223g). Conversely, in terms of non-structural damage, significant variations in fundamental frequencies are observed for both specimens for an earthquake intensity of 75% (PGA= 0.335g), which corresponds to an experimentally observed DL1. However, in terms of frequency variation, a significant difference is observed between tests F2_3S_M and F2_4S_M for the same PGA, as shown in Fig. 4.23. Indeed, test F2_3S_M globally shows a greater variation of natural frequency with respect to test F2_4S_M due to the higher flexibility caused by the 5mm gap between the infill walls and the frame. Indeed, for the same PGA, specimen F2_3S_M reached higher drift ratios if compared to F2_4S_M. Based on available data, it can be observed that a frequency variation for the first in-plane mode ranging between 0.7% and 5.2% is associated with a DL0/DL1 for non-structural components of both specimens (PGA<0.223g, IDR<0.11%). At intermediate earthquake intensities, the two specimens behaved slightly differently in terms of frequency variation. Indeed, specimen F2_3S_M experienced a frequency variation of 42.5% at DL1 (PGA=0.335g, IDR=0.19%) and a variation of 52.6%-65.9% at DL2 (PGA=0.446-0.558g, IDR=0.31-0.41%). Conversely, specimens F2_4S_M, having experienced a lower drift demand with respect to F2_3S_M, showed a less significant variation in fundamental frequencies. The frequency variation for PGA ranging between 0.335g and 0.558g is about 26.3%-29.6% (IDR=0.1-0.4%), corresponding to observed DL1 and DL2 in infill walls. A higher frequency variation, equal to 64.6%, is reached with the full cracking of the infill strut classified as DL2/DL3 (PGA=0.669g, IDR=0.62%). Hence, the different boundary condition of infill walls affected both drift demand and natural frequency variation in RC frames subjected to the same earthquake intensity.

Table 4.17. Comparison between variation in frequencies in bare frame and infilled frame F2_3S_M.

Configuration	Earthquake intensity [%]	PGA [g]	Numerical frequency [Hz]	Frequency variation	Damage Level
Bare frame	0	0	6.90	-	-
	50	0.223	6.33	-8.3	DL0
	75	0.335	6.30	-8.7	DL0
	100	0.446	6.26	-9.3	DL0
	125	0.558	6.25	-9.3	DL0
	150	0.669	6.20	-10.1	DL0
Infilled frame F2_3S_M	0	0	24.9	-	-
	50	0.223	23.6	-5.2	DL0/DL1
	75	0.335	14.3	-42.5	DL1
	100	0.446	11.8	-52.6	DL2
	125	0.558	8.5	-65.9	DL2
Infilled frame F2_4S_M	0	0	27.4	-	-
	50	0.223	27.2	-0.7	DL0/DL1
	75	0.335	20.2	-26.3	DL1
	100	0.446	20.1	-26.6	DL2
	125	0.558	19.3	-29.6	DL2
	150	0.669	9.7	-64.6	DL2/DL3

**Figure 4.22.** Comparison of variation in natural frequency between bare and infilled frames with respect to peak ground acceleration.

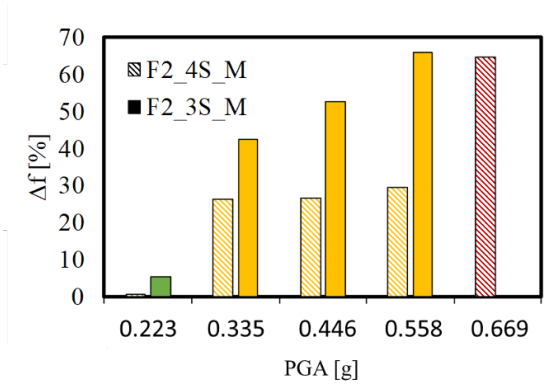


Figure 4.23. Comparison between numerical and experimental frequencies for the in-plane vibration mode

4.4 RC Buildings

4.4.1 Numerical study

In the present section, the numerical framework is adopted to correlate global and local structural damage of a 3D RC building after a seismic event through SHM data. The correlation between the variation of vibration period of RC columns at different damage levels is adopted to correlate the global damage level to the maximum interstorey drift (IDR_{max}) experienced by the structure during an earthquake. Indeed, the relationship between the local damage of single structural members (and their variation in fundamental period) and the global structural damage (and the variation of the fundamental period of the entire structure) has not been assessed yet. The chosen case study is an existing building, located in the L’Aquila municipality, heavily damaged during the 2009 earthquake (Fig. 4.24) The building has a rectangular plan with dimensions 15.60x10.00m and each floor is 3.20 meters high [54]. The building has columns of size 40x40cm for the entire height of the building and, in one direction, ordinary beams of size 40x55cm, while in the other direction wide beams of size 40x20cm, embedded in the floor slab, are used.

The FE model of the building was made in OpenSees [47]. Both column and beam elements are modelled by using *nonlinearBeamColumn*



Figure 4.24. a) Front view of the case study building and b) typical floor plant of the case study building.

elements with a *Hinge – Radau* integration. The length of the plastic hinge, necessary to define the zone within which to concentrate the plasticity of the element, was defined in accordance with [48], considering the following relationship:

$$L_p = 0.08 \frac{h}{2} + 0.22 f_{ym} d_{bar} \quad (4.7)$$

where h is the shear length of the element, f_{ym} is the yield strength of the steel and d_{bar} is the diameter of the reinforcement bars. Then, in the region defined as a plastic hinge, a fibre section with a patch square and a subdivision number equal to 30×30 was assigned for the concrete fibres, while a straight layer with a number of fibres equal to the reinforcing bars present in the cross-section was assigned for the steel fibres. The concrete fibres were assigned a constitutive law with the Concrete01 model whose parameters are 32 MPa for concrete compressive strength and elastic modulus of 31 GPa, while the steel was modelled with the Hysteretic model where the yielding point is 535 MPa in terms of strength and 0.0029 for strain [54]. In the other part of the element, out of the plastic hinge length, an elastic section was assigned. The building is governed by a flexural failure mode; hence the shear behaviour of the columns is not modelled. Nonlinear dynamic analyses are performed through the time history recorded by the EST accelerometer station of L’Aquila in 2009 (AQQ). The chosen time history has been appropriately scaled to simulate

different damage scenarios. Starting from an intensity of 100%, defined as the original signal intensity, the time history has been scaled to 20%, 40%, 60% 80%, 125%, 150% and 200%. Each of these intensities, including the 100% intensity, were applied in the two directions of the structure according to the following loading patterns:

- X
- Z
- $0.03 X + 1.00 Z$
- $X + 0.30 Z$

where the X direction is the direction with the greatest number of spans while the Z direction is a direction with the least number of spans (see Fig. 4.24b). An eigen analysis is performed before and after each nonlinear dynamic analysis to detect the variation of modal properties of the structure. For each nonlinear dynamic analysis, the variation of vibration period (ΔT_{global}) of the structure is recorded, as well as the IDRmax for each storey. These records are compatible with the output data obtained from a long-term SHM system with at least one accelerometer for each floor of the building. The results of the analyses are first discussed as a function of the direction of the ground shaking and of the seismic intensity, then overall results of all the considered scenarios are reported and discussed. Fig. 4.25 shows the IDRmax reached by each column of the case-study building during the ground shaking for an earthquake intensity of 150% and under all the considered loading scenarios (i.e., 1.00X, 1.00Z, 1.00X+0.30Z, 0.30X+1.00Z). It can be noted that, for the case-study building, the IDR reaches maximum values at the lower levels of the structure. Indeed, columns at first and second storey experience a DL3 for all the loading cases, while columns at the third storey reach a DL1 or DL2, depending from the loading scenario. The global structural damage is then evaluated considering the peak and the weighted averaged IDRmax, and the damage level is assigned following the relationships reported in Table 21. Results are summarized in Table 22 for the considered scenarios.

Results are reported in Table 4.18 for a fixed loading scenario (1.00X) under ground shaking of increasing intensity. The peak and average DL_{global}

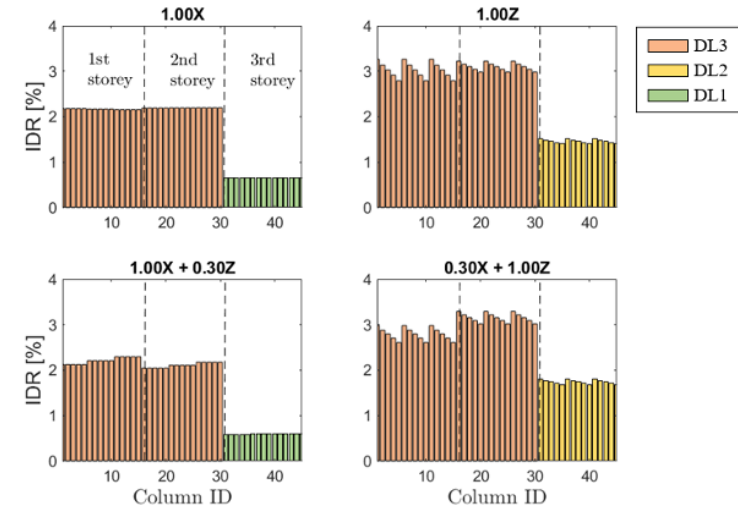


Figure 4.25. Interstorey drift of each column for analysis with 150% intensity of ground shaking.

are reported, along with the variation of vibration period experienced by the building along the X direction after the ground shaking. It can be observed that the average DL_{global} is usually lower than the peak one. For the considered loading scenario, the building reaches a DL4 for an IDR_{max} of 3.92% and with a period elongation of 41.9% with respect to the undamaged configuration. For the loading scenario 1.00X+0.30Z the IDR_{max} and the elongation of period in the X direction show no significant differences with respect to the 1.00X scenario. However, the bidirectional loading affects significantly the mode of vibration of the building in the Z direction.

Data obtained from all the considered loading scenarios and all the chosen earthquake intensities are then analyzed to derive ranges of variation of the period elongation of the building as a function of the global damage level experienced. Results are summarized in Table 4.19 both for peak and average global damage level. Results in terms of period elongation, ΔT , are also plotted in Fig. 4.26 and compared with the ranges of variation derived in Lubrano Lobianco et al. [59] for RC columns. In detail, coloured markers represent the period elongation of the case-study

Table 4.18. Summary of global damage level and correlated period variation for the first loading scenario (1.00 X).

Scenario	Earthquake intensity	IDR_{max}	DL_{peak}	Period variation		
	(%)			(%)	(-)	μ_d
1.00 X	10	0.29	DL0	0.00	DL0	+2.2
	20	0.55	DL1	0.33	DL0	+13.4
	40	1.18	DL1	0.33	DL0	+17.5
	60	1.84	DL2	0.67	DL1	+20.0
	80	2.63	DL3	1.00	DL1	+36.9
	100	2.23	DL3	1.44	DL1	+32.4
	125	1.91	DL3	2.00	DL2	+35.4
	150	2.19	DL3	2.33	DL2	+39.0
	200	3.92	DL4	2.33	DL2	+41.9

building while black plots represent the ranges of variation of vibration period for the columns. It can be noted that for each loading condition (1.00 X, 1.00 Z, 0, 3 X + 1.00 Z, 1.00 X + 0.3 Z) and for each intensity of AQG earthquake the markers fall within the range estimated in the previous study for the RC column, if the DL corresponding to the peak IDR is considered. On the other hand, considering the weighted average value of μ_d and the corresponding DL, only the DL2 and DL3 seems to have a good match between the correlations read on the columns and those for the whole building.

Table 4.19. Summary of natural period variation ranges at different damage levels considering both peak and average value.

Global Damage Level	Period variation			Period variation		
	DL_{peak}			$DL_{average}$		
	16th	84th	Median	16th	84th	Median
DL1	+10.3	+19.1	+17.5	+32.3	+36.6	+35.4
DL2	+28.8	+36.6	+32.7	+32.3	+40.4	+38.9
DL3	+32.4	+38.7	+37.2	+40.9	+42.4	+42.4
DL4	+41.9	+43.8	+42.8	-	-	-

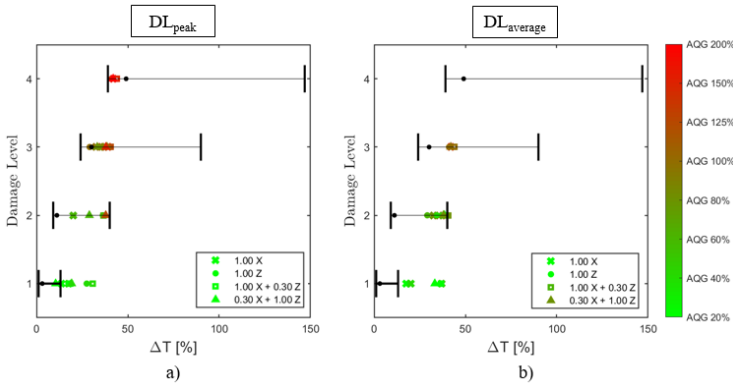


Figure 4.26. Correlation with the a) peak and b) averaged column DS and period variation of the building.

4.5 RC bridge piers

4.5.1 Numerical study

The study aims at tackling the problem of the correlation between information on modal properties derived from SHM data and damage levels occurred in the monitored bridges after a ground shaking. The study focuses on a specific class of bridges, the simply supported Reinforced Concrete (RC) bridges, which represents a very common typology of existing road bridges. Among the failure modes affecting this specific bridge type under seismic excitation, those related to flexural and shear capacity of piers play a relevant role due to different reasons (inadequate flexural strength or ductility, inadequate splice length, inadequate transverse reinforcement, etc.). In this study, the performance of ductile piers governed by a flexural failure mode is investigated. In such a context, the response of the structure is governed by fundamental frequencies depending on the mass of the decks and on the stiffness of the piers [60]. Solid rectangular columns are commonly found in low to moderate height bridges both in the case of single column as well as multiple columns bents [60], so they are experimentally investigated under the assumption that failure modes are governed by flexure without lack of generality of the results. The selected damage can be detected, in principle, by focusing the attention on the vi-

bration response of piers only, so the number of sensors to install and the cost of the monitoring system can be optimized by limiting the observability to those primary structural elements. The significance of monitoring the acceleration response of piers for the selected class of bridges is confirmed by a number of applications [61, 62, 63]. In particular, the measured acceleration response of the piers can be processed in order to perform reliable estimates of its dynamic properties that can be effectively used to assess the structural integrity [64, 65]. Following these results, the present study investigates the influence of different seismic damage scenarios on the dynamic response of a class of ductile RC piers whose geometrical and mechanical properties are based on real surveys carried out on existing Italian RC bridges of the simply supported type. A dataset of 250 rectangular RC bridge piers with solid cross-section has been generated for the numerical simulations. The definition of the RC bridge piers dataset relies on the Latin Hypercube sampling technique and adopts data distributions from the extensive study performed by Zelaschi et al. [66] to characterize the portfolio of existing Italian bridges (1970s-1990s). The study focuses on simply supported bridges following the schematic representation of Fig. 4.27.

Relevant geometrical and mechanical data collected from a real stock of about 458 Italian RC bridges presented in Zelaschi et al. [66] are summarized in Table 4.20. In particular, the type of distribution along with relevant statistics are reported for pier height (h), pier cross section dimensions (B and H , as reported in Table 4.20), steel and concrete mean strength (f_{ym} and f_{cm}). It should be noted that the pier always presents the strong axis in the transverse direction of the bridge. For the steel reinforcement ratio (ρ), a uniform distribution is adopted in the range 0.5%-1.0%. The concrete stiffness is also taken as random variable for the Monte Carlo simulation, randomly selecting the concrete strain at maximum strength of the Concrete01 material in the range 0.003-0.008, based on the outcomes of the model calibration. The distributions of geometrical and mechanical properties for the generated sample of 200 RC piers are plotted in Fig. 4.28. The mass of the bridge deck is computed based on the distribution of the superstructure area and of the average span length, both treated as random variables in the Monte Carlo simulation and reported in Table 4.20. The tributary mass assigned to the generic bridge

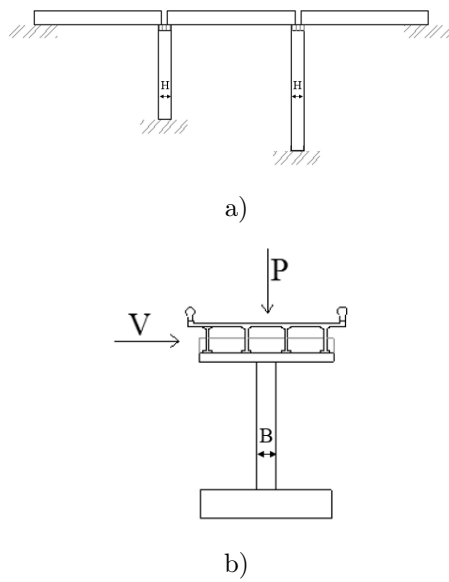


Figure 4.27. Structural scheme of examined bridge and loading scheme: longitudinal profile (a) and transverse profile (b).

Table 4.20. Statistics of relevant geometrical and mechanical properties of existing bridge piers.

Variable	Distribution	Distribution parameters
Pier height h (m)	Lognormal	Mean (log): 1.95 std.: 0.8275
Solid rectangular section Dimension in the bridge transverse direction B (m)	Weibull	Shape: 1.65 Scale: 2.34
Solid rectangular section Dimension in the bridge longitudinal direction H (m)	Weibull	Shape: 0.96 Scale: 2.79
Steel tensile strength f_{ym} (MPa)	Normal	Mean: 504.40 std.: 157.84
Concrete compressive strength f_{cm} (MPa)	Normal	Mean: 40.00 std.: 7.44
Average span length (m)	Normal	Mean: 29.936 std: 12.174
Superstructure area (m^2)	Lognormal	Mean (log): 7.88 std: 0.9087

pier is then computed multiplying the superstructure area, the span length and the typical density of reinforced concrete (i.e., $25 \text{ kN}/\text{m}^3$). The tributary mass is then concentrated at the top node of the pier in the OpenSees model.

Numerical analyses of the tested specimens and a model updating process have been carried out in order to reliably predict the effect of seismic damage on the fundamental modal properties of RC piers. To this aim, the nonlinear behaviour of column-type elements has been modelled in OpenSees [47] through a distributed plasticity model. The input param-

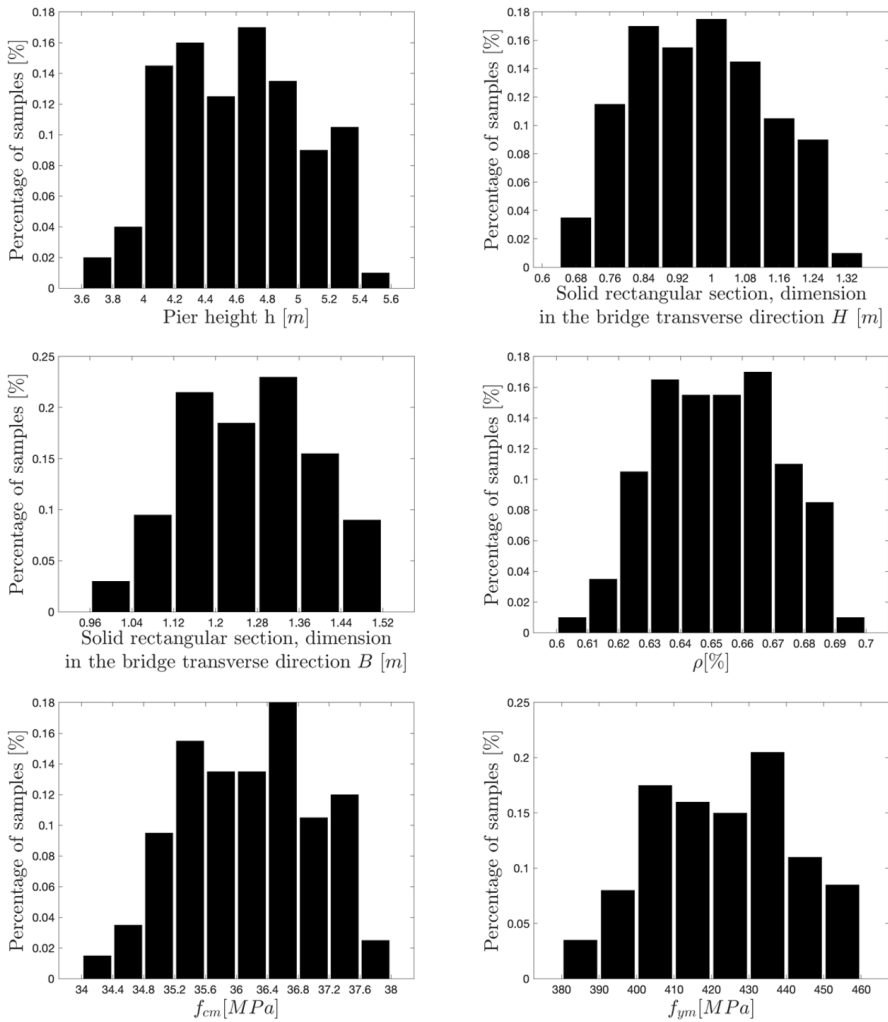


Figure 4.28. Distribution of geometrical and mechanical parameters for the population of 200 RC bridge piers.

eters required for the numerical modelling have been then updated based on the results of the experimental tests presented in Section 3, so that a validated baseline for probabilistic analyses has been set. As mentioned before, the present study focuses on ductile piers governed by a flexural failure mode. However, the approach can be extended to other typical failure mechanisms (i.e., short piers or piers with lap-splicing) if experimental data for model calibration and validation are available to ensure the reliability of numerical simulations. The `BeamWithHinges` command is used to build a `forceBeamColumn` element, which allows distributed plasticity to be spread also beyond the plastic hinge region. For the cantilever column-type element, a single hinge is defined at the base section, and its length is computed as follows [48]:

$$L_{pl} = 0.08L_S + 0.022f_{ym}d_b \quad (4.8)$$

where L_S is the shear length, d_b the longitudinal bars diameter, and f_{ym} the average yield strength of steel.

The solid cross-section of the beam-column element is uniformly discretized into 30 fibres to closely represent small stress-strain variations. The concrete nonlinear behaviour is simulated with the `Concrete01` material, which implements the Kent-Scott-Park stress-strain, while the longitudinal steel reinforcement is modelled with the `OpenSees` uniaxial Hysteretic material. The parameters adopted for both stress-strain models are calibrated against experimental data, as discussed in detail in the next section. The fixed-end rotation due to bond slip resulting from strain penetration effects is modelled using a zero-length section element at the end of the beam-column element. The `Bond_SP01` material is assigned to the steel fibres of the zero-length section element for taking into account the cyclic bond slip law proposed by Zhao and Sritharan [50]. For the material parameters definition, the yield slip s_y is determined as follows:

$$s_y(mm) = 2.54 \left(\frac{d_b(mm)}{8437} \frac{f_{ym}(MPa)}{\sqrt{f_{cm}(MPa)}} 2\alpha + 1 \right)^{\frac{1}{\alpha}} + 0.34 \quad (4.9)$$

where f_{cm} is the average compressive strength of concrete, and α is taken as 0.4 in accordance with the CEB-FIB Model Code 90. The ultimate slip s_u is taken as $40s_y$, the initial hardening ratio is assumed equal to 0.4 and the pinching factor is 0.6. A fixed restraint is adopted at the base

node to simulate the foundation. Geometric nonlinearities are considered in the model by means of the PDelta geometric transformation. As a result of discretization, concentrated masses are considered for the eigenvalues analyses. The Newton-Raphson solution algorithm is adopted to solve the model nonlinear equations.

The FE model has first been calibrated against the results of quasi-static cyclic tests. To perform a robust calibration, the results of the quasi-static cyclic tests have been complemented with six additional tests on similar structural elements collected from the literature and presented in Di Ludovico et al. [46]. Hence, the results of eight experimental tests on cantilever RC columns subjected to constant axial load and cyclic quasi-static lateral loads have been employed for model calibration and validation. Geometrical and mechanical properties of the selected columns are summarized in Table 4.21. Square as well as rectangular columns, reinforced either with plain or deformed bars, were considered.

Table 4.21. Geometric and mechanical parameters of the RC columns for model calibration.

Specimen	R300P-c	R500P-c	R500P-c-bis	S300P-c	R300D-c	R500D-c	S300D-c	A	B
b (mm)	500	300	300	300	500	300	300	300	500
h (mm)	300	500	500	300	300	500	500	500	300
f_{cm} (MPa)	18.8	18.8	18.8	18.8	18.8	18.8	18.8	28.8	28.8
f_{ym} (MPa)	330	330	330	330	520	520	520	330	330
Type of bars	P	P	P	P	D	D	D	P	P

All the columns were tested following the cyclic load protocol reported in Di Ludovico et al. [46], and the observed failure mode was in each case controlled by flexure. The Young's Modulus of concrete, expressed by means of the concrete strain at maximum strength (f_c) in the Concrete01 material has been updated in order to achieve a good agreement between numerical and experimental lateral stiffness and, hence, natural frequency. The model calibration is then performed by updating for each test the concrete strain at peak stress, f_c , with a step size of 0.001. Fig. 4.29 shows the comparison between experimental and numerical capacity curves along with the value of ε_c that best fits the experimental data. It is noted that the value of ε_c ranges from 0.003 to 0.008 for the selected quasi-static experimental tests. It is also observed that the numerical curves fit quite

well the hysteretic behaviour of the RC columns in terms of peak strength, lateral stiffness, and pinching effect, well catching the degradation due to damage.

The resulting calibrated models have been then validated against results of output-only modal identification tests in the undamaged and damaged configurations. To this aim, the experimental frequencies of configurations C_0, C_1 and C_2 (reported in Table 4.22) have been compared with those obtained from OpenSees before and after the non-linear static cyclic analysis. Indeed, the OpenSees software updates the stiffness matrix of the model to account for the damage occurred during the cyclic loading and modifies the results of the modal analysis. The comparison of natural frequencies is reported in Table 4.22, along with the value of ε_c associated with the minimum error between experimental and numerical frequencies. It can be noted that for specimen B, a value of ε_c ranging from 0.005 to 0.006 provides the lowest error in terms of natural frequencies for both configurations C_0 and C_2. The same value of $\varepsilon_c = 0.006$ is found to best fit the hysteretic curve from quasi-static test (Fig. 4.29(c)). Similarly, a value of $\varepsilon_c = 0.008$ has been found to provide a good match both with the static and dynamic behaviour of specimen A (Fig. 4.29(d)). The consistency of the obtained results confirms that the FE model is able to predict with a good accuracy the static and dynamic response of column-type elements in both the undamaged and seismically damaged configurations for the considered failure mode.

Table 4.22. Comparisons between experimental and numerical natural frequencies.

Configuration	Specimen	Fundamental frequency			Fundamental Frequency		
		Weak direction			Strong direction		
		Exp	OS	ε_c	Exp	OS	ε_c
C_0	B	31.9 Hz	30.8 Hz	0.005	49.5 Hz	50.1 Hz	0.005
C_1	A	-	-	-	28.8 Hz	28.4 Hz	0.008
C_2	B	17.3 Hz	17.3 Hz	0.006	-	-	-

The procedure discussed in the Chapter 3 has been applied to analyse the population of 200 RC bridge piers and to assess the range of variation of the selected modal-based damage features as a function of the seismic damage level. For the generic pier model, the cyclic lateral loading is

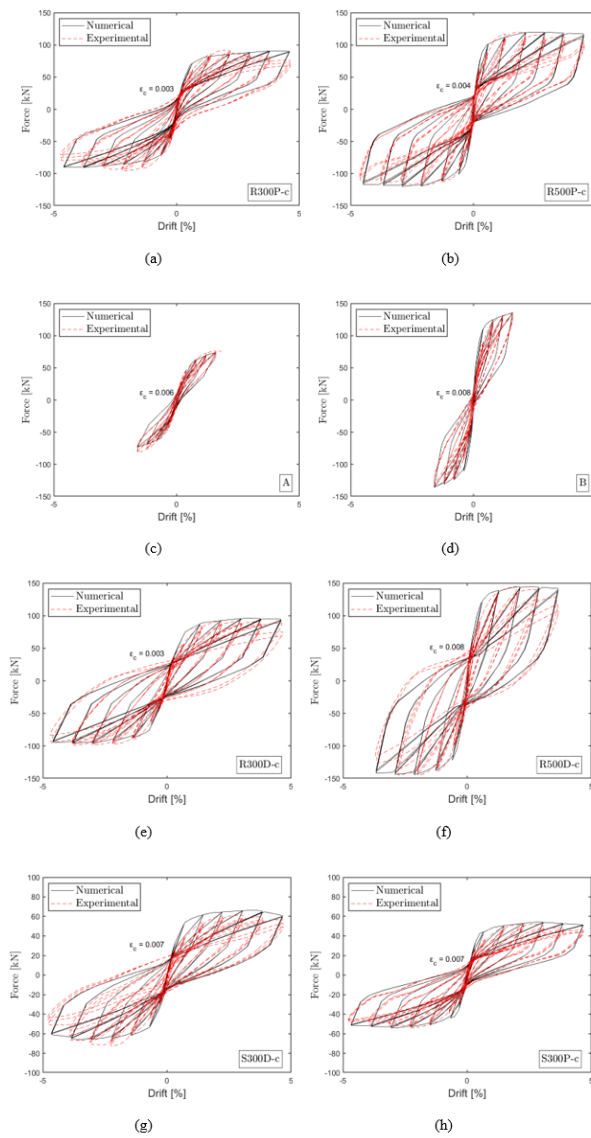


Figure 4.29. Comparison between numerical and experimental capacity curves for the selected eight tests.

applied along the transverse direction y of the bridge (Fig. 4.27(b)).

The load protocol adopted for the numerical simulations is reported in Table 4.23 in terms of imposed DR and number of repetitions for each cycle up to a DR=4.8%, which is assumed to represent a limit value for the complete damage of the pier. This loading protocol is widely adopted for quasi-static testing of structural components and represent all the identified DL. A constant axial load ratio equal to 0.1 is applied in the model during the numerical cyclic loading analyses. For each cyclic loading phase, the damage level is assessed by computing the P&A DI on the hysteretic capacity curve. To assess the DI at each imposed DR, the ultimate rotation capacity of the piers is computed as reported in Perdomo and Monteiro [67]. Then, the variation of the modal-based damage features is assessed and correlated with the damage level experienced by the pier according to the seismic damage scale of Park&Ang reported in the previous section.

Table 4.23. Load protocol for the cyclic pushover.

Loading sequence	IDR [%]	Number of repetitions for each cycle
I	0.80	3
II	1.20	3
III	1.60	3
IV	2.40	3
V	3.20	3
VI	4.80	3

The methodology depicted in Section 3 has been adopted to analyse the dataset of 200 RC bridge piers and to assess the probability distributions of the variation of selected modal-based damage features as a function of the seismic damage level. Given the number of DR investigated, a total of 1200 data are collected from the numerical simulations. Natural frequencies variation in the loading direction are denoted in the following as Δ_{f_1} . The plot in Fig. 4.30 shows the probability distributions of Δ_{f_1} for the set of simulations as a function of the imposed DR. It is clear from numerical results the effect of increasing seismic demand, expressed by means of the displacement demand, on the variation of natural frequency for the piers.

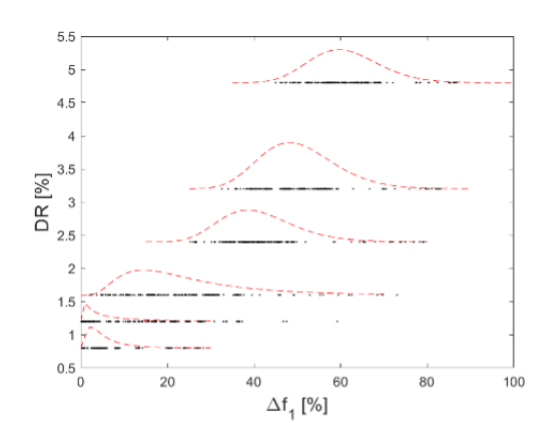


Figure 4.30. Probability distribution of Δf_1 as a function of the DR for the dataset of 200 piers.

Each simulation has been paired with the associated P&A damage level, as depicted in Fig. 4.31(a). With a chosen dataset n.1200 simulations are reached, out of which 200 (18%) reached a DL1, 400 (33%) a DL2, 400 (33%) a DL3 and 200 (18%) a DL4, thus ensuring a sufficient number of data for each damage level. Fig. 4.31(b) shows the number of simulations that reached a certain variation of fundamental frequency, Δf_1 , for each damage level. For DL1, most of the simulations showed a frequency variation lower than 10%, whereas frequency variations ranging between 10-30% are observed for the simulations classified as DL2. For DL3 variation of natural frequency ranges between 30% to 80%, with higher number of data in the range 40-60%. Similarly, for DL4 the frequency variation is between 50% and 100%, with a higher density of results in the range 60-80%.

To finally provide information about the probability of occurrence of a certain damage level given an observed variation of natural frequency in the monitored pier, lognormal cumulative probability functions are derived from the results of numerical simulations, as plotted in Figure 4.32. In the Figure, both the cumulative distributions of numerical data and the fitted lognormal curves are reported for each damage level. The fitting is herein performed adopting the Least Square Estimation method. Mean (μ) and logarithmic standard deviation (β) for the derived curves are reported in

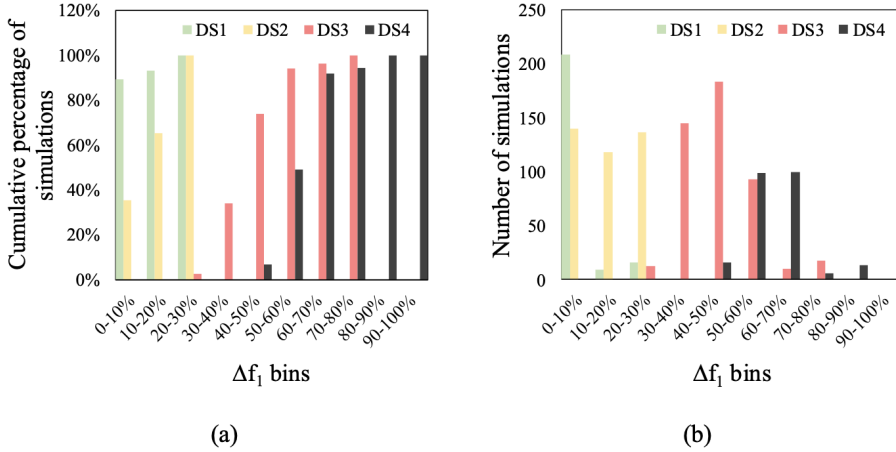


Figure 4.31. a) Cumulative percentage of simulations for each damage level and b) number of simulations that reached a damage level in a certain range of frequency variation.

Table 4.24. The curves allow to assess in a probabilistic framework the correlation of a variation in fundamental frequency due to structural damage in the pier and the probability of occurrence of a certain damage level. For instance, a frequency variation of 40% with respect to the reference condition can be associated with a probability of occurrence of 100% of DL1, 90% of DL2, 28% of DL3 and 0% of DL4. Such kind of information can support decision making processes about serviceability of bridges in the aftermath of an earthquake. Furthermore, additional sources of uncertainties such as environmental effects can be included in the probabilistic model to update the curves based on real observations of the frequency variation over time of the monitored assets in the undamaged reference configuration.

While the previous results confirm the sensitivity of the fundamental natural frequencies to damage, the corresponding mode shapes appear less sensitive to seismic damage. To compute the CoMAC and ECoMAC indices related to numerically-computed mode-shapes at different stages of analysis and, therefore, damage levels, three control points are adopted. For each column, their distance from the base section, normalized with

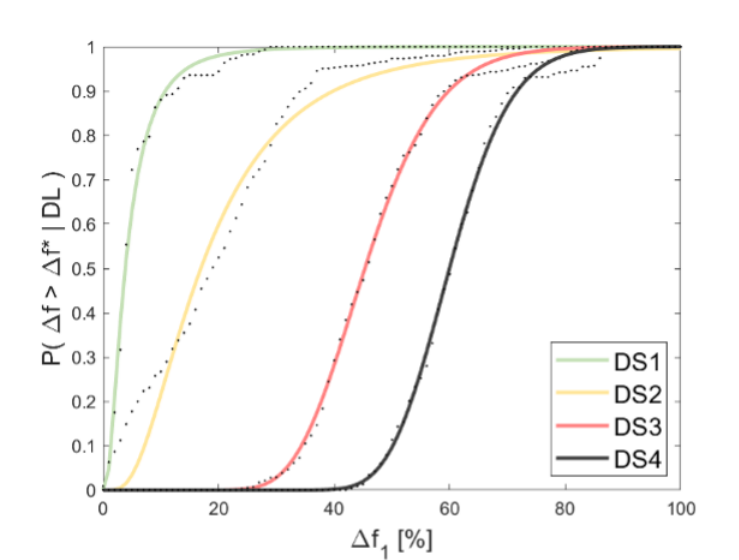


Figure 4.32. Probability of exceedance of each damage level as a function of Δf_1

Table 4.24. Frequency variation probability functions parameters (μ and β) for each damage level.

Damage level	$\mu(\%)$	$\beta(-)$
DL1	4.4	0.80
DL2	16.0	0.67
DL3	49.3	0.22
DL4	60.3	0.14

respect to the pier height H , is 0.3, 0.5 and 0.7. However, it is expected to have more significant variations of both indices near the pier base where the seismic damage is concentrated (i.e., plastic hinge region). The mean, the 16th and the 84th percentiles of the distributions of CoMAC and ECoMAC obtained from numerical simulations for different damage levels are depicted in Fig. 4.33(a) and Fig. 4.33(b), respectively, for the control point at 0.3 from the base of the piers, which is located in the potential plastic hinge region. The figures show that both CoMAC and ECoMAC are slightly sensitive to the simulated seismic damage. Similar results are obtained for the other control points for which the plots of CoMAC and ECoMAC are not herein reported for the sake of brevity. The numerical analyses also confirm that the fundamental mode shapes are not very sensitive to the considered seismic damage scenario, in agreement with the experimental observations reported in Section 4.1.1. Comparing the two damage indices, the ECoMAC appears to be slightly more sensitive than the CoMAC in detecting and localising seismic damage.

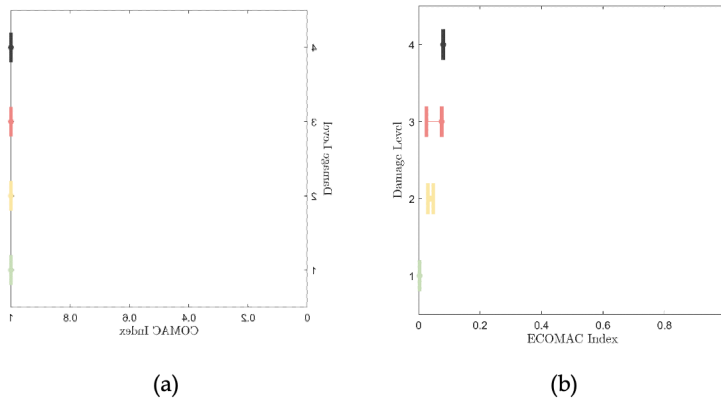


Figure 4.33. CoMAC (a) and ECoMAC (b) for control point at 0.3H from the base of the pier.

A proposal of SHM and data management for bridges

5.1 Introduction

Infrastructures maintenance and inspections programs are more effective the earlier they are able to detect problematic performance. Sporadic and limited inspection procedures need to be supplemented with continuous, remotely accessed real-time, automated monitoring systems. This is possible today with the support of Bridge Health Monitoring (BHM) technologies that aim to continuously monitor the health of the infrastructure, i.e., the level of safety. This work aims to develop effective and reliable means of acquiring, managing, integrating, and interpreting structural performance data to obtain as much information as possible at a minimum cost, reducing human intervention. One issue related to the development of SHM technologies for civil infrastructure is that, except for rare cases, each structure has specific characteristics (material, structural type, geometry, etc.) and it is, therefore, not easy to build a monitoring system that is suitable for all types. The objective therefore of the present study is the definition and development of an appropriately SHM system to overcome these limitations by investigating systems that are adaptable to different categories of bridges. A first distinction can be made based on the material of construction. In what follows, therefore, the study of the monitoring system will be divided into three macro groups of bridges, depending on

the material of construction: reinforced concrete, steel, and masonry. The intent is to assess structural characteristics and the level of damage, keeping in mind that the deterioration process of structures begins at the very moment they are completed and put into operation. Critical issues are intended to be identified and categorized to guide the managing body in inspection and maintenance. Finally, with the data collected, it is possible to create an archive, which is continuously updated, to optimize the use of resources and improve the quality of interventions to be planned. The Service Limit State (SLS) aims to supervise the structural behaviour under different loading conditions. In this regard, to keep an eye on the safety status of the monitored structure, certain thresholds of the monitored parameters can be set, exceeded by which an early warning is sent to the management system. Exceeding a threshold does not necessarily constitute cause for alarm, but it can also be an alert index, following which the necessary inspections are scheduled and decisions are supported. All analyses are intended to identify problems related to damage as cracking, corrosion etc. It started with simple elements that form the infrastructure and is then planned to extend them on a large scale. The most current monitoring systems fit the continuous technological development of data collection and processing instruments. The most interesting measurements to monitor are static or dynamic, but alongside these are usually measured temperature changes that can alter the value of the measured parameters. The designed structural monitoring system involves the use of automatic instrumentation: a system of fixed sensors is installed on the structure that measures the change a physical or mechanical property, which will then be converted into the parameter of interest. It is a system that continuously and automatically records data that can be made immediately available and transmitted to a remote processing unit. Such a monitoring system has different purposes and costs than structural monitoring with removable instrumentation, in which readings are taken by a technician at predefined intervals, taking advantage of tally bases that are specially installed on the structure to be monitored. The two types of monitoring are not always alternative, but can be complementary. In the following sections, a numerical model of a dataset of bridge piers will be shown on which seismic damage was correlated to period changes. Subsequently, the architecture of a monitoring system and its application in different case

studies will be described.

5.2 Architecture of SHM and data management

In order to define the operation of the monitoring system, an architecture of a network was proposed for the management, synthesis, and transmission of the data acquired by the sensors planned for monitoring the infrastructure. The system envisages two compulsory nodes Fig. 5.1, which are responsible for acquiring and processing the data, and one or more optional nodes, which will have access to a web interface for displaying the processed data. Specifically, an on-site machine is foreseen that is able to acquire and process the signals in order to extrapolate synthetic parameters for the evaluation of significant structural parameters for the assessment of the health status of the structure. For this machine, a logical support with a high storage capacity is not foreseen, since the elimination of the raw data is foreseen after the transfer, of the processed data, to the remote machine, or in any case after a certain interval of time useful for checking the data in the event of anomalies, to be established according to the operator's needs; for example, it may be decided to keep all the raw data (time series) in the archive for a week and then eliminate them. The remote server, on the other hand, will have to have a good storage capacity, possibly expandable, as it will act as a real archive of the structure's state of health and all related parameters. In the remote server, therefore, there will be a data visualization interface and an algorithm that will generate a warning should one or more parameters exceed a set threshold.

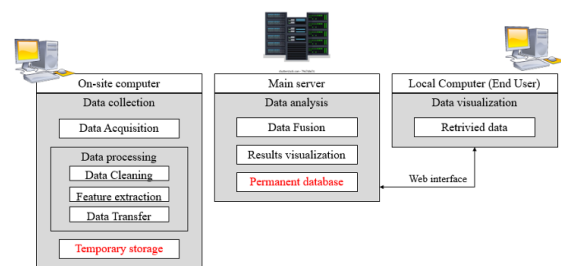


Figure 5.1. Scheme of architecture of the monitoring system

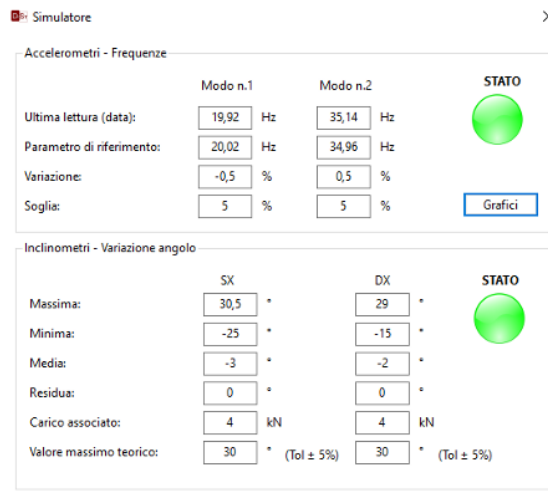


Figure 5.2. Example of management software interface of the main server

Data synthesis means the extrapolation of sensitive parameters whose variation may be a symptom of a change in the structural configuration. If we consider a time interval of 1h with a sampling rate of 200Hz, this time series will consist of 720 thousand samples for each sensor, which translates into a large amount of storage space, especially when the number of sensors is high. This problem will be more pronounced as the longer the time interval for storing unprocessed data. However, from an operational and engineering point of view, it is not essential to store the entire time history but it is certainly useful to extract synthetic parameters representing the health of the structure. One of the fundamental parameters, in dynamic monitoring, for evaluating the condition of the structure is its vibration modes, which represent its dynamic behavior. They are intrinsic values of the structure, they do not depend on external loads and therefore a change in them represents a change in the mass or stiffness of the structure. The modes of vibration consist of a pair of values (eigenvalue and eigenvector), the first representing the vibration frequency and the second its shape. These pairs can be derived from the time history in accelerations by changing the domain, i.e. from the time domain to the frequency domain via the Fourier transform. The peaks in amplitude, displayed in this domain, correspond to the structural frequencies. In this

way, we go from 720 thousand samples to a few numbers (depending on the number of modes read). Modal forms can also be derived by analyzing in the frequency domain, through the Fourier Transform, the time series under acceleration. It is easy to see that the accuracy and number of points available for its reconstruction is a function of the number of sensors installed on the infrastructure. With regard to the rotations read by the inclinometers, it is certainly useful to summarise the time histories of the data recording in terms of maximum, minimum, average and residual value, the latter understood as rotation read when the structure is unloaded. These values are calculated with reference to a specific time interval and it is thus possible to compare the various readings over time. As specified above, in summary, the time histories of the data acquired by the sensors will be stored, temporarily and for an interval fixed by the operator's needs, on the on-site computer and processed at 1h intervals. The processed data will be sent "over the air" (OTA) to a main server, where it will be collected, stored, and interpreted. Their trend over time and any variations will then be evaluated, and any thresholds to be defined will be indicated on the screen. Following a system calibration process under normal infrastructure operating conditions, it will be possible to optimise and calibrate the thresholds. To summarise, two types of thresholds could be defined (Fig. 5.3), the first deriving from simple structural evaluations and/or literature values, while the estimation of the second threshold could take place following a calibration made downstream of the installation of the sensors and after a given period of time, sufficiently long to capture various phenomena of an environmental nature.

The same applies to the dynamic parameters and readings from the accelerometers installed on the structure (Fig. 5.4). In this case, the significant parameters that need to be extracted and stored are the peaks of the spectral matrix and the associated operating deflection shapes (ODS). It is also possible to plot the modal shape, once the frequency is fixed, on the monitoring network management software, through an interface that shows in real time the geometry of the infrastructure and the related modal shapes read from the processing of the accelerometer data. This section describes a methodology for defining variation thresholds of engineering interest for the works under consideration. In summary, synthetic data, such as vibration frequencies, will be extracted from the algorithms in the

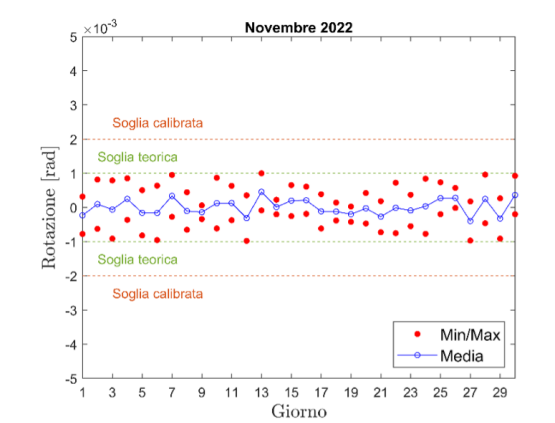


Figure 5.3. Example of time trend of damage characteristics of inclinometer's damage features time trend

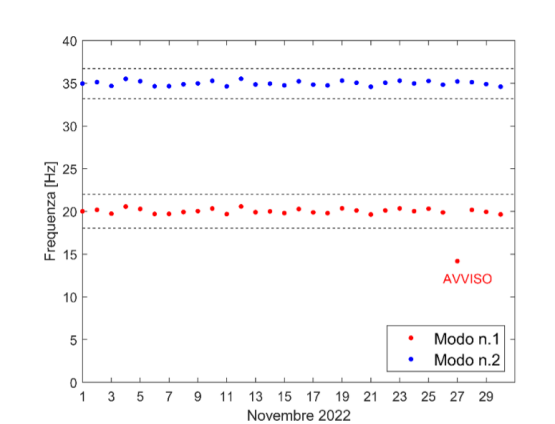


Figure 5.4. Example of time trend of damage characteristics of accelerometer's damage features time trend.

appendix, the variation of which, if slight, may be considered physiological or due to environmental factors such as temperature, or in the case of significant variations a warning will be issued. In particular, thresholds may be set on two different levels, the first being theoretical/literal and the second based on an appropriate training period on data from the sensors installed on the system.

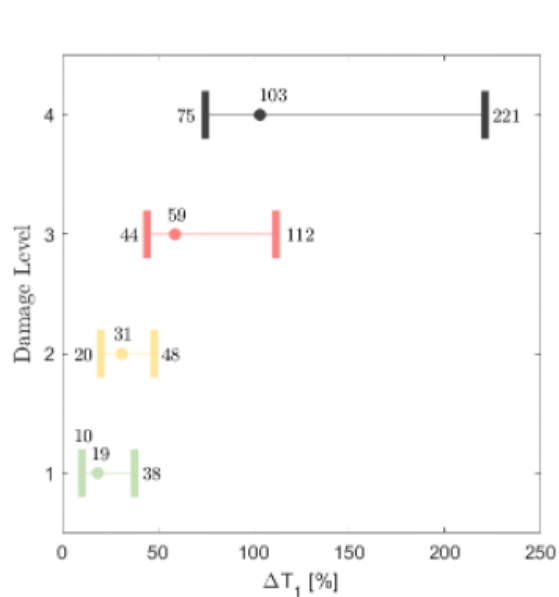


Figure 5.5. Example of threshold estimated for piers bridge.

As far as the first level is concerned, with reference to frequency variation, the following is an example of thresholds defined following laboratory tests on columns. As can be seen from Fig. 5.5, period variations of less than 13% with respect to the elastic period can be associated with minor damage to the structure. Conversely, variations over 40% are correlated with moderate damage. These limits, recalculated and readjusted to the case study, could be taken as a parameter for the evaluation of urgency in the planning of inspections, i.e., once it is realised that an anomaly has been detected in the system, the magnitude of the variation can be used to support the planning of inspections, thus defining the degree of urgency with which to intervene. It is also necessary to take into account the effects

due to temperature. The same applies to the other parameters and quantities measured by all sensors. It should be emphasised that the dynamism and volume of the data require the use of advanced processing methodologies capable of identifying the temporal evolution of the measurements. To this end, one of the objectives is the development of methodologies that automate monitoring and act as a decision support system for users. For each instrument, an estimate was made of the local storage space required for the temporary storage of data to be processed, and of the space occupied by the processed data to be transferred and archived. The estimate is precautionary in that a 24-hour continuous acquisition was assumed for the calculation of the local storage space required for the temporary storage of data to be processed. All data acquired for one week are stored locally, even unprocessed data. Only the processing products are to be transferred via the cloud (Fourier transform for accelerometers and minima, maxima, averages over time intervals and residuals for inclinometers and Linear Variable Displacement Transducers (LVDTs)). The following tables summarise the estimated value of the required space, locally, for the temporary storage of data to be processed, and the size of the processed data to be transferred and stored, for the main instruments.

Table 5.1. Local space required for temporary storage of data to be processed for accelerometers, inclinometers, pH sensors and LVDTs.

Accelerometers ($f_s=200$ Hz)	Inclinometers ($f_s= 5$ Hz)	pH sensors ($f_s= 1$ day)	LVDT ($f_s= 5$ Hz)
4.3 GB/day	200 MB/day	10 kB/day	200 MB/day

Table 5.2. Size of processed data to be transferred and archived, for accelerometers, inclinometers, pH sensors and LVDTs.

Accelerometers	Inclinometers	pH sensors	LVDT
800 kB/day	800 kB/day	10 kB/day	800 kB/day

5.3 Sensors for monitoring system

The constituent elements of the structural monitoring architecture are:

- Sensors, i.e., instruments that detect the change in a physical or mechanical quantity;
- Data acquisition and transmission system: devices that receive signals generated by sensors, convert them and transmit them to computers for processing;
- Data control and processing system: control the operations of the acquisition system and process the data received;
- Data management and archiving system: they store processing results to enable later analysis;
- Structural evaluation system

The sensors and acquisition system are normally installed on the structure, while the other elements are in the manager's office room. The mainly characteristics of the instruments are:

- Range of measures: is the group of values of a single physical entity on the sensors is able to read;
- sensibility: is the lowest value that the instrument can be read;
- resolution: depicted the smallest appreciable variation of the quantity under consideration that over entire measuring range, i.e. the value of the last significant value obtainable;
- linearity: is the property of a measuring to give values that can relate linearly to the input signal;
- accuracy: measure of how closely the results agree with the true or accepted value;
- frequency response: is the description of the instrument output (a function of time) using frequency instead of time as the variable;
- noise: is any disturbance that tends to mask a useful signal.
- transversal sensitivity: defines how sensitive the accelerometer is to accelerations perpendicular to its axis. This parameter is expressed in percentage terms and should ideally be zero per cent.

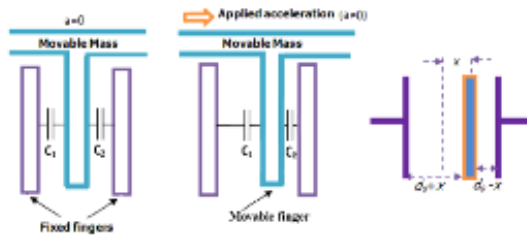
The basis of an efficient monitoring system is an interaction between sensing techniques and mathematical models. The quality of the data provided by sensor measurements determines the quality of the mathematical model used in data processing. The more accurate and precise the sensing instruments are, the more accurate and precise the predictions made through structural monitoring will be. The types of sensors proposed in this document, for railway or motorway viaducts, are shown in the following table. For each instrument, the quantity that can be detected is specified. Crack gauges can be provided in later stages of monitoring.

A brief description of each instrument is given below. An accelerometer is a measuring instrument capable of detecting and/or measuring acceleration by calculating the force detected in relation to the mass of the object. The most commonly used accelerometers can be divided into three categories: Capacitive accelerometers (MEMS): Micro-Electro-Mechanical Systems (MEMS) are a manufacturing technology that can be used in

Table 5.3. Type of instruments and relative measurements

Instruments	Measurements
Accelerometers	Frequencies and modal shapes
Inclinometers	Rotations
LVDTs	Relative displacements
Weather station	Temperature and relative humidity

the production of accelerometers. Generally, when referring to MEMS accelerometers, reference is made to capacitive accelerometers although this technology can also be used for piezoresistive accelerometers. MEMS are cheaper sensors; the operating principle uses the positioning of a weight on springs. One end of the springs is attached to the comb capacitor armature, while the other end is attached to the weight. The force acting on the sensor causes the weight to be shifted onto the springs, so the distance between the capacitive element and the mass varies, and a change in capacitance takes place;

**Figure 5.6.** Capacitive accelerometer scheme

Piezoresistive accelerometers: The operating principle of such accelerometers is similar to the operation of a tensiometer, i.e. the sensor used to measure stress. These types of accelerometers are fitted with a piezoresistive material, which deforms under the flow of an external force, causing a change in resistance. The change in resistance is converted into an electrical signal, which is in turn received by the receiver built into the accelerometer. Piezoresistive accelerometers have a wide measuring band, so they are capable of recording vibrations with high amplitudes and high frequencies. Piezoelectric accelerometers: piezoelectricity is the property

of certain crystals to generate a potential difference when subjected to mechanical deformation; the operation of such an accelerometer is similar to the operating principle of piezoresistive accelerometers. However, under the influence of acceleration, their resistance does not vary, and they generate an electrical voltage of a predetermined value. The sensing element used in these sensors is usually titanium lead-zirconate (PZT). The deformation of the lead-titanium zirconate generates an electrical charge. These accelerometers are characterized by high sensitivity and accuracy. The output signal of piezoelectric accelerometers is usually subjected to amplification and temperature compensation. The operating principle of a generic accelerometer can be theorised as in Fig. 5.7.

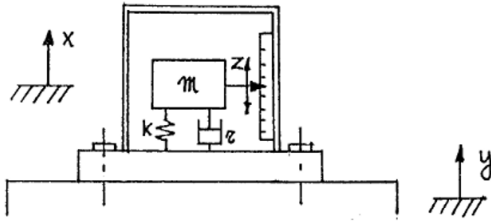


Figure 5.7. Operating principle of an accelerometer

The equation of motion expressed in relative coordinates is of the type:

$$m\ddot{z} + \mu\dot{z} + kz = -m\ddot{y} \quad (5.1)$$

Assuming a harmonic displacement of the constraint $y = Y e^{i\Omega t}$ a harmonic steady-state solution is obtained:

$$z = Z \cos(\Omega t) - \phi \quad (5.2)$$

having displacement amplitude:

$$\frac{Z}{Y} = \frac{m\Omega^2}{\sqrt{(k - m\Omega^2)^2 + (r\Omega)^2}} = \frac{a^2}{\sqrt{(1 - a^2)^2 + (2ah)^2}} \quad (5.3)$$

acceleration amplitude:

$$\frac{Z}{\Omega^2 Y} = \frac{1}{\omega_0^2 \sqrt{(1-a^2)^2 + (2ah)^2}} \quad (5.4)$$

phase angle:

$$\phi = \arctan\left(\frac{r\Omega}{k - m\Omega^2}\right) = \arctan\left(\frac{2ah}{1-a^2}\right) \quad (5.5)$$

being: $a = \Omega/\omega_0$ the dimensionless frequency parameter; $\omega_0 = \sqrt{\frac{k}{m}}$ the instrument's own pulsation; $h = \frac{r}{2m\omega_0}$ the dimensionless damping parametrs. The main features of an accelerometer are listed below.

- **Sensitivity:** The sensitivity of an accelerometer defines how quickly the sensor converts mechanical energy into an electrical signal (output) and this defines the measurement range of the accelerometer. Sensitivity is generally expressed in mV/g (millivolts per g) or pC/g (picocoulombs per g), where g is the acceleration of gravity. The choice of sensitivity depends on the type of signal you wish to measure. If you are interested in small vibrations, then a high sensitivity is required to get a clean signal. When, on the other hand, one wants to measure accelerations due to impulsive events then it is preferable to use accelerometers with low sensitivity (less than 1mV/g). For dynamic monitoring applications, a high sensitivity is recommended, which varies depending on the type of structure, but in any case not less than 500mV/g. **Mass:** must not exceed 1/10 of the mass of the vibrating part on which the accelerometer is mounted, so as not to change the dynamic properties of the body being measured. This problem is little felt in the application field of dynamic monitoring of structures.
 - **Bandwidth:** The output signal remains constant as the frequency changes from 0 Hz, for DC-response type systems (MEMS), and 1-2 Hz for AC-response type systems (piezoelectric), up to a limit imposed by the resonance of the accelerometer, at which point the signal increases. As a rule, an accelerometer is usable up to one-third of its resonance frequency, taking into account any reduction in frequency due to mounting. This problem is overcome by choosing an accelerometer with a sufficiently wide bandwidth.
-

- Noise: the noise level can be defined in different ways; some data sheets report noise as RMS, usually expressed in $\mu V/\sqrt{Hz}$ or $\mu g/\sqrt{Hz}$, calculated from the mean square value of the signal obtained in the absence of mechanical excitation. Accelerations smaller than noise will not be detectable. Some manufacturers provide a spectral parameter of the noise expressed in $\mu V/\sqrt{Hz}$ or $\mu g/\sqrt{Hz}$, this is because noise tends to decrease as frequency increases.
- Transverse sensitivity: it defines how sensitive the accelerometer is to accelerations orthogonal to its axis. This parameter is expressed in percentage terms and should ideally be zero per cent.

The definition of the acquisition frequency represents one of the most important parameters in the definition of a dynamic monitoring system. The Nyquist-Shannon theorem states that the acquisition frequency must be at least double the maximum frequency to be sampled. Assuming, for example, that the maximum expected value of the frequency of interest is 20Hz, an acquisition frequency greater than 40Hz must be adopted. Inadequate selection of the sampled frequency results not only in the failure to identify frequencies greater than half of it, but also in incorrect reconstruction of the signal after its digitisation and some high frequencies will appear as low frequencies. This problem is recognised as aliasing, in fact, aliasing is the phenomenon that originates from the discretisation of a continuous signal when it is incorrectly sampled, in particular undersampled. From a FEM model described in the next chapter, it was estimated that the maximum frequency of interest, for case studies, is in the region of 60 Hz, so a frequency higher than 120 Hz is required. For practical purposes, it would be better to be far from the Nyquist frequency, so it was decided to increase the acquisition frequency to 200 Hz. Inclinometers are instruments that measure inclination. There are different types of inclinometers on the market. Bar inclinometers, or inclinometers, are metal bars on which a highly sensitive inclinometer sensor is mounted. They are firmly anchored to the surfaces to be controlled by means of special brackets. They can vary in length, generally from 1 to 3 meters, and are installed individually, to monitor the relative inclination between two points, or in series, so that the end of one bar coincides with the beginning of the next, until the required distance is covered. In the latter case, each individual

bar rotates differently following the differential movements of the structure; this allows a profile of the differential failures to be reconstructed. Bar inclinometers have low costs, good sensitivity, reliability over time and robustness.



Figure 5.8. Example of electroplating bars

There are also the micro-electro-mechanical-system MEMS (Micro-Electro-Mechanical-System) single, biaxial or triaxial inclinometer sensors. The sensor provides an output voltage proportional to the inclination of the instrument, which is read out and converted into a measurement of inclination in the form of mm/m; an integrated thermometer also allows the thermal effect on the structure and sensor to be assessed to distinguish seasonal variations from actual rotations, with automatic correction for thermal effects. Electrolyte-type sensors are characterized by excellent thermal stability, while MEMS-type sensors guarantee excellent linearity and thermal stability. The full scale, typically $\pm 2^\circ$ or $\pm 5^\circ$, allows for resolution and stability suitable for normal conditions of use. Measurements can be taken by means of a manual portable control unit or by means of a datalogger, with automated management. Manufacturers generally have specific software that allows real-time management of measurements.

The prediction of the rate of deterioration of the concrete's protective capacity, represented by the concrete cover, is all the more advantageous, effective and decisive the earlier it is performed. The method based on the use of electrodes aims to non-destructively measure the chloride content



Figure 5.9. Example of MEMS inclinometer

and pH of the concrete in order to assess the deterioration conditions and to monitor the ageing and deterioration process over time. This technique provides information on the dynamics of chloride diffusion and pH variation with depth. In particular, the method is based on the measurement of the potential of an electrode with a millimetre diameter inserted inside the concrete in the casting or post-casting phase, referred to a counter electrode of the liquid junction type placed on the external surface of the same. The method for measuring the concentration of chloride ions and pH in concrete is based on the measurement of the electrode potential of a measuring electrode inserted inside the concrete, with respect to a reference electrode placed on the external surface of the concrete. In the case of chlorides, the measuring electrode consists of a silver wire covered with an AgCl film obtained by electrochemical anodising. In the case of pH, the measuring electrode consists of an iridium wire coated with an iridium oxide film obtained by thermal oxidation. In both cases, the reference electrode is of the liquid junction type, consisting of a copper rod immersed in a saturated copper sulphate solution. Potential measurements are translated into concentration values by means of sensor-specific calibration curves derived from laboratory measurements of reference standards. The corrosion detection and monitoring system is intended to be additional and complementary to the laboratory analytical procedures. pH electrodes can either be installed during casting (pre-casting), anchoring them to the reinforcement (in which case the sensors are immersed in the concrete) or, in existing structures, they can be inserted with a minimally invasive intervention into small holes drilled in the concrete, subsequently covered with gypsum paste and suitably sealed on the outside. Data can be acquired

by data loggers with an adjustable time frequency. The measurements are transmitted, in real-time, to the central portal, which records the information and manages alarms. Transmission admits all types of protocols and takes place via GSM or WIFI modem, or directly via a USB serial port. Ultrasonic thickness measurement is a widely used non-destructive testing technique to measure the thickness of metallic elements even when access is only provided from one side. Such gauges, which were developed with the same operating principles as sonar, have become common for structural monitoring applications since 1970.



Figure 5.10. Examples of commercial ultrasonic thickness gauges

Such gauges are excellently suited to monitoring the thickness of materials with a high Young's Modulus, as the transmission of pulses at high-/very high frequencies is optimal in these materials. Continuous thickness measurement for metal members is therefore a remarkable and proven application, especially when monitoring such structures in aggressive environments. Sound energy can be generated over a wide frequency spectrum. Ultrasonic thickness gauges work by measuring the transmission time of a sound pulse generated by a small transducer, which is reflected within the element under investigation (flange, core) in the direction of thickness. The measurement is normally carried out from one side only in 'impulse/echo' mode, as the presence of the steel/air interface alone is capable of inducing the reflection of the waves carry out the required measurements. This mode is extremely advantageous in the case of metal members with surfaces that are difficult to access, such as box sections, tubulars, tiled elements or even laminated profiles located immediately below the deck. The thickness measurement is carried out using the well-known principles of compression wave transmission in elastic materials. The transducer detects the reflection time (forward + return) in the element considered, which is related to the thickness s of the element via a simple kinematic relationship:

$$s = \frac{v_{el} t_{rif}}{2} \quad (5.6)$$

where s is the thickness of the monitored element, v_{el} is the propagation speed of elastic waves in the material considered, t_{rif} is the reflection time (forward+return) measured by the transducer. From the theory of elastic waves, the correlation between the speed of propagation and the physical and mechanical properties of the material is well known. With reference to steel we have, in particular:

$$v_{el} = \sqrt{\frac{E_s}{\rho_s}} \quad (5.7)$$

where E_s is the Young's steel modulus and ρ_s is the density of the steel. It follows that for the monitoring of metallic materials, the reference propagation speed is essentially constant and of the order of 5172 m/s. It is evident that the speed of sound in the test material is an essential part of the measurement process, so any changes in the speed of sound due to environmental effects must be duly taken into account (e.g. due to daily and/or seasonal variations in temperature). Therefore, the careful calibration of ultrasonic measuring devices is an essential preliminary step, as the accuracy of the measurements cannot exceed the accuracy of the calibration. In order to optimise wave transmission, liquid interfaces are usually applied between the gauge and the element to be monitored ('couplant'). Common couplants are glycerine, propylene glycol, water, oil and gels, of which minute quantities are sufficient to bridge the air gap that would otherwise (albeit extremely thin) occur between the gauge and the member. Continuous thickness measurements ultimately allow both daily thickness excursions due to thermal expansion and actual thickness reductions due to material degradation to be monitored, which can be appropriately manipulated to derive daily/monthly/annual corrosion rates. The reference specifications of these sensors are summarised below:

- Measuring technologies: direct measurement (single element, not suitable for corrosion measurement); delay line (with separating element between transducer and membranes, useful for measurement of very thin thicknesses); immersion (water/oil, as transmission fluid,

useful for moving products); dual element (with two transducers at a reduced distance, very suitable for corrosion);

- Measuring range (dual-element meters): $\simeq 0.1$ mm to 40 mm;
- Instrument sensitivity (dual-element meters): ± 0.002 mm;
- Measuring frequency (dual-element meters): 5 Hz;
- Other specifications: in the case of protected elements (e.g. galvanising, although not currently permitted by RFI (Rete Ferroviaria Italiana) in the case of railway bridges), the different wave propagation velocities in the elastic media in series must be taken into account; the transducers should be carefully protected if the temperatures of the surfaces to be monitored exceed 50°C .

LVDTs (Linear Variable Displacement Transducers) are electromechanical devices (Fig. 5.11) used to convert rectilinear motion into a variable electric current, voltage or electrical signals, and vice versa. They are used as mechanical motion sensors in measurement technology. The classification of electromechanical transducers includes conversion principles or types of output signals.



Figure 5.11. Linear Variable Differential Transducers

Physically, the LVDT construction is a hollow metal cylinder in which a shaft of smaller diameter can swing inside the housing along the cylinder's longitudinal axis. The shaft, or push rod, terminates in a magnetically conductive core that must be inside the cylinder, or coil assembly, when the device is in operation, as depicted in Fig. 5.12

The push rod is attached to the point whose measurement is to be known, while the coil assembly is attached to a reference point which, if

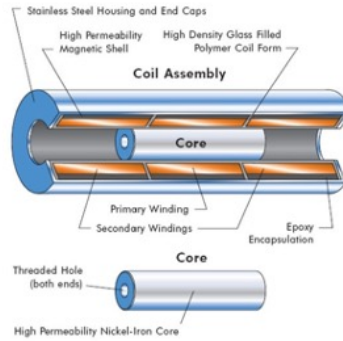


Figure 5.12. Internal structure of LVDT devices

possible, must be fixed or at least triangulated with other points to allow the reading or derivation of an absolute quantity. Therefore, in the structural field, LVDTs can be used to know displacement measurements. The basic variable in selecting an LVDT is the maximum displacement of the core from its 'zero' position that produces an output with the specified linearity. The distance the core can travel is called the full scale displacement. Since the core can be moved from the 'zero' position by either side of the LVDT transducer, the linear operating range is twice the full scale displacement. This is indicated in \pm full scale displacement and called the nominal linear range. This figure is a fundamental specification for an LVDT. The linear range of any LVDT changes by a few degrees with frequency. The nominal linear field is a value related to the frequency at which the transformer is powered. When the LVDT is used with the correct core for the specific frequency, the actual linear field will always be equal to or greater than the nominal value. Where improved linearity is not an essential parameter, the operating range can and will be increased far beyond the nominal linear range. Conversely, an improvement in linearity can be achieved by using the LVDT for less than its nominal linear range, or only to one side with respect to the 'zero' position. Another factor influencing the operating range of an LVDT is the load resistance. The nominal linear range is specified for a high load resistance, typically 50kOhm to 0.5MOhm. If a low load resistance is required, the effects of this on the linear range must be considered. Sensitivity can be spec-

ified in terms of output per nominal full scale. Sensitivity is generally expressed in mV output per 0.001 inch of displacement per volt of excitation (mV/mm/Volt), although it is occasionally specified in volts output per inch per volt of input. The ideal output of an LVDT with an infinite load resistance for a given core position is the product of sensitivity, core displacement and excitation voltage. The actual output voltage depends on the load resistance and the excitation frequency. If a high load resistance is used, the difference between the ideal and actual output voltage is insignificant. If a low load resistance is used, its effects must be taken into consideration. Sensitivity also varies with the excitation frequency; therefore, this must be known when considering sensitivity. Sensitivity used to be an important specification for an LVDT in the past, however, nowadays, with the availability of high-gain amplifiers, digital players and other modern electronic media, the importance of sensitivity has diminished for LVDT users. The output voltage of an LVDT is a linear function of the core displacement within a specific range of motion. Within the nominal range, the maximum output deviation of an LVDT from the best straight line applied in an output diagram as a function of core displacement is defined as the linearity of the LVDT. Linearity is usually expressed as a percentage of the full-scale output, but occasionally as a percentage of the reading. Linearity is normally specified for a high load resistance. The typical linearity of an LVDT is 0.25% of full scale, but improvements can be achieved by special construction techniques. Linearity up to 0.05% can therefore be achieved in this manner. Of course, linearity can also be improved by using a measuring range below the full-scale range or by using half the nominal operating range. The smallest change in core position that can be observed at the output of an LVDT is called resolution. Since an LVDT operates on the principle of magnetic coupling, the resolution is essentially infinite. This means that an infinitesimal change in core position will result in a change at the output. Having determined the important terms for an LVDT, it is now possible to examine the operating characteristics in detail. An LVDT can be designed to operate at frequencies from 50 Hz up to radio frequency (1 Mhz and above). However, the usual transformers for laboratory, military and industrial applications are supplied to operate in the 50 to 25 kHz range. The fidelity of response to vibrations or rapid mechanical movements requires the use of a frequency

at least 10 times higher than the frequency of movement of the mechanical element. When an LVDT is used for static or very slow measurements with no oscillations above 6 Hz, a frequency of 60 Hz is convenient. A higher excitation frequency can be used to achieve better results even though the same operation could be performed with a lower frequency. In any case, the LVDT must be suitable for a particular frequency. Sensitivity and efficiency generally increase with the excitation frequency, especially in the low-frequency part of the previously specified range. Common LVDTs are developed for nominal supply voltages of 1 to 10 V, although other voltages may be used in certain applications. The mechanical operating life of the LVDT is practically infinite, as explained above. Nevertheless, the possibility of electrical failure exists. There are two possibilities of failure; shorted or open winding. Factory tests make the possibility of a short circuit very low. Local weather stations (Fig. 5.13) allow the continuous measurement of basic environmental parameters such as temperature, relative humidity, atmospheric pressure and wind speed and direction.



Figure 5.13. Example of H-level sensors layout for monitoring subsidence in a building.

These measuring stations are of particular interest for continuous structural monitoring applications, as they minimise the uncertainty on the aforementioned parameters that would result from assuming the measurements provided by 'centralised' meteorological stations as local values. The latter, in fact, are frequently located at considerable distances from the structures being monitored, and therefore the measurements are polluted by interpolation operations between the measurement site and the site of construction. The most modern local weather stations have a modular

structure consisting of digital sensors with no moving parts, and are therefore also inherently protected from recurring wear and tear that would occur, for example, as a result of wind speed measurements. It should be recalled that the accurate measurement of the latter parameter, in association with the direction of air currents, is of fundamental importance for dynamic monitoring, as it serves as an important source of 'ambient noise', which in turn is the main input for the operational dynamic analyses to be carried out for in-situ modal identification. Similarly, accurate measurements of temperature and relative humidity make it possible to eliminate uncertainties related to phenomena such as material degradation (e.g. carbonation of reinforced concrete or corrosion of steel) or any periodic measurement fluctuations due to seasonal effects. The high level of integration of the electronic circuits for the latest generation of local stations makes it possible to have a small body within which all operational functions are collected; this facilitates precisely the activity of meteorological monitoring outdoors. H-Levels are systems for accurate, long-term monitoring of differential subsidence of structures. The versatility of configuration allows them to be adapted to different cases of interest: buildings, tunnels, geotechnical works and other civil structures. The system consists of a series of H-Level sensors hydraulically connected to a reference tank, installed in a position deemed stable. Each H-Level includes a high-resolution pressure sensor that monitors the liquid level resulting from the height difference (hydraulic head) between the sensor and the reference tank (Fig. 5.14).

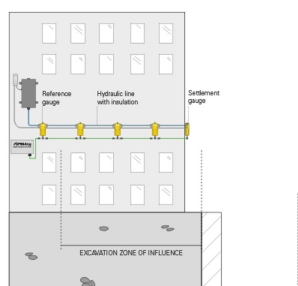


Figure 5.14. Picture of a typical weather station

Such systems have the enormous advantage of being able to directly

monitor absolute displacement measurements. This is key in the monitoring of structures where other possible systems would involve the use of ground anchoring systems, which are often very costly and difficult to implement due to the typical conditions of bridges (river crossings and/or high gradients). Digital crack gauges are instruments used for measuring and recording relative movements between parts of the same structural element or between different elements, on vertical and/or horizontal surfaces. Crack gauges consist of two plates attached to the edges of a crack, which partially overlap and allow the relative displacement in the vertical and horizontal directions of two opposing surfaces to be measured. The lower plate is graduated in the horizontal and vertical directions, with the zero positioned at the intersection of the median lines. The measurement of lesion movement is indicated in mm or fractions thereof and is marked by the amount of displacement of the reticule plate with respect to the underlying millimeter plate, starting from the zero value. The crack gauge is positioned across the crack, with the grid zeros coinciding.

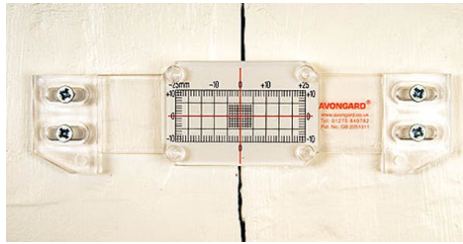


Figure 5.15. Example of an analogue crackmeter.

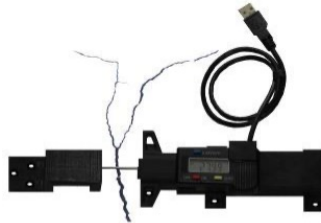


Figure 5.16. Example of a digital crackmeter.

Deformation sensors are widely used in many measurement applica-

tions, from static to dynamic. Through appropriate correlations, they can be used for measurements of deflection, vibration, load, torque, pressure, tension and strain.

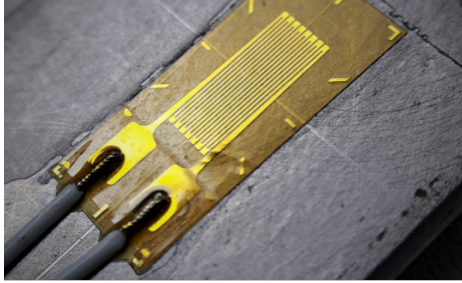


Figure 5.17. Example of a commercially available strain gauge.

Of particular importance among them are strain gauges or resistance strain gauges. Such sensors measure strain by means of a change in electrical resistance. In a single-sensor strain gauge (Fig. 5.17), a metal foil pattern is mounted on a flexible substrate, which also serves to isolate the metal from the test object. A current is passed through the foil pattern. When the test object is stressed on the axis parallel to the foil pattern, a change in resistance proportional to the amount of deflection occurs. It is therefore possible, via a suitable calibration curve, to measure the deflection from the resistance measurement:

$$\varepsilon_{str} = \frac{\Delta L}{L_0} = k_{sg} \Delta R_{sg} \quad (5.8)$$

where ε_{str} is the deformation undergone by the monitored structural element in the strain gauge direction, i.e. the ratio of the measured fibre elongation L to its initial length L_0 , k_{sg} is an instrumental parameter characteristic of strain gauge which correlates the measured resistance difference ΔR_{sg} to the deformation of the monitored fibre. This parameter can be variable as R_{sg} changes and is therefore provided through the aforementioned calibration curve. Temperature plays a key role in resistance (and consequently strain) measurements made by strain gauges. In particular, it is observed that for the conductors constituting the strain gauges, resistance increases with temperature. It is therefore necessary to compen-

sate for this effect by arranging two strain gauges mutually orthogonal, so that one of them measures the total deformation (parallel to the axis of the member, mechanical + thermal def.) while the other is only able to detect the thermal deformation (orthogonal to the axis of the member, thermal def.).

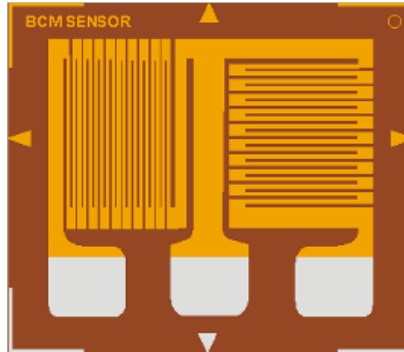


Figure 5.18. Coupled configuration of strain gauges in order to purify errors due to temperature variations.

Another source of temperature increase is the self-heating of the resistance gauge (Whitestone Bridge) as a result of the Joule effect. It should in any case be pointed out that, as far as this latter phenomenon is concerned, the calibration curves are already calibrated for appropriate compensation (via a specific parameter called Gauge Factor GF). The measurements of deformation (and consequently of tension) through deformometers can provide a very useful integration to dynamic structural monitoring following the diagnosis of structural damage in progress. Following the partial or total failure of one or more structural elements, in fact, there are phenomena of internal redistribution of stresses that can also be considerable in the case of strongly hyperstatic structures (e.g. in continuous girder bridges). At the same time, such gauges are crucial for identifying otherwise unforeseen stress regimes resulting from effects not quantified in the design (e.g. torsional effects due to the meandering of mobile loads or transverse actions from wind/earthquakes).

5.4 Accelerometers layout optimization

A modal analysis was performed on a FEM model to determine the number of accelerometers required to measure certain points of the modal shapes for a simple-supported grid. Figure 5.19 shows the points of the modal shape that can be captured using three accelerometers, while Figure 5.20 shows the points that can be captured using five accelerometers. Finally, Figure 5.21 illustrates the points of the modal shape that can be captured using seven accelerometers.

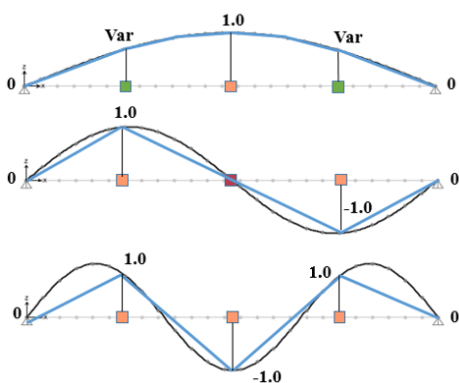


Figure 5.19. Accuracy on prediction of modal shapes with n.3 sensors.

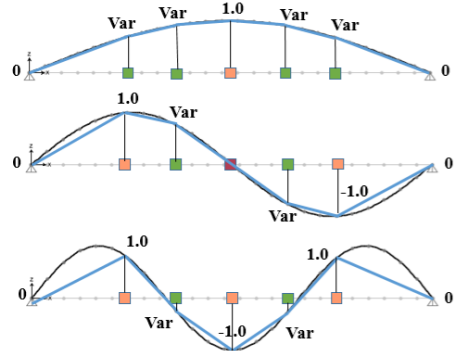


Figure 5.20. Accuracy on prediction of modal shapes with n.5 sensors.

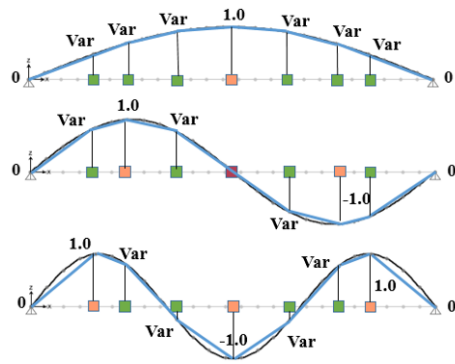


Figure 5.21. Accuracy on prediction of modal shapes with n.7 sensors.

Considering the identification of the modal forms of three vibration modes of the simple-supported beam as a target, at least seven accelerometers equally spaced across the span are required to have a discrete accuracy of the shape. To minimize the number of sensors needed, it may be worthwhile to take into account the structural symmetry and monitor only one side of the span. However, it is important to validate this approach using experimental data to ensure its effectiveness.

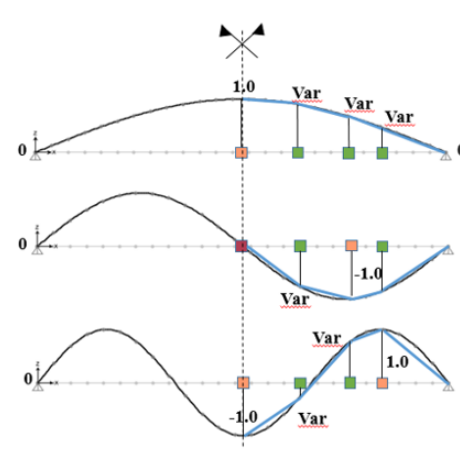


Figure 5.22. Positioning and number of accelerometers taking into account the symmetry of the span.

Chapter 6

Bridge Health Monitoring: case studies

In this section an experimental study that aims to validate the methodology proposed in the previous chapter on a scaled steel bridge is reported along with an application to some case studies of existing railroad bridges and viaducts in Italy. According to the monitoring simulation showed in the previous chapter and a simplified modelling, a monitoring system and instruments layout for the following bridges are defined:

- Brin Viaduct (EAV)
- Volturno Viaduct (EAV)
- Viaduct n.1011 (TaNA)
- San Gennaro Viaduct (TaNA)
- Sant'Eframo Viaduct (TaNA)
- Viaduct n.0080 (TaNA)
- Viaduct n. 1028 (TaNA)
- Viaduct n.1080 (TaNA)
- Viaduct n.1026 (TaNA)

There are two bridges managed by “Ente Autonomo Volturmo” (EAV) and seven managed by “Tangenziale di Napoli” (TaNA). A description of each viaduct and its instrumentation layout will be given in the following sections.

6.1 Laboratory test for validation

The methods suggested in the previous chapter has been tested in the lab using a scaled steel bridge. There are two piles supporting the 4.7 meter long span of the bridge. A dynamic identification of the structure was carried out using two different layouts with the same number of sensors to evaluate the structural symmetry in order to validate the methodology proposed in the previous chapter. Fig. 6.1 and Fig. 6.2 show a lateral view and a front view of the specimen bridge, respectively.



Figure 6.1. Lateral view of the specimen bridge

The dynamic identification test was carried out from ambient noise. Were used n.8 accelerometers mems arranged according to two different layouts as shown in Fig. 6.3. The technique used to derive frequencies and modal shapes is the Frequency Domain Decomposition. Downstream of the identification, a simulation and test of the functioning of the system was carried out, according to the methodology described in the previous chapter. In particular, it has been simulated that the sensors are installed

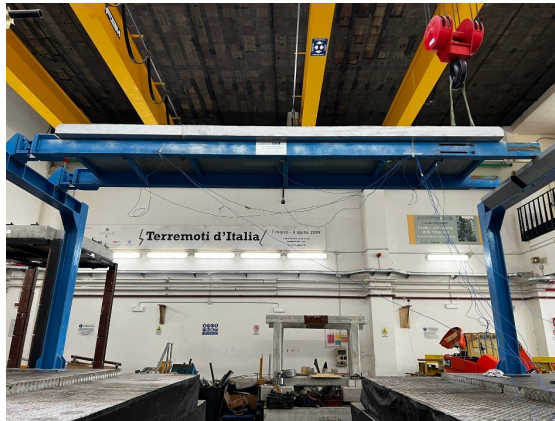


Figure 6.2. Front view of the specimen bridge

on an existing structure where there is an on-site acquisition unit that transmits data to a remote server, processing and extracting the significant parameters before data transfer. As shown in Table 6.1, the results of Operational Modal Analysis include a flexural mode with a frequency equal to 12.60 Hz, a modal complexity factor (MCF) of 0.36%, a damping ratio of 0.597%, and a torsional mode with a frequency equal to 15.45 Hz, a modal complexity factor of 1.32%, a damping ratio of 1.58%.

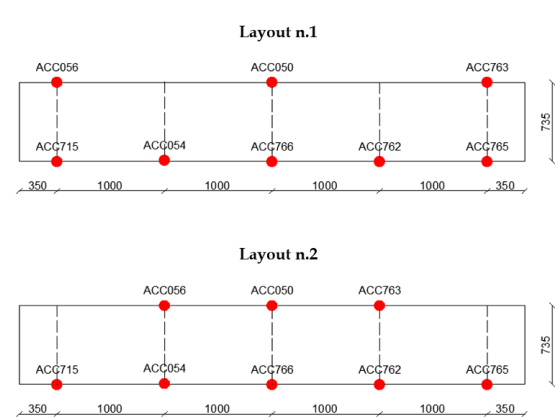


Figure 6.3. Layouts of accelerometers for the OMA test of the specimen

noted that for the objective of monitoring global behaviour, the number of sensors could be reduced, after the training period, by taking into account the symmetry of the span (this arrangement is proposed to have useful indications for the best calibration of the monitoring system).

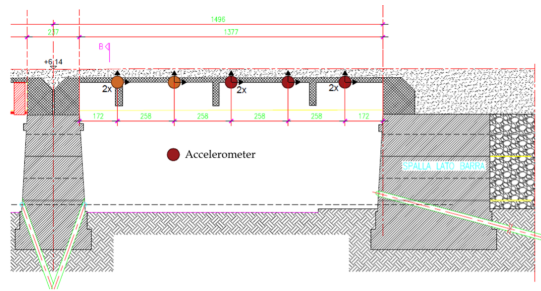


Figure 6.6. Layout of accelerometers for the BRIN bridge

* Double the number of sensors (2x) means installing a sensor on the opposite side of the cross-section to assess torsional effects.

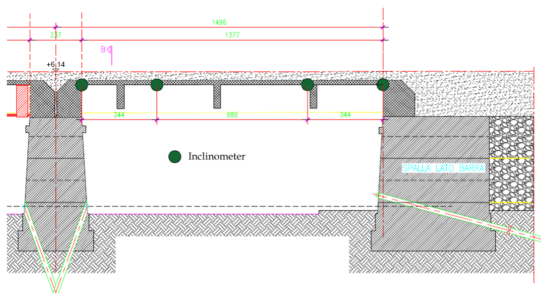


Figure 6.7. Layout of inclinometers for the BRIN bridge

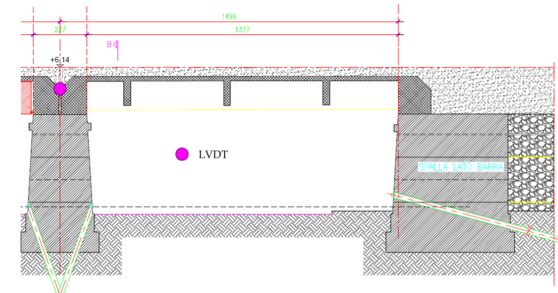


Figure 6.8. Layout of LVDTs for the BRIN bridge

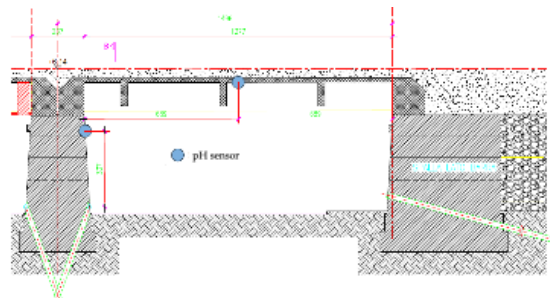


Figure 6.9. Layout of pH sensor for the BRIN bridge

6.3 Volturno bridge

The Volturno railway bridge is located at km 7+368 on the S.M. Capua Vetere-Piedimonte Matese line, crosses the Volturno River and is located in the municipality of Triflisco, province of “Caserta”. The bridge, with a metal structure, consists of three spans of respectively:

$$L_1 = 22.05 \text{ m}$$

$$L_2 = 44.10 \text{ m}$$

$$L_3 = 22.05 \text{ m}$$

The structure of each span consists of two main parallel-current truss beams connected by vertical uprights and diagonal inverted V-beams. The height of the main truss beam is 4.00m. The structure has upper and lower bracing in addition to vertical cross X bracing. In terms of restraint conditions, the side spans are found to have a pair of supports at the abutments, and a pair of pendulums at the piers. The central span, on the other hand, has a pair of supports at the pier on the Santa Maria Capua Vetere side, and a pair of pendulums on the Triflisco side abutment. The operating loads bear on the structure through the action of the rails on the longitudinal stringers. The upper floor between the rails and the side pedestrian walkways is made of striated sheet metal. The abutments are made of reinforced concrete. The structure of the abutment named S1 (S. Maria C. V. side) placed in the riverbed consists of a massive plinth of dimensions $L \times B \times H = 8.5 \times 5.5 \times 1 \text{ m}$, founded on 24 beaten piles of length 20 m and diameter 50 cm placed at 1.5 m spacing. On the plinth rises the slightly tapered reinforced concrete abutment of dimensions $B \times H = 5.6 \times 9.5 \text{ m}$. Hinge-type supports are placed on the top. The abutment structure named S2 (Triflisco side) consists of a massive plinth with dimensions $L \times B \times H = 16.8 \times 6.4 \times 1.7 \text{ m}$, found directly on the ground. On the plinth rises the slightly tapered reinforced concrete abutment of dimensions $B \times H = 2.4 \times 12.25 \text{ m}$ and is stiffened by two wing ribs of dimensions $B \times H = 3.2 \times 10.1$. Hinge-type supports are placed on the top. The structure of the pile named P1 (S. Maria C. V. side) placed in the riverbed consists of a massive plinth, with an elongated rectangular-shaped base with dimensions $B \times L \times H = 4.0 \times 13.0 \times 1.0 \text{ m}$ and connected ends for water runoff, founded on 23 beaten piles, on which the pile with a rectangular section connected on the tapered minor sides and placed to support the reinforced concrete

pulvinus is elevated. Both hinge-type (Triflisco side) and bipendole-type (S.M. Capuavetere side) supports are placed on the top. The structure of the pile named P3 (Triflisco side) consists of a massive plinth, with an elongated rectangular-shaped base with dimensions $B \times L \times H = 4.0 \times 13.0 \times 1.0$ m and connected ends; from the documents collected in the archives, the base appears to be founded on 23 beaten piles, on which the pile rises with a rectangular section connected on the smaller sides, tapered and placed to support the reinforced concrete pulvinus. On the top are placed the supports of the bi-fold type.

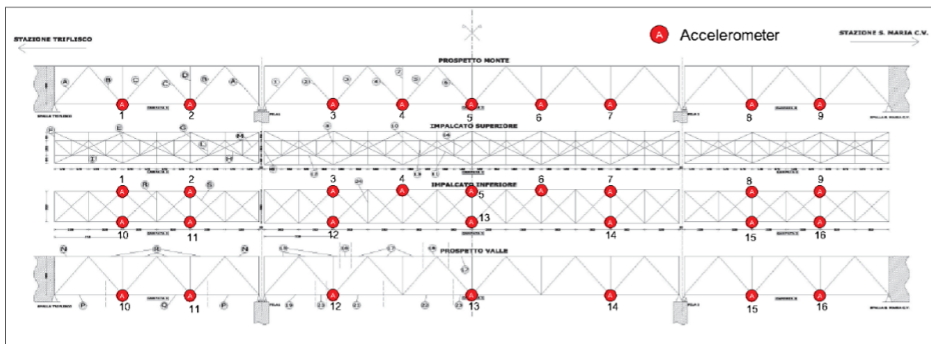


Figure 6.10. Accelerometers layout on the Volturmo bridge

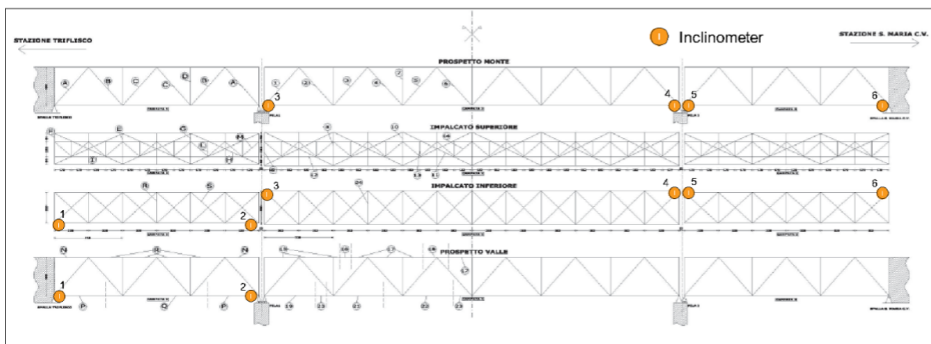


Figure 6.11. Inclinerometers layout on the Volturmo bridge

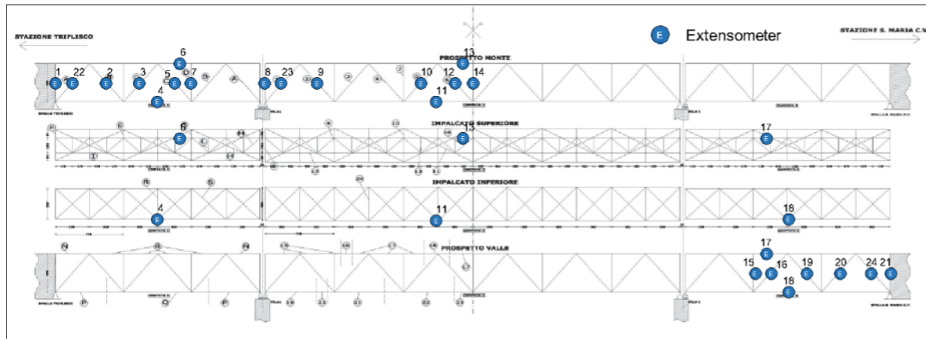


Figure 6.12. Extensometers layout on the Volturno bridge

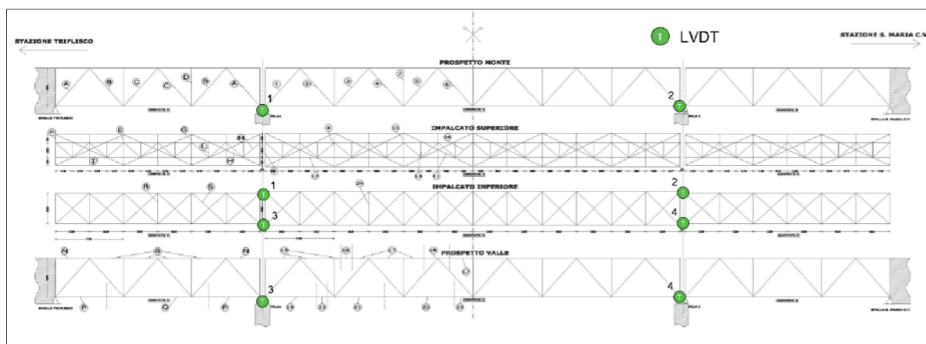


Figure 6.13. Linear variable displacement transducers layout on the Volturno bridge

6.4 Viaduct n.1011

The Viaduct 1011 is an exit ramp located at km. 12+887 of the Naples ring road, specifically at the 'Arena S. Antonio' viaduct (work no. 67), and serves as the exit for the "Vomero" junction. The ramp is supported by pile n.3 of the viaduct and features access ramps consisting of Gerber brackets that support three pre-stressed beams. These beams are connected by crossbeams and an upper slab, and range in length from 18.00 to 20.00 meters, with a roadway width of 7.20 meters. The beams have a height of 1.50 meters from the lower surface of the beam to the upper surface of the slab, with a 0.20-meter thickness. The decks are supported by four reinforced concrete piers of varying heights, which are of rectangular hollow sections. The final deck rests on a reinforced concrete septum abutment, and the foundations are in piles. To provide support between the dapped end and the beams, 20-mm-thick rubber pads are used.

The monitoring system covers two spans of the work, specifically the span between piers 32 and 33 and the span between piers 33 and 33 bis and the piers themselves. The study spans were chosen according to the following criteria: maximum variation in pile height, accessibility. The objective is to monitor the behaviour of a span, through a minimisation of the sensors necessary for the acquisition of key parameters for the evaluation of its global behaviour. The variation in the global properties of the span is an indication of possible "defects"/"anomalies" arising in the time span between two successive measurements. The occurrence of such anomalies can lead to the fielding of different levels of in-depth activities for the detailed analysis and understanding of the problem at hand. Only two spans for this bridge are being studied.



Figure 6.14. Picture of the viaduct n.1011

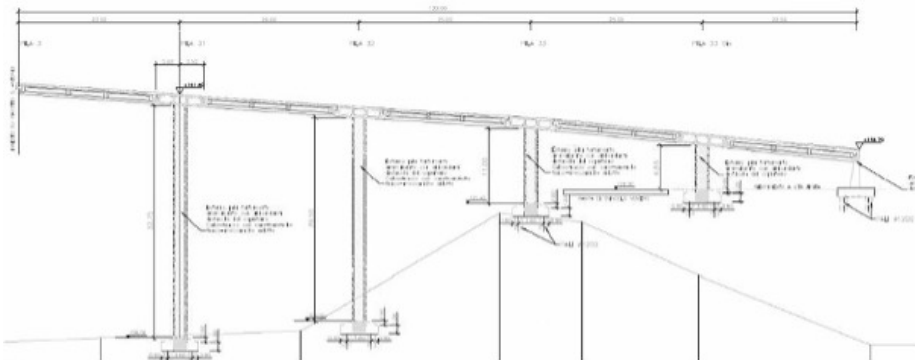


Figure 6.15. Lateral view of the viaduct n.1011

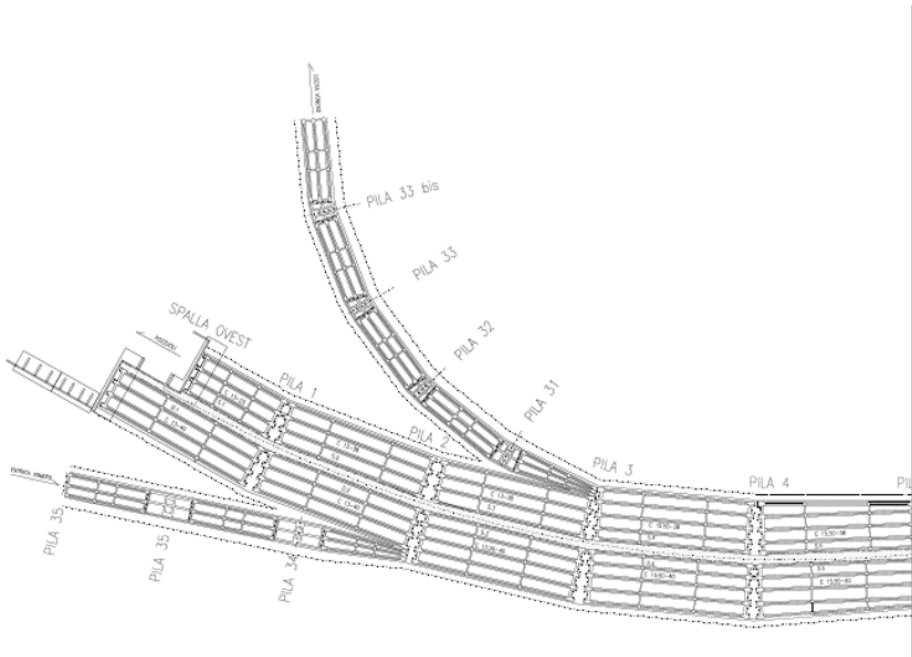
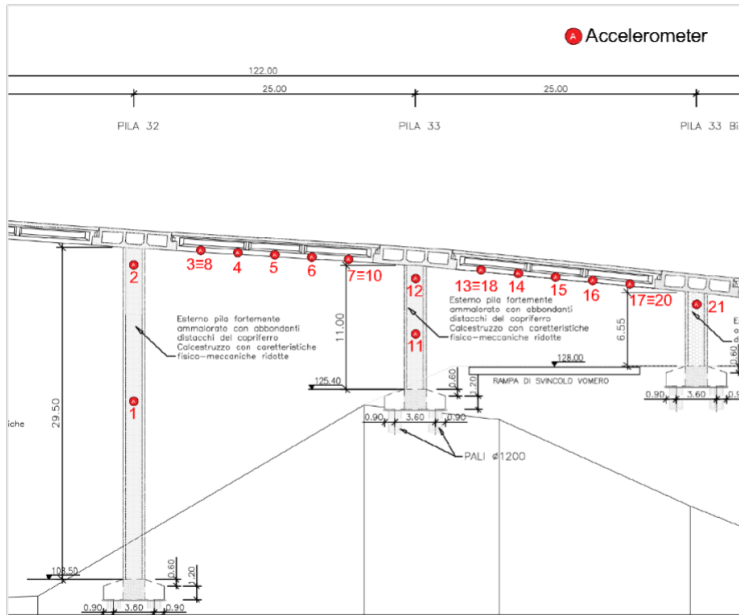
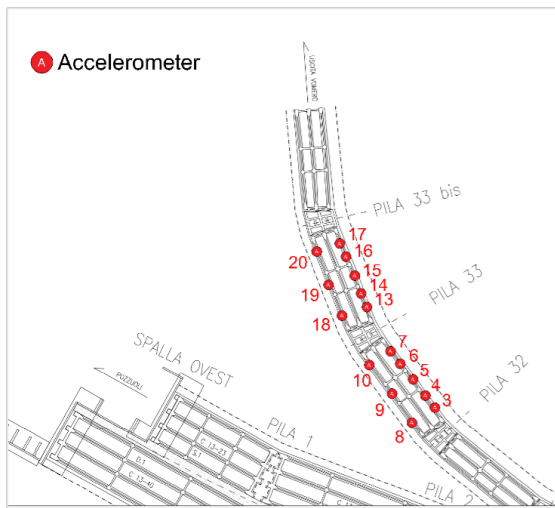


Figure 6.16. Plan view of the viaduct n.1011

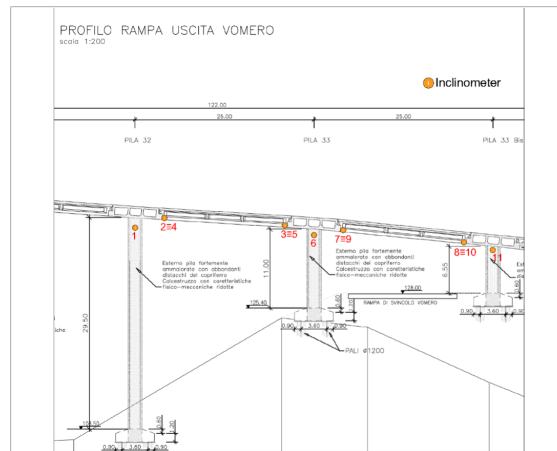


a)

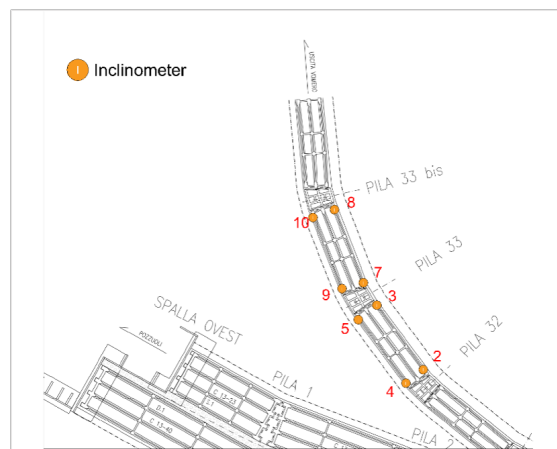


b)

Figure 6.17. Accelerometers layout on the viaduct n.1011 a) lateral view b) plan view



a)

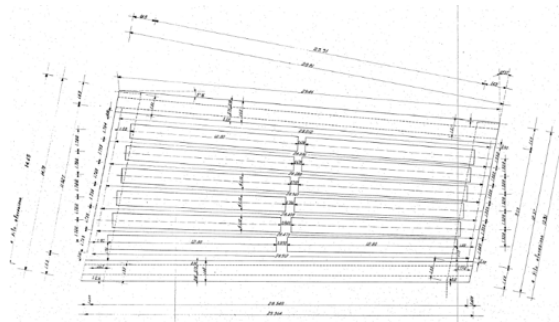


b)

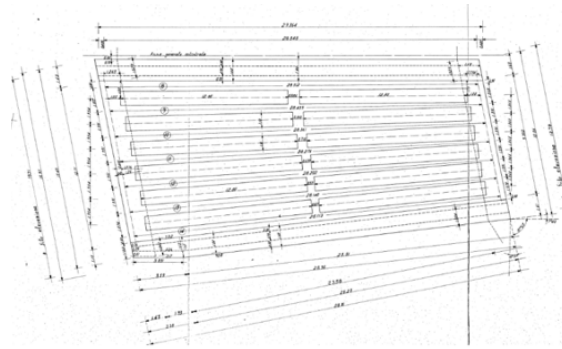
Figure 6.18. Inclinometers layout on the viaduct n.1011 a) lateral view b) plan view

6.5 San Gennaro Viaduct

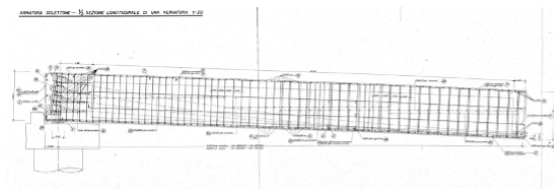
The San Gennaro viaduct is located at km 16+405 of the Naples Bypass, and consists of a supported beam with one span serving two carriageways and two decks. The deck is constructed from a lightened, pre-stressed concrete slab consisting of an upper and a lower slab in pre-stressed reinforced concrete, with pre-stressed concrete ribs placed at variable distances ranging from 1.35 meters to approximately 2 meters. The overall height of the section is 1.53 meters. The floor slabs have a theoretical span that varies slightly between approximately 28.10 meters and 28.50 meters. There are header stringers and an intermediate stringer, and the decks have a variable width of 12.51 to 14.79 meters for the left slab and 12.78 to 15.97 meters for the right slab. The deck is supported by two lateral abutments, which have foundations in piles. The supports are made of neoprene.



a)

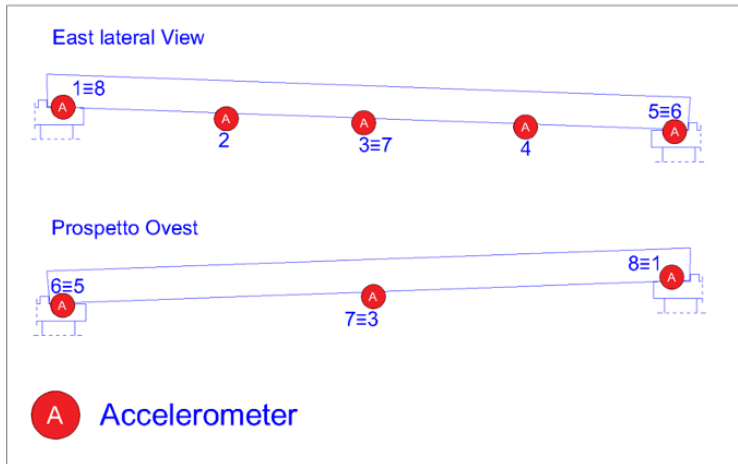


b)

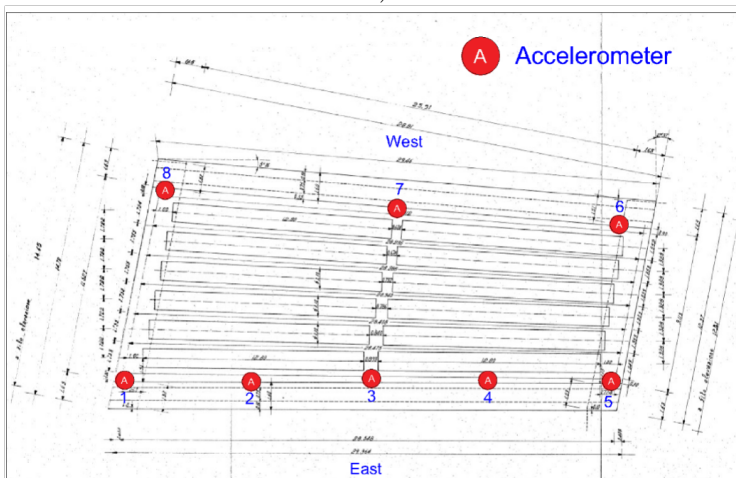


c)

Figure 6.21. Original project excerpts San Gennaro viaduct a) left lane b) right lane c) lateral section

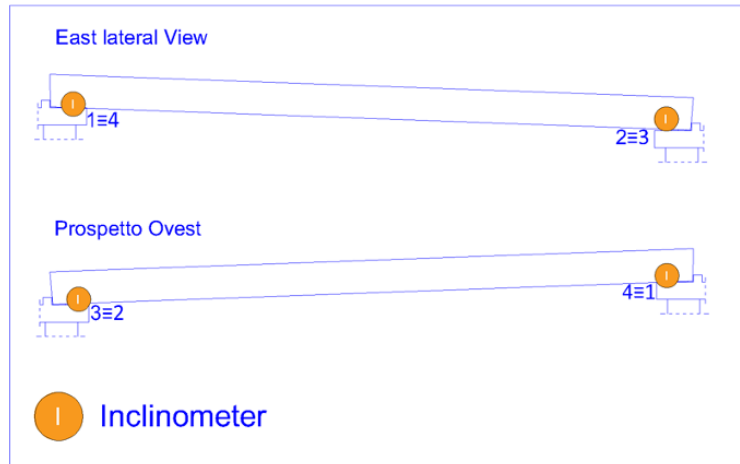


a)

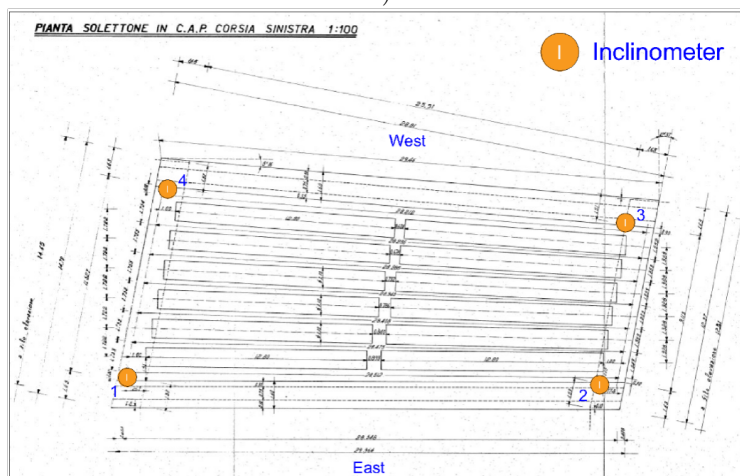


b)

Figure 6.22. Accelerometers layout for San Gennaro viaduct a) lateral view
b) plan view

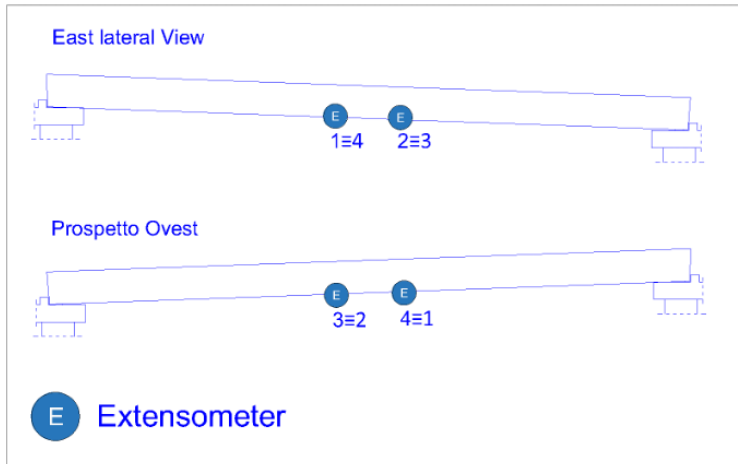


a)

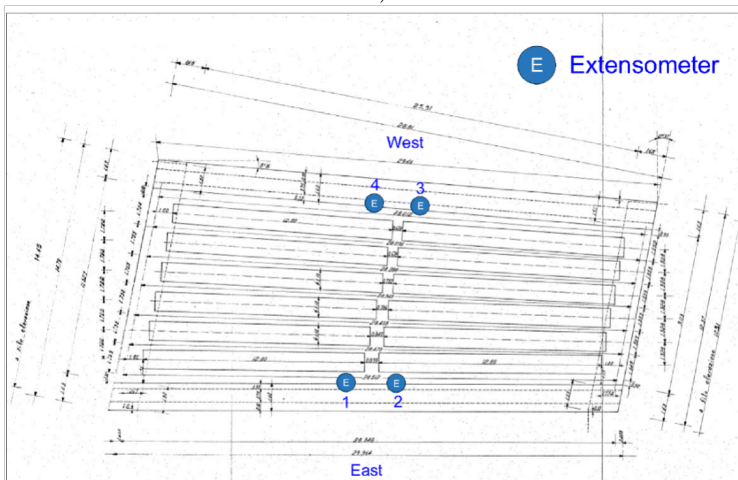


b)

Figure 6.23. Inclinometers layout for San Gennaro viaduct a) lateral view
b) plan view

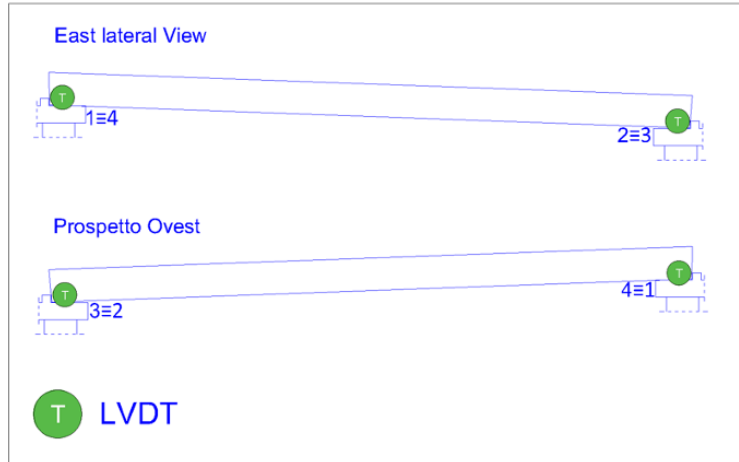


a)

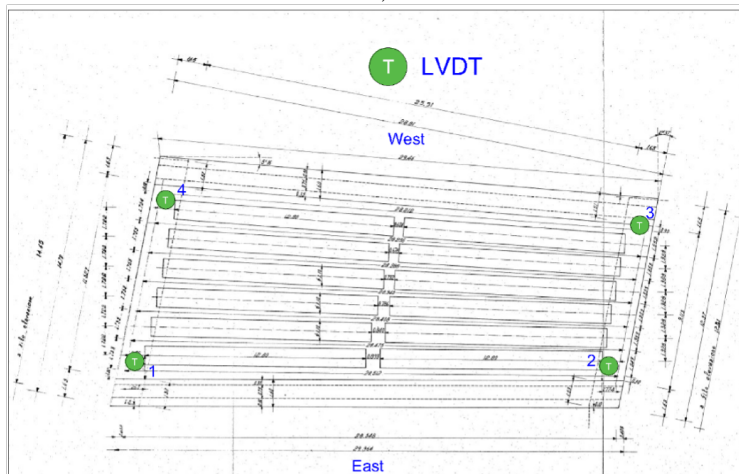


b)

Figure 6.24. Extensometers layout for San Gennaro viaduct a) lateral view
b) plan view



a)



b)

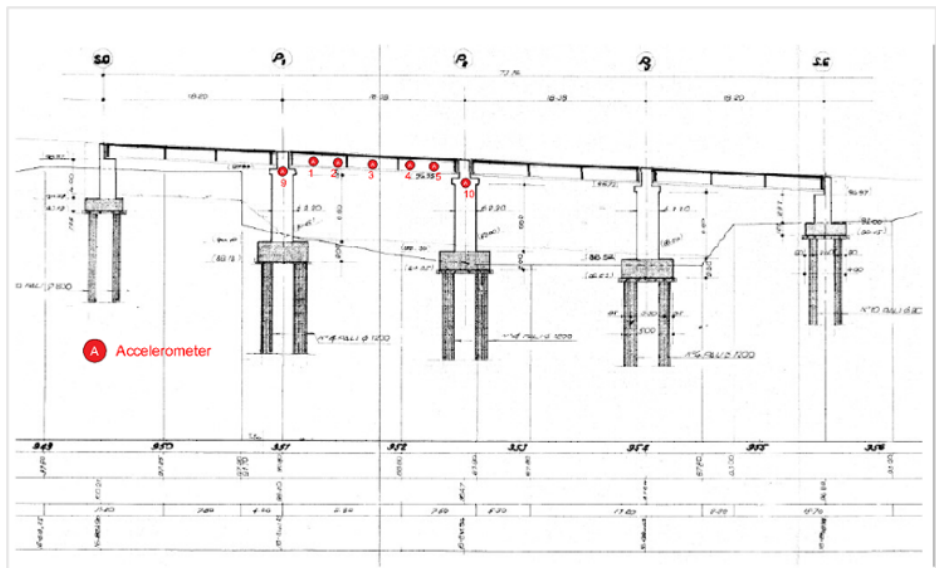
Figure 6.25. LVDTs layout for San Gennaro viaduct a) lateral view b) plan view

6.6 Sant'Eframo viaduct

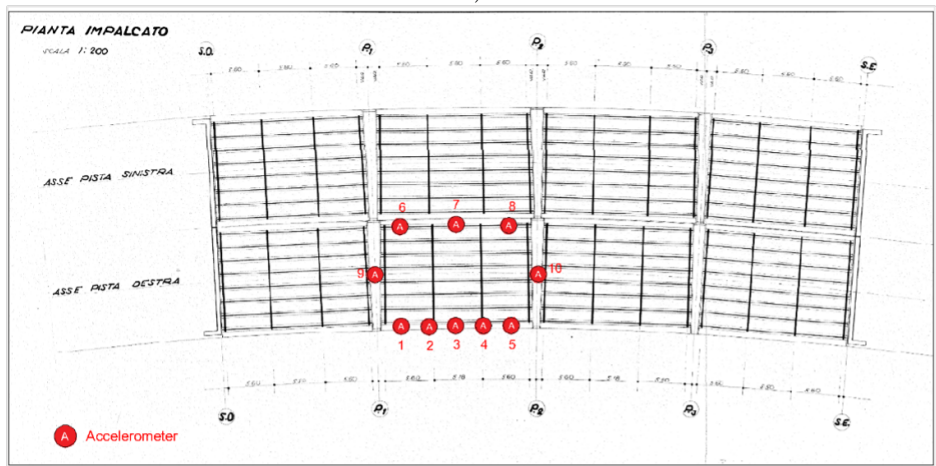
The Sant'Eframo Viaduct is located on the main section of the Naples ByPass (km 17+711), between the Corso Malta and Capodimonte exits. This viaduct is designed as a reinforced concrete simple-supported girder, featuring four spans. The deck consists of eight beams spaced at 1.65 meters and has a height of 1.20 meters. The beams are connected by a 0.20-meter-thick slab, with two crossbeams at the head and two at the span. The theoretical span of the viaduct is 16.90 meters. The elevation structures of the viaduct consist of reinforced concrete circular-section piers which support the deck. The foundations of the viaduct are constructed with plinths on piles. Neoprene pads are used as supports. Currently, only one span of the viaduct is being studied.



Figure 6.26. Picture of Sant'Eframo Viaduct

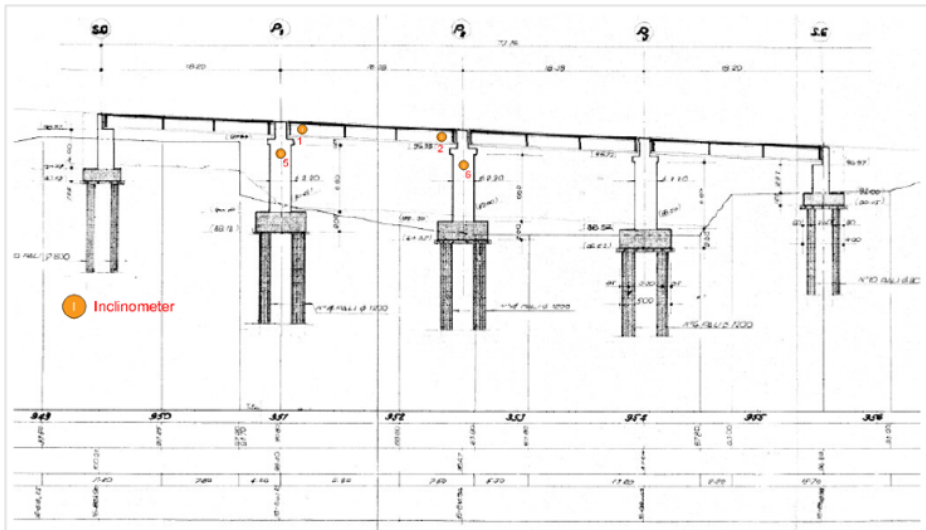


a)

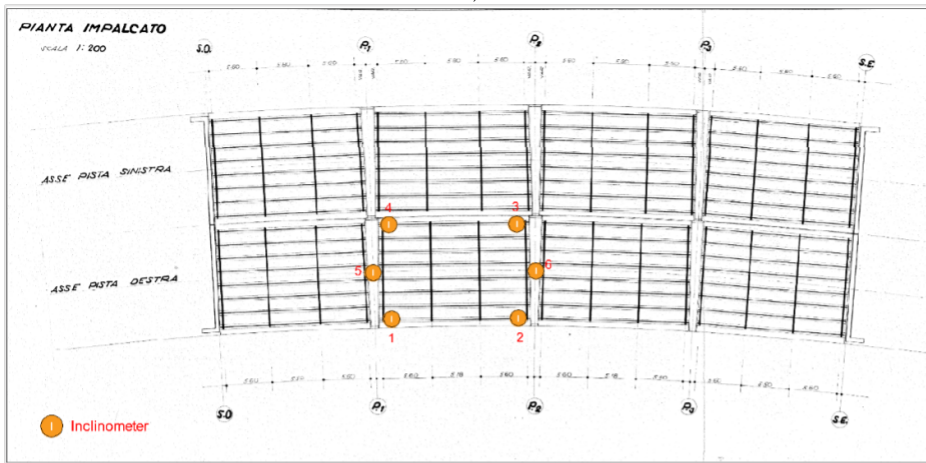


b)

Figure 6.27. Accelerometers layout of Sant'Eframo viaduct a) lateral view
b) plan view.

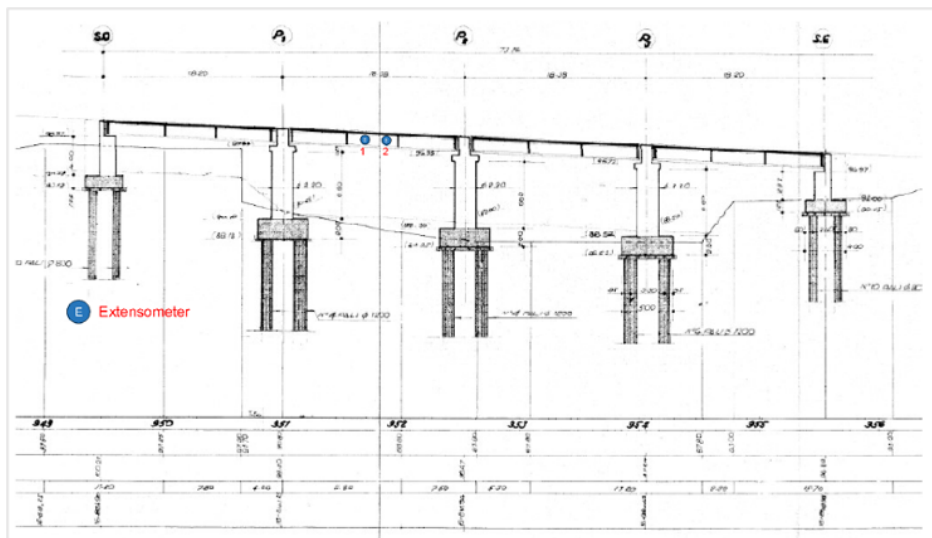


a)

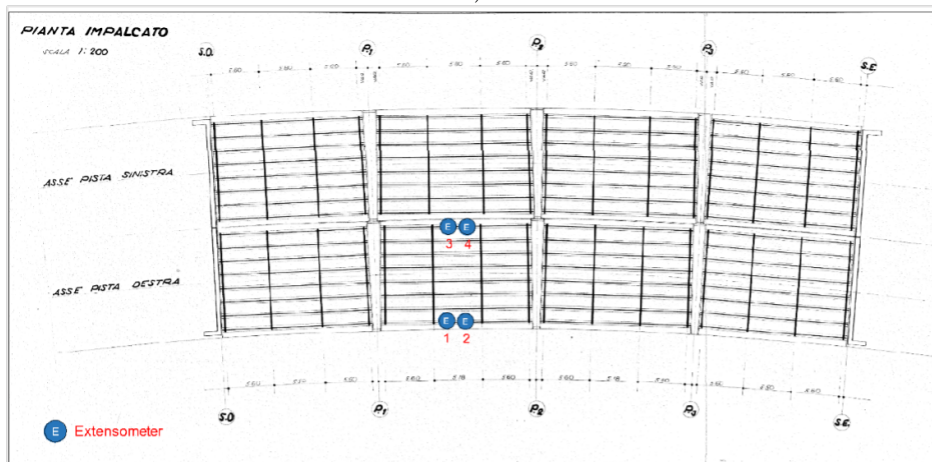


b)

Figure 6.28. Inclinometers layout of Sant'Eframo viaduct a) lateral view b) plan view.

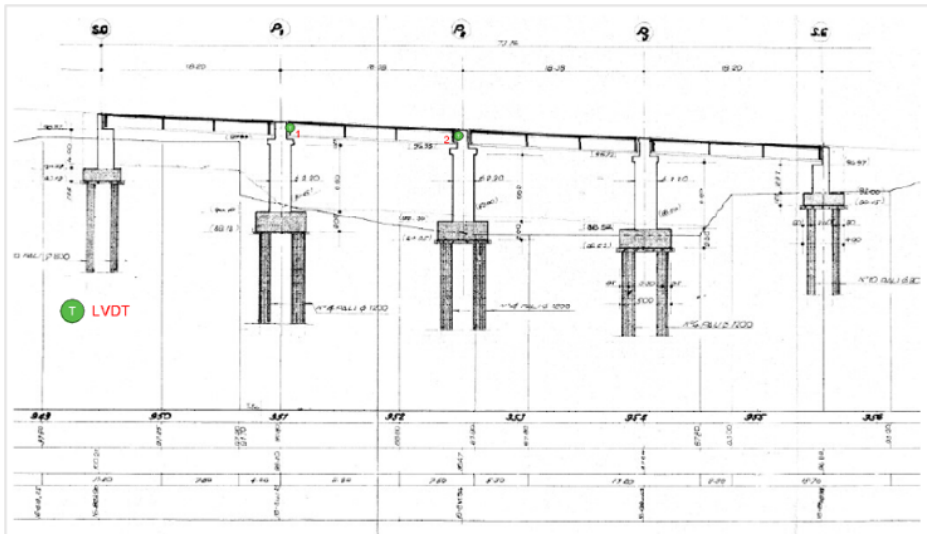


a)

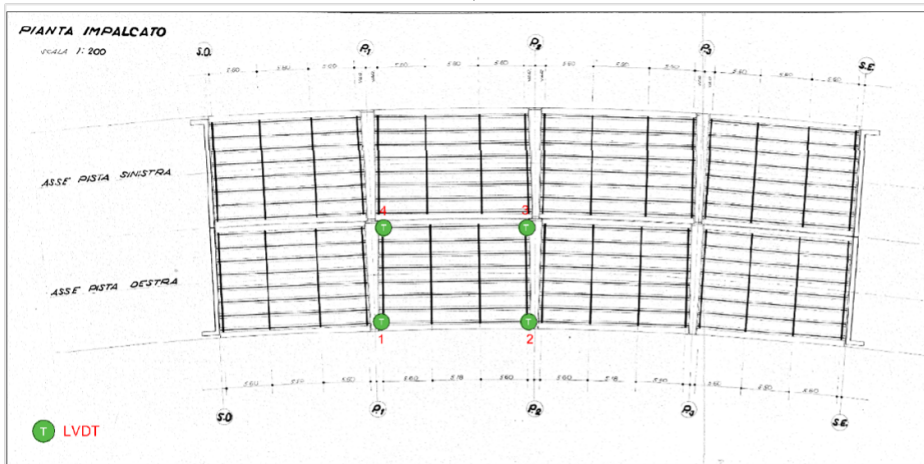


b)

Figure 6.29. Extensometers layout of Sant'Eframo viaduct a) lateral view
b) plan view.



a)



b)

Figure 6.30. LVDTs layout of Sant'Eframo viaduct a) lateral view b) plan view.

6.7 Viaduct n.0080

The "Poggio di Capodimonte" viaduct, identified as viaduct 01.01.0080.0.0, is located at kilometer 16+041 on the Naples Bypass. The viaduct is composed of two joined carriageways. The structure has three spans with a supported girder static scheme.

The decks are made up of a lightened slab, consisting of an upper and lower slab in reinforced concrete and reinforced concrete ribs with pre-stressed cables placed at approximately 1.05 m intervals. The lateral decks have a cross-section height of approximately 1.20 m, while the central deck has a height of 1.50 meters. The net span, from west to east, is as follows:

Span 1 = 13.00 meters

Span 2 = 33.68 meters

Span 3 = 13.09 meters.

The left carriageway is 12.97 meters wide, while the straight right carriageway is 13.50 meters wide. Span 1 is supported by the west pier and a circular section pier in reinforced concrete that is common for both decks. The central span's decks rest on the preceding pier to the west, while each deck to the south rests on a reinforced concrete pier consisting of three columns with a pulvinus on the top. The east decks rest on the previously mentioned piers and a common pier. Currently, only one span of this bridge is being studied.

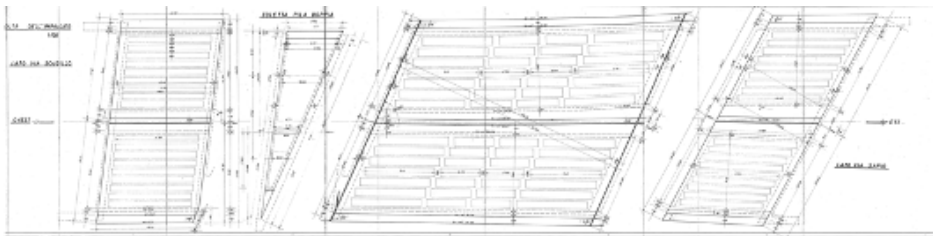


Figure 6.31. Carpentry of the “Poggio di Capodimonte” viaduct.

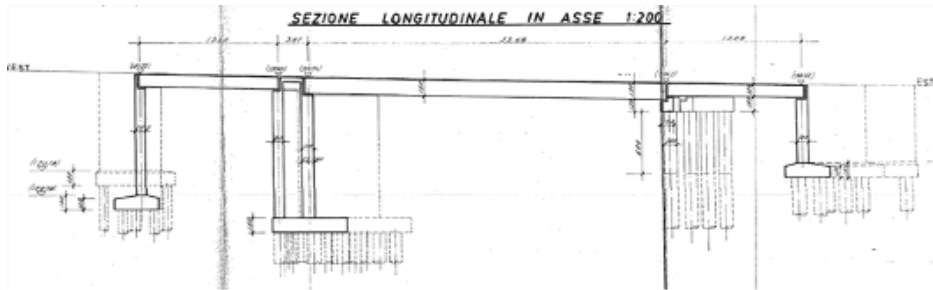
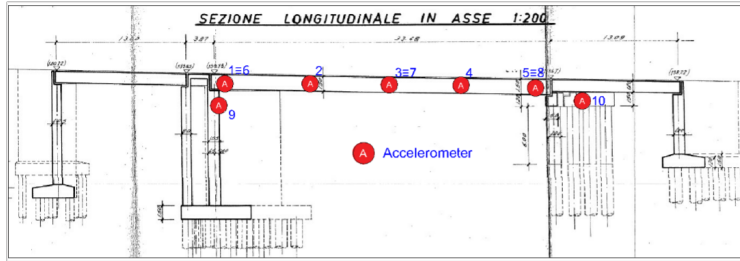


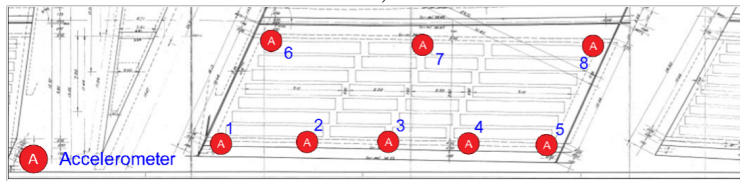
Figure 6.32. Lateral view of the “Poggio di Capodimonte” viaduct.



Figure 6.33. Picture of the “Poggio di Capodimonte” viaduct.

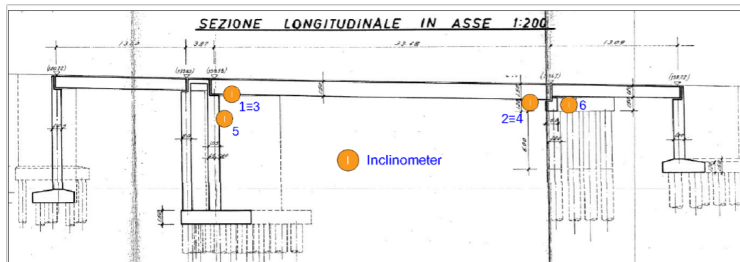


a)



b)

Figure 6.34. Accelerometers layout of the “Poggio di Capodimonte” viaduct
a) lateral view; b) plan view.

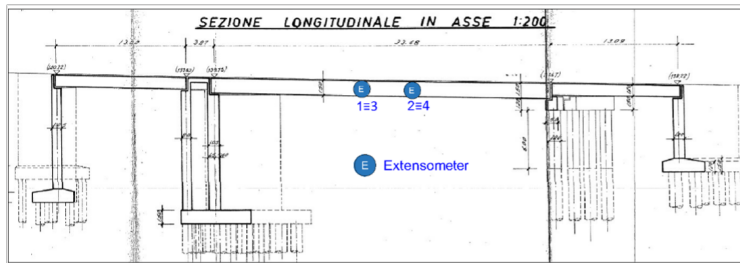


a)

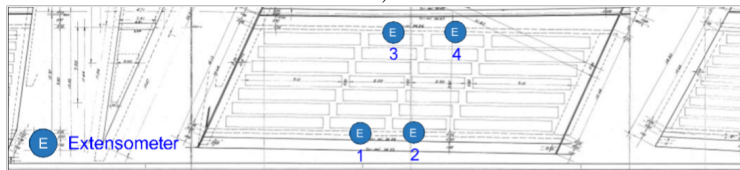


b)

Figure 6.35. Inclinometers layout of the “Poggio di Capodimonte” viaduct
a) lateral view; b) plan view.

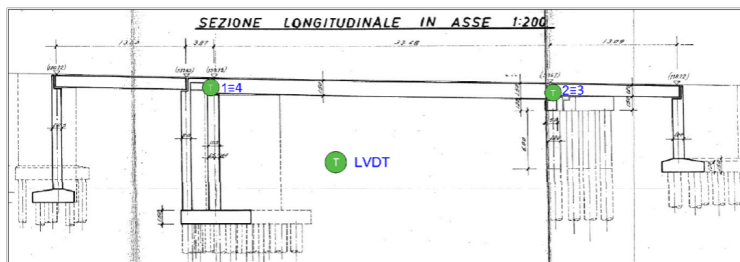


a)

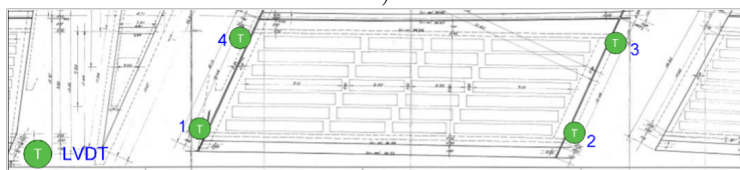


b)

Figure 6.36. Extensometers layout of the “Poggio di Capodimonte” viaduct
a) lateral view; b) plan view.



a)



b)

Figure 6.37. LVDTs layout of the “Poggio di Capodimonte” viaduct a) lateral view; b) plan view.

6.8 Viaduct n.1028

The "Manina" viaduct, identified as viaduct 01.01.1028.0.5, is an overpass located at the entrance junction from Capodichino. The viaduct has a static scheme of a continuous beam on three supports made of reinforced concrete. The net span between supports is 55.30 meters. The deck is composed of a 1.05 m slab, which is lightened by the presence of eight metal tubes that are interrupted approaching to the central support. The space between the tubes forms nine beams that are reinforced with prestressing cables. The deck is completed with a solidification casting. The deck is supported by two piers that are founded on piles, while the central support consists of a cantilever in reinforced concrete.



Figure 6.38. Picture of Viaduct n.1028 "Manina".

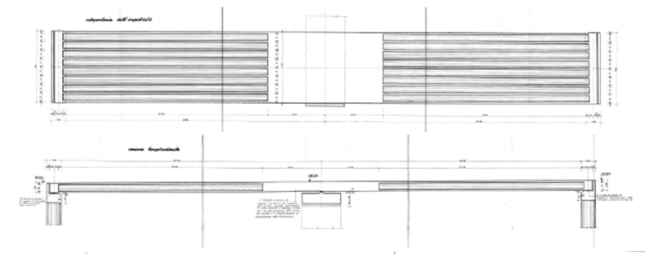


Figure 6.39. Lateral and plan views of viaduct n.1028 "Manina".

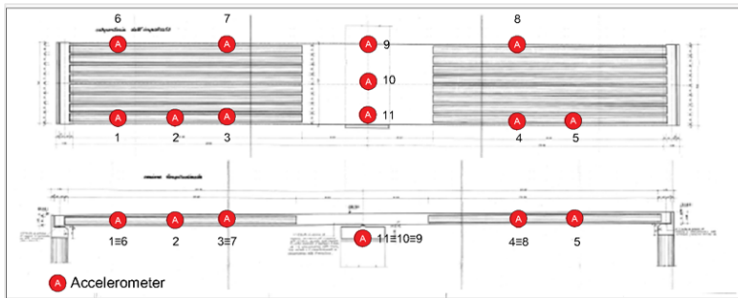


Figure 6.40. Plan and lateral views of the accelerometers layout of the “Manina” viaduct.

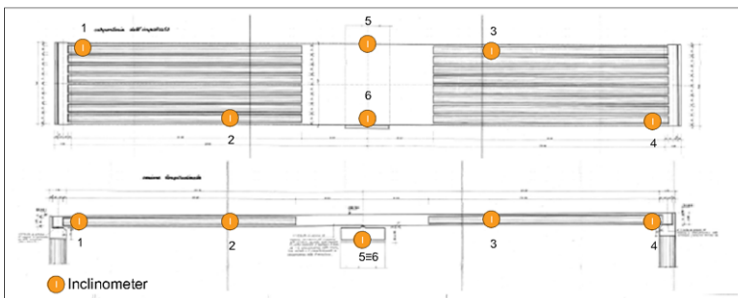


Figure 6.41. Plan and lateral views of the inclinometers layout of the “Manina” viaduct.

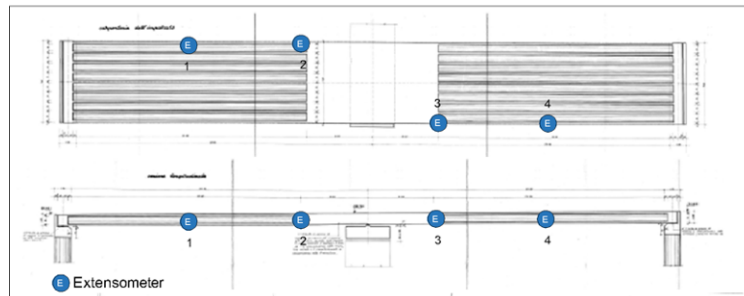


Figure 6.42. Plan and lateral views of the extensometers layout of the “Manina” viaduct.

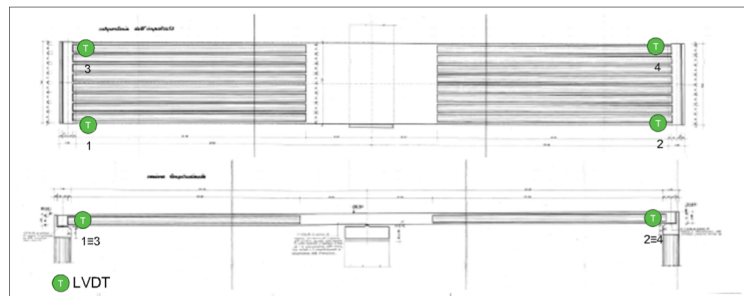


Figure 6.43. Plan and lateral views of the LVDTs layout of the “Manina” viaduct.

6.9 Viaduct n.1026

The viaduct 01.01.1026.0.1, overpass, is located at km 19+000 of the "Tangenziale di Napoli", consists of eleven spans with a static scheme of a simple-supported beam and a steel-concrete composite structure. The deck is composed of a slab with a thickness of 0.25 meters, two beams with a spacing 4.50 meters. The elevated structures are supported by single reinforced concrete pier with a solid circular section. The first span, encountered when proceeding from west to east, is supported by pier n.20 and pier n.21. On pier n. 20, the pulvinus is in common with the old station deck, while the last span rests from pier n.49 to pier D1. The pier caps are in reinforced concrete, with variable sections. The elevated structures are founded on piles.



Figure 6.44. Picture of viaduct n.1026.

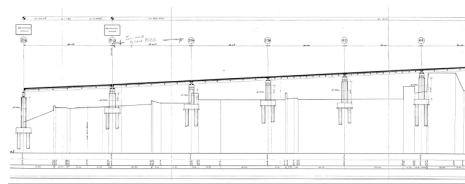


Figure 6.45. Lateral view of viaduct n.1026 from pier n.20 to pier n.44.

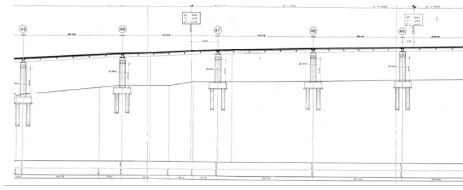


Figure 6.46. Lateral view of viaduct n.1026 from pier n.45 to pier n.49.

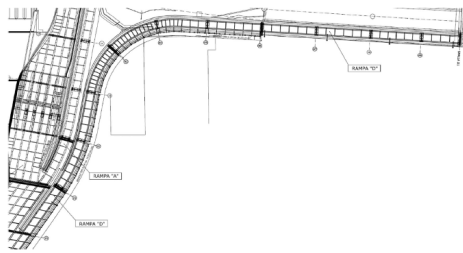
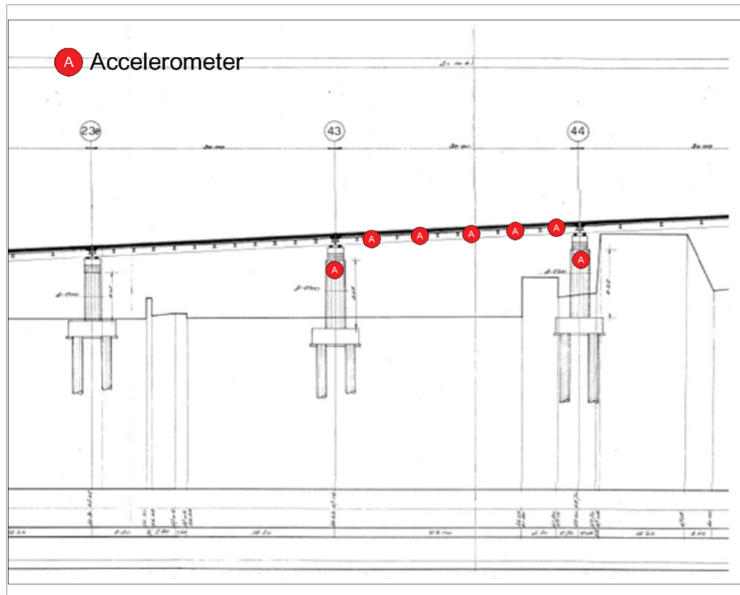


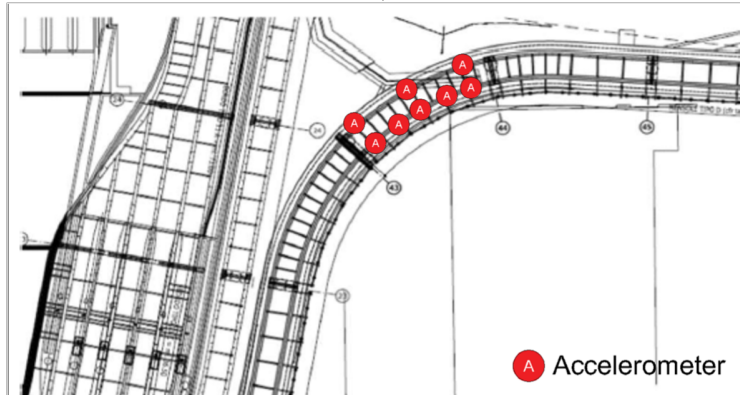
Figure 6.47. Plan view of viaduct n.1026.

6.10 Cassiodoro viaduct

The “Cassiodoro” viaduct consists of 10 spans that have a longitudinal slope of 4.5 percent and transverse slope of 3.8 percent, with a total length of 193 m.

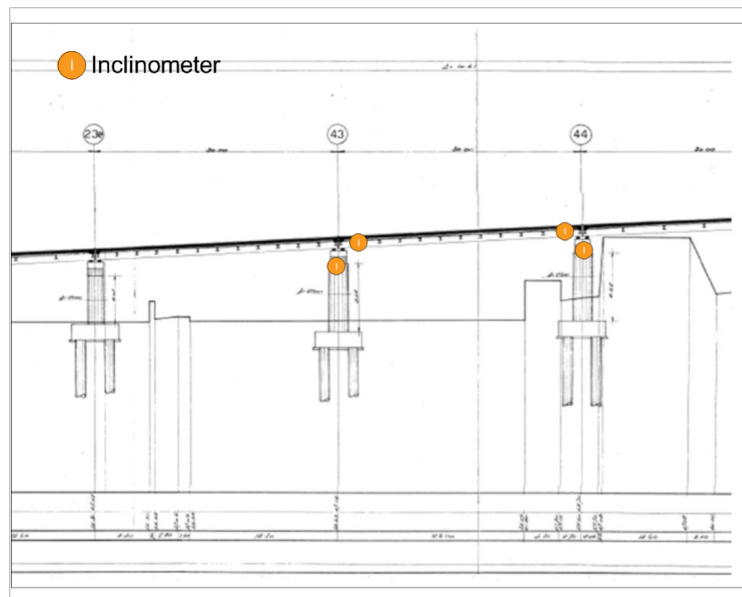


a)



b)

Figure 6.48. Accelerometers layout of viaduct n.1026.(a) lateral view;
(b)plan view

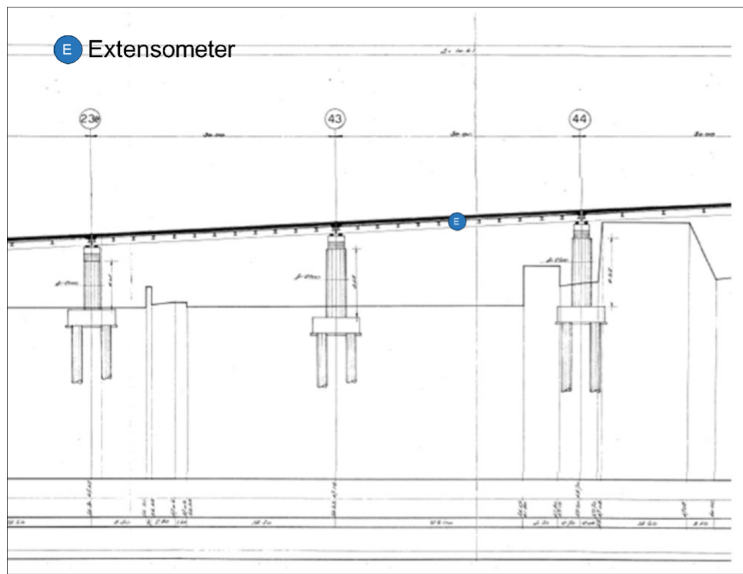


a)



b)

Figure 6.49. Inclinometers layout of viaduct n.1026.(a) lateral view; (b)plan view.

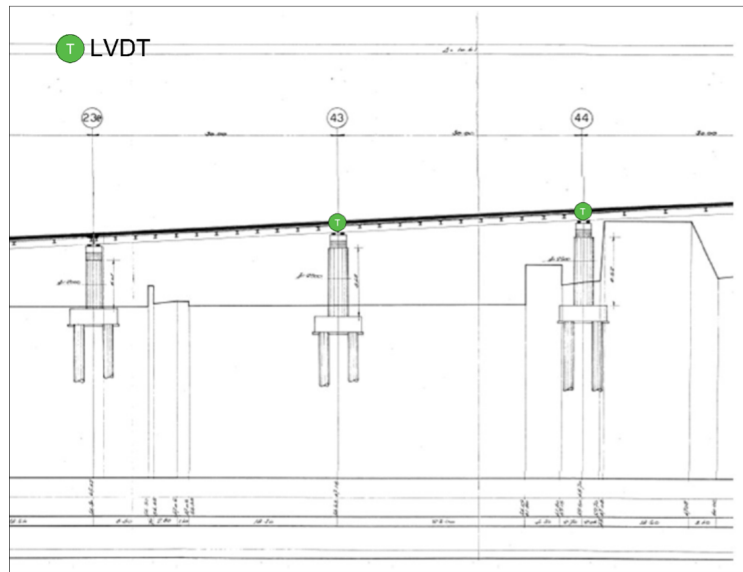


a)

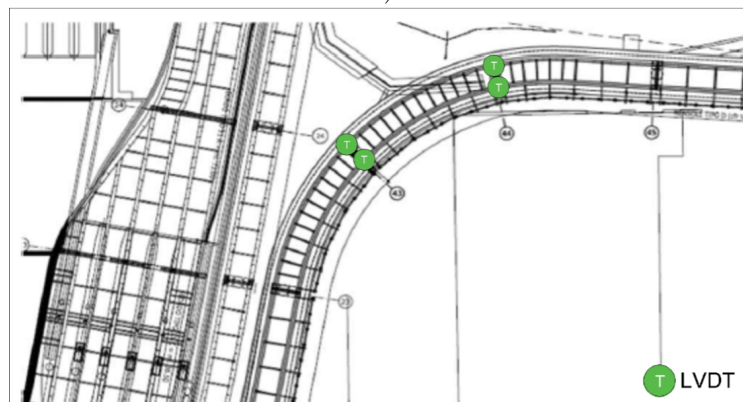


b)

Figure 6.50. Extensometers layout of viaduct n.1026.(a) lateral view; (b)plan view.



a)



b)

Figure 6.51. LVDTs layout of viaduct n.1026.(a) lateral view; (b)plan view.



Figure 6.52. Picture of the “Cassiodoro” viaduct (from Google Earth).

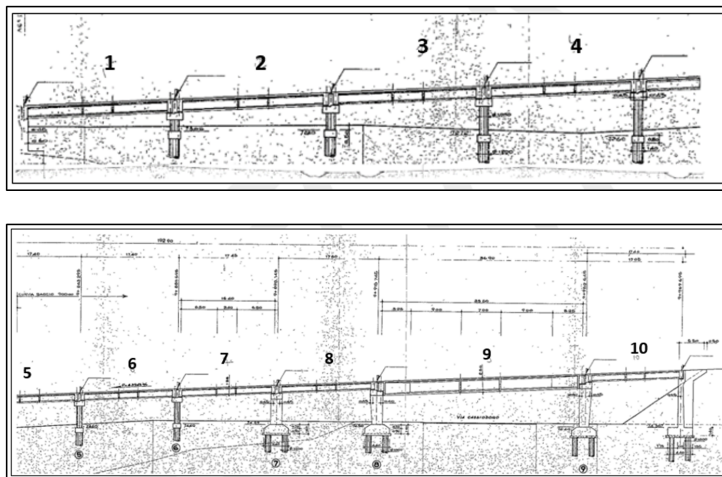


Figure 6.53. Lateral views of the “Cassiodoro” viaduct.

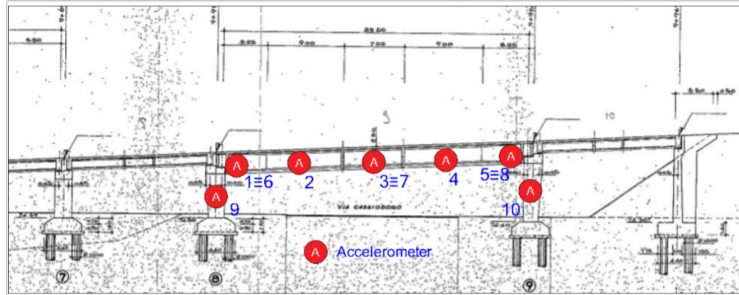


Figure 6.54. Accelerometers layout of the “Cassiodoro” viaduct – lateral view.

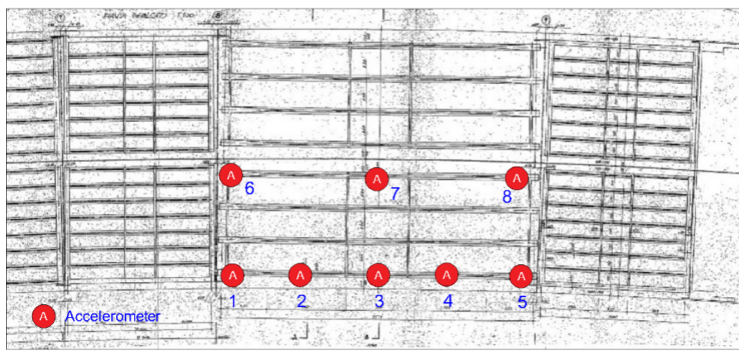


Figure 6.55. Accelerometers layout of the “Cassiodoro” viaduct – plan view.

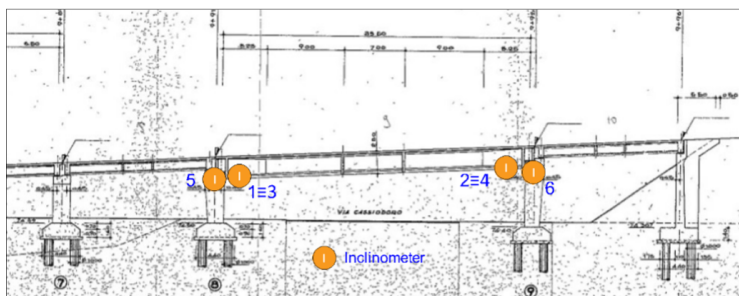


Figure 6.56. Inclinerometers layout of the “Cassiodoro” viaduct – lateral view.

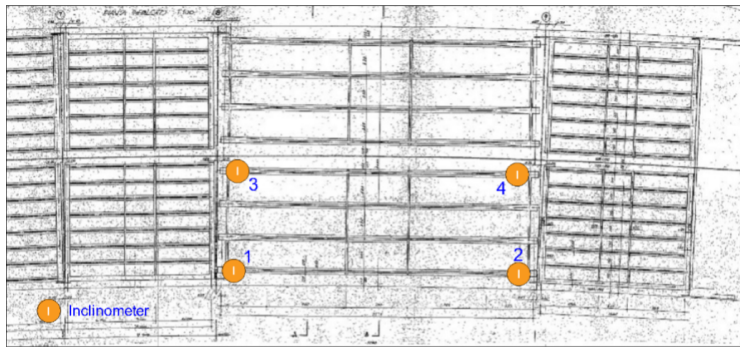


Figure 6.57. Inclinometers layout of the “Cassiodoro” viaduct – plan view

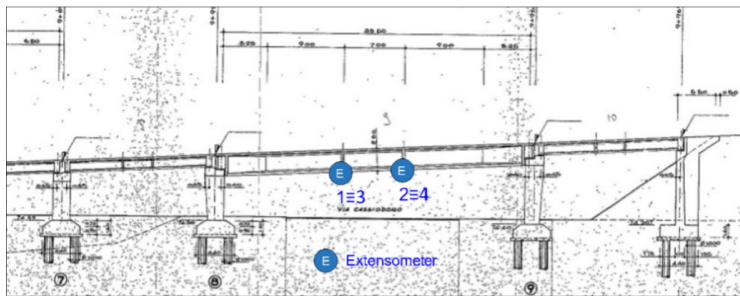


Figure 6.58. Extensiometer layout of the “Cassiodoro” viaduct – lateral view.

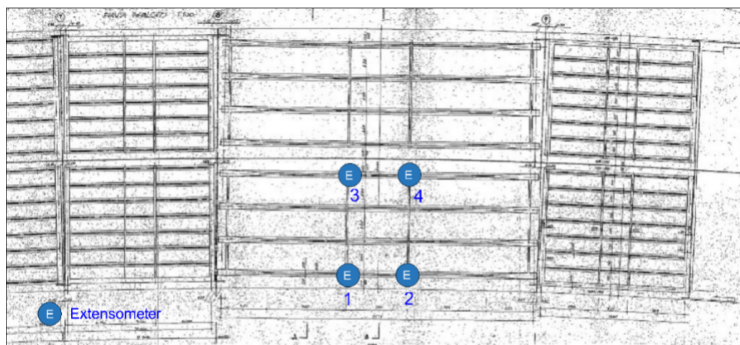


Figure 6.59. Extensiometer layout of the “Cassiodoro” viaduct – plan view.

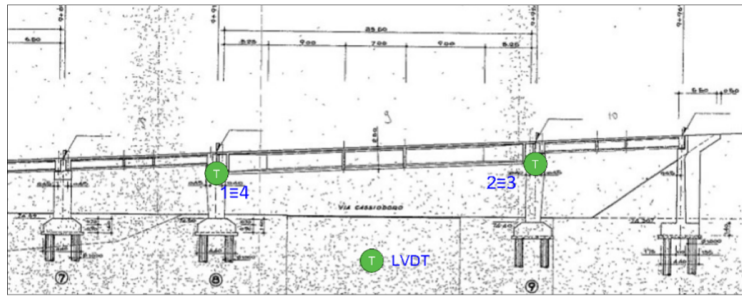


Figure 6.60. LVDTs layout of the “Cassiodoro” viaduct – lateral view.

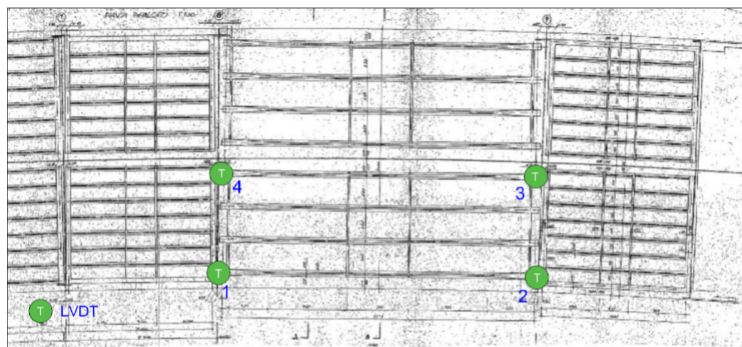


Figure 6.61. LVDTs layout of the “Cassiodoro” viaduct – plan view.

Conclusions

The thesis investigated through experimental and numerical data the variation of modal properties of structures due to seismic damage for damage quantification via SHM. In detail, the study focused on structures with increasing level complexity: RC columns, 2D RC frames and 3D RC buildings. Furthermore, RC bridge piers are also assessed for bridges health monitoring (BHM). Concerning the analysis on RC columns and bridge piers, the following conclusions can be derived:

- The methodological framework herein presented appears a sound technique to correlate the changes in dynamic properties and stiffness of structures in relation with an occurred damage. This system, combined with refined model updating techniques, represents a reliable tool for the damage detection, localization and quantification during long-term SHM;
- The fundamental period elongation can be simulated through sequential pushover-modal analysis on refined FEM model, providing ranges of variation of such DM as a function of the imposed IDR or the damage level. From preliminary results on the investigated dataset of RC columns, the ranges of variation of period elongation showed a large scatter of results and a significant overlap among damage levels, making difficult the clear identification of the level of damage if period elongation is used as DM during SHM. For the dataset of RC columns herein investigated, period elongation less

than 13% is associated to a minor damage, period elongation up to 40% represent a moderate to severe structural damage. Period elongation greater than 40% is associated to severe damage or collapse;

- The ranges of variation of residual drift ratios derived on the dataset for each defined damage levels showed a good agreement with the thresholds and damage levels classification provided by the FEMA 356, confirming the goodness of the damage simulation and of the damage classification adopted for the study. For the dataset under investigation, residual drift greater than 0.2% is associated to a moderate damage. Residual drift greater than 0.8% is associated to severe damage, whereas values of residual drift higher than 2.1% are associated to structural collapse;
- A correlation between seismic damage level, IDRs and lateral stiffness degradation has been derived. This can be useful for seismic damage modelling in sequential analysis (i.e., mainshock-aftershock, earth-quake followed by tsunami). For the dataset of RC columns, a stiffness degradation greater than 22% is associated to a minor damage, while a stiffness degradation greater than 42% indicates a moderate damage level. A stiffness reduction higher than 68% means a severe damage, and degradation greater than 83% is associated with the collapse;
- A good match between the numerical results on lateral stiffness degradation and the empirical model from Di Ludovico et al. [22] is found, attesting the reliability of the methodology in simulating the structural performance and damage under load reversal.

Furthermore, the present thesis reported an assessment of the capacity of vibration based structural health monitoring in providing reliable results in terms of detection of structural damage and estimation of the damage magnitude. Attention has been focused on solid rectangular piers belonging to simply supported bridge systems in order to define a simplified monitoring procedure able to detect and quantify damage based on the measured variations of the fundamental modal properties. The effect of seismic damage of different intensities has been analysed. In order to correlate the changes in the selected damage sensitive features with

the magnitude of damage, experimental quasi-static cyclic tests as well as output-only modal identification tests (in undamaged and damaged configurations) have been carried out on two full-scale specimens. The collected data have been complemented with others available from the literature and used for the calibration and validation of a numerical model able to predict the fundamental natural period elongation as a function of seismic damage level, assuming a flexural failure mode. The refined model has been finally used to carry out extensive probabilistic analyses aimed at defining threshold values for the selected damage features under transverse direction seismic excitation to discriminate between slight or moderate damage, on one hand, and higher damage levels, on the other hand. The proposed methodology appears effective to assess the influence of the seismic damage on the dynamic properties of RC piers in the case of flexural failure modes. It can be noted that seismic damage mainly affects the fundamental natural frequencies while the mode shapes are less sensitive than natural frequencies to structural damage associated to lateral loads. Numerical simulations demonstrated that the higher the natural period increase, ΔT , the higher is damage level increase, and provided a statistical characterization of the typical range of ΔT associated with each damage level. Even though some overlap exists among those ranges, in the absence of more refined analyses they can be addressed as a reference to estimate the magnitude of seismic damage suffered by solid rectangular RC piers in simply supported bridges. As an alternative, the approach adopted in the present study can be applied for a model-based threshold setting at increasing damage level for a given structure: to this aim, the results of quasi-static cyclic tests and the calibrated value of ε_c can be adopted as references. In any case, the thresholds refer to natural period changes resulting from an appropriate compensation of the influence of environmental factors. The study also attests that the costs of the SHM system for simply supported RC bridges can be optimized by installing the sensors only on top of the piers and so doing the variations of the fundamental periods can be tracked. Further work is needed to increase the overall reliability of the results, extending them to different failure modes (i.e., shear, lap-splice) and structural systems to provide a wider definition of threshold values for damage detection and quantification through SHM.

The main outcomes of the study performed on infilled RC frames are

summarised herein:

- OMA output for the first in-plane mode attested that the damage occurred in infill walls at the end of the loading sequences, classified as DL2/DL3, reduced the fundamental frequency of the infilled RC frames by 63-64% with respect to the undamaged configuration;
- For the first out-of-plane mode, OMA records from the two tests show that a DL2 damage to infill walls causes a reduction of fundamental frequency of 19%-23%;
- The undamaged bare frame contributes to 25% of the undamaged infilled frame fundamental frequency for the first in-plane mode and to 77% of the undamaged infilled frame fundamental frequency for the first out-of-plane mode;
- • The FE model has shown to predict with a good accuracy the experimental static and dynamic performance of tested specimens before and after damage, slightly underestimating the experimental fundamental frequencies by 2-10%;
- • The numerical analyses allowed to assess the contribution of structural and non-structural damage to the overall frequency variations. For the tested specimens, frequency variation due to structural damage corresponds to 0.7 Hz for a $PGA=0.669g$.

The results obtained from the analysis of the 3D building show, as expected, a mismatch between the peak and average global damage level, being the average one usually lower than one corresponding to the peak. Ranges of variation of the vibration period are derived for both peak and average global damage levels. Finally, considering the weighted average value of the DL to correlate the vibration period elongation with the Damage Level (DL), the results obtained for the whole building do not match with those derive for the columns. Conversely, a good agreement is observed between the period elongation of single columns and the whole building if the peak damage level is considered. Future studies will look at extending the application of the proposed methodology to a wider dataset of RC buildings with infill walls. Future studies will extend the analysis

to 3D infilled RC frames and will include the effect of openings that significantly affect the overall contribution of infill walls to the variation in modal properties of structures. The second part of the thesis focused on the Bridge Health Monitoring. A proposal of a new architecture for data management has been described and illustrated. It focused on the study, development and implementation of a robust methodology, based on the combined use of information from different monitoring sources, in order to keep structural safety and operability under control with a minimum number of sensors, over time, of the main infrastructure networks of mobility of the Italian territory. Specifically, this methodology is based on the integrated use of advanced products aimed at monitoring the health of strategic mobility infrastructures. The proposed procedures are applicable to entire infrastructure systems, beyond the specific type, and can be part of Civil Protection programs or infrastructure stakeholders, related to the continuous monitoring of the built and risk prevention. The sporadic and limited inspection procedures must be integrated with continuous monitoring systems that can be accessed remotely in real time and automated. In fact, infrastructure maintenance and inspection programs are all the more effective the earlier their ability to detect problematic performance. This is possible, today, with the support of Bridge Health Monitoring (BHM) technologies that aim to continuously monitor the health of the infrastructure, that is, the level of safety. In this thesis, the sensors constituting the monitoring system are analyzed in detail and then discuss the use of sensors for structural monitoring. For each tool, an estimate was made of the local storage space needed for the temporary storage of the data to be processed, and the space occupied by the processed data to be transferred and stored. Through an experimental test on a scale bridge, where a dynamic identification was done and simulated data transmission from a local machine to a remote machine, the feasibility of the methodology was assessed in the lab. Finally, several applications were illustrated that show the main parameter to be monitored, the layout of the instruments chosen for the specific case study, and the indices to be extracted from the time series read by the sensors installed on the structure according with the proposed monitoring system architecture.

Bibliography

- [1] Keith Worden, Charles R. Farrar, Graeme Manson, and Gyuhae Park. The fundamental axioms of structural health monitoring. *Proceedings of the Royal Society A: Mathematical, Physical and Engineering Sciences*, 463:1639–1664, 2007.
- [2] Leandro Iannacone, Pier Francesco Giordano, Paolo Gardoni, and Maria Pina Limongelli. Quantifying the value of information from inspecting and monitoring engineering systems subject to gradual and shock deterioration. *Structural health monitoring*, 21(1):72–89, 2022.
- [3] OS Salawu. Detection of structural damage through changes in frequency: a review. *Engineering structures*, 19(9):718–723, 1997.
- [4] Charles R. Farrar and Keith Worden. An introduction to structural health monitoring. *Philosophical Transactions of the Royal Society A: Mathematical, Physical and Engineering Sciences*, 365:303–315, 2 2007.
- [5] Hoon Sohn. Effects of environmental and operational variability on structural health monitoring. *Philosophical Transactions of the Royal Society A: Mathematical, Physical and Engineering Sciences*, 365:539–560, 2007.
- [6] Bart Peeters and Guido De Roeck. Reference-based stochastic subspace identification for output-only modal analysis. *Mechanical Systems and Signal Processing*, 13:855–878, 1999.
- [7] Rolf G. Rohrmann, Matthias Baessler, Samir Said, Wolfgang Schmid, and Werner F. Ruecker. Structural causes of temperature affected modal data of civil structures obtained by long time monitoring. *Proceedings of the International Modal Analysis Conference - IMAC*, 1:1–7, 2000.
- [8] K. Worden, H. Sohn, and C. R. Farrar. Novelty detection in a changing environment: Regression and inter polation approaches. *Journal of Sound and Vibration*, 258:741–761, 2002.

-
- [9] C. R. Fritzen, G. Mengelkamp, and A. Güemes. Elimination of temperature effects on damage detection within a smart structure concept. *Structural Health Monitoring 2003: From Diagnostics and Prognostics to Structural Health Management - Proceedings of the 4th International Workshop on Structural Health Monitoring, IWSHM 2003*, pages 1530–1538, 2003.
- [10] Jyrki Kullaa. Eliminating environmental or operational influences in structural health monitoring using the missing data analysis. *Journal of Intelligent Material Systems and Structures*, 20:1381–1390, 2009.
- [11] Michael Döhler, Falk Hille, Laurent Mevel, and Werner Rücker. Structural health monitoring with statistical methods during progressive damage test of s101 bridge. *Engineering Structures*, 69:183–193, 2014.
- [12] Anders Rytter. Vibrational based inspection of civil engineering structures. *Fracture and Dynamics*, 1993.
- [13] Paolo Barsocchi, Gianni Bartoli, Michele Betti, Maria Girardi, Stefano Mammolito, Daniele Pellegrini, and Giacomo Zini. Wireless sensor networks for continuous structural health monitoring of historic masonry towers. *International Journal of Architectural Heritage*, 15:22–44, 2021.
- [14] E. T. Whittaker. Xviii.—on the functions which are represented by the expansions of the interpolation-theory. *Proceedings of the Royal Society of Edinburgh*, 35:181–194, 1915.
- [15] Claude E. Shannon. Communication in the presence of noise. *Proceedings of the IEEE*, 72:1192–1201, 1984.
- [16] H. Nyquist. Certain topics in telegraph transmission theory. *Proceedings of the IEEE*, 90:280–305, 2002.
- [17] Keith Worden. Structural health monitoring using pattern recognition. *CISM International Centre for Mechanical Sciences, Courses and Lectures*, 520:183–246, 2010.
- [18] Jerome P Lynch and Kincho H Law. Energy market-based control of linear civil structures. *Proceedings of the US-Korea Workshop on Smart Structural Systems*, pages 23–24, 2002.
- [19] A E Aktan, S K Ciloglu, K A Grimmelman, Q Pan, and F N Catbas. Opportunities and challenges in health monitoring of constructed systems by modal analysis. *International Conference on Experimental Vibration Analysis for Civil Engineering Structures*, 2005.
- [20] Charles Kennedy and C. D. P. Pancu. Use of vectors in vibration measurement and analysis. *Journal of the Aeronautical Sciences*, 14:603–625, 11 1947.
-

-
- [21] Daniel Balaageas, Claus-Peter Frtizen, and Alfredo Guemes. *Structural Health Monitoring*. John Wiley & Sons, Ltd, 2010.
- [22] D. J. Ewins and Z. S. Han. Resonant Vibration Levels of a Mistuned Bladed Disk. *Journal of Vibration, Acoustics, Stress, and Reliability in Design*, 106(2):211–217, 04 1984.
- [23] Peter Cawley and Robert Darius Adams. The location of defects in structures from measurements of natural frequencies. *The Journal of Strain Analysis for Engineering Design*, 14(2):49–57, 1979.
- [24] S W Doebling, C R Farrar, M B Prime, and D W Shevitz. Damage identification and health monitoring of structural and mechanical systems from changes in their vibration characteristics: A literature review. 5 1996.
- [25] E Fol, R Tomás, J Coello De Portugal, and G Franchetti. Detection of faulty beam position monitors using unsupervised learning. *Physical Review Accelerators and Beams*, 23(10):102805, 2020.
- [26] F Casarin and M Modena. Structural assessment and seismic vulnerability analysis of the reggio emilia cathedral, italy. *Proceeding of Structural Analysis of Historical Constructions*, 2006.
- [27] Luís F Ramos. Damage identification on masonry structures based on vibration signatures. 2007.
- [28] Chiara Bedon. Diagnostic analysis and dynamic identification of a glass suspension footbridge via on-site vibration experiments and fe numerical modelling. *Composite Structures*, 216:366–378, 2019.
- [29] Vanni Nicoletti, Davide Arezzo, Sandro Carbonari, and Fabrizio Gara. Vibration-based tests and results for the evaluation of infill masonry walls influence on the dynamic behaviour of buildings: a review. *Archives of Computational Methods in Engineering*, 29(6):3773–3787, 2022.
- [30] A De Sortis, E Antonacci, and F Vestroni. Dynamic identification of a masonry building using forced vibration tests. *Engineering Structures*, 27(2):155–165, 2005.
- [31] Emília Juhásová, Ramiro Sofronie, and Rogerio Bairrao. Stone masonry in historical buildings—ways to increase their resistance and durability. *Engineering Structures*, 30(8):2194–2205, 2008.
- [32] Luís F Ramos, Filippo Casarin, Cristiano Algeri, Paulo B Lourenço, and Claudio Modena. Investigations techniques carried out on the qutb minar, new delhi, india. 2006.
-

-
- [33] D Rinaldis, P Clemente, A De Stefano, et al. Design of seismic arrays for structural systems. In *Structural Health Monitoring and Intelligent Infrastructure-Proceedings of the 2nd International Conference on Structural Health Monitoring of Intelligent Infrastructure, SHMII 2005*, volume 2, pages 1447–1453, 2006.
- [34] Maria Rosa Valluzzi, Maurizio Valdemarca, and Claudio Modena. Behavior of brick masonry vaults strengthened by frp laminates. *Journal of composites for construction*, 5(3):163–169, 2001.
- [35] Bijaya Jaishi, Wei-Xin Ren, Zhou-Hong Zong, and Prem Nath Maskey. Dynamic and seismic performance of old multi-tiered temples in nepal. *Engineering Structures*, 25(14):1827–1839, 2003.
- [36] Carmelo Gentile and A Saisi. Ambient vibration testing of historic masonry towers for structural identification and damage assessment. *Construction and building materials*, 21(6):1311–1321, 2007.
- [37] Maurice S Bartlett. Smoothing periodograms from time-series with continuous spectra. *Nature*, 161(4096):686–687, 1948.
- [38] Peter Welch. The use of fast fourier transform for the estimation of power spectra: a method based on time averaging over short, modified periodograms. *IEEE Transactions on audio and electroacoustics*, 15(2):70–73, 1967.
- [39] Bart Peeters and Guido De Roeck. Reference-based stochastic subspace identification for output-only modal analysis. *Mechanical systems and signal processing*, 13(6):855–878, 1999.
- [40] Rune Brincker, Lingmi Zhang, and Palle Andersen. Output-only modal analysis by frequency domain decomposition. In *Proceedings of ISMA25: 2000 International Conference on Noise and Vibration Engineering*, pages 717–723. Katholieke Universiteit, Leuven, 2000.
- [41] Carlo Rainieri and Giovanni Fabbrocino. Operational modal analysis of civil engineering structures. *Springer, New York*, 142:143, 2014.
- [42] Bart Peeters, Herman Van der Auweraer, et al. Polymax: a revolution in operational modal analysis. In *Proceedings of the 1st International Operational Modal Analysis Conference, Copenhagen, Denmark*, volume 820, pages 1–12, 2005.
- [43] Young-Ji Park, Alfredo H-S Ang, and Yi Kwei Wen. Seismic damage analysis of reinforced concrete buildings. *Journal of Structural Engineering*, 111(4):740–757, 1985.
-

-
- [44] Marta Del Zoppo, Marco Di Ludovico, Alberto Balsamo, and Andrea Prota. Comparative analysis of existing rc columns jacketed with cfrp or frcc. *Polymers*, 10(4):361, 2018.
- [45] Donatello Cardone and Giuseppe Perrone. Developing fragility curves and loss functions for masonry infill walls. *Earthquakes and Structures*, 9(1):257–279, 2015.
- [46] M Di Ludovico, GM Verderame, A Prota, G Manfredi, and E Cosenza. Cyclic behavior of nonconforming full-scale rc columns. *Journal of Structural Engineering*, 140(5):04013107, 2014.
- [47] Frank McKenna and Gregory L Fenves. The opensees command language manual. *University of California, Berkeley (opensees. ce. berkeley. edu)*, 2001.
- [48] T Paulay and MJN Priestly. Structural walls. *Seismic design of reinforced concrete and masonry building*, pages 362–499, 1992.
- [49] Dudley Charles Kent and Robert Park. Flexural members with confined concrete. *Journal of the structural division*, 97(7):1969–1990, 1971.
- [50] Jian Zhao and Sri Sritharan. Modeling of strain penetration effects in fiber-based analysis of reinforced concrete structures. *ACI structural journal*, 104(2):133, 2007.
- [51] R Tefpers, Z Achillides, A Azizinamini, G Balázs, AB Vliet, J Cabrera, J Cairns, et al. Bond of reinforcement in concrete. *Lausanne: Fib*, 2000.
- [52] FEDERAL EMERGENCY FEMA 356 et al. Prestandard and commentary for the seismic rehabilitation of buildings. *Federal Emergency Management Agency, Washington, DC*, 2000.
- [53] M. Di Ludovico, Maria Polese, Marco Gaetani d’Aragona, Andrea Prota, and Gaetano Manfredi. A proposal for plastic hinges modification factors for damaged rc columns. *Engineering Structures*, 51:99–112, 06 2013.
- [54] C Del Vecchio, M Di Ludovico, GM Verderame, and A Prota. Pseudodynamic tests on full-scale two storeys rc frames with different infill-to-structure connections. *Engineering Structures*, 266:114608, 2022.
- [55] Maria Teresa De Risi, Paolo Ricci, and Gerardo M Verderame. Modelling exterior unreinforced beam-column joints in seismic analysis of non-ductile rc frames. *Earthquake Engineering & Structural Dynamics*, 46(6):899–923, 2017.
-

-
- [56] CZ Chrysostomou, Nicholas Kyriakides, Panagiotis Kotronis, and Elpida Georgiou. Derivation of fragility curves for rc frames retrofitted with rc infill walls based on full-scale pseudodynamic testing results. In *ECCOMAS Congress 2016*, 2016.
- [57] TB Panagiotakos and MN Fardis. Seismic response of infilled rc frames structures. In *11th world conference on earthquake engineering*, volume 23, page 28, 1996.
- [58] Gerardo M Verderame, Paolo Ricci, Maria Teresa De Risi, and Carlo Del Gaudio. Experimental assessment and numerical modelling of conforming and non-conforming rc frames with and without infills. *Journal of Earthquake Engineering*, 26(2):573–614, 2022.
- [59] Alessandro Lubrano Lobianco, Marta Del Zoppo, and Marco Di Ludovico. Seismic damage quantification for the shm of existing rc structures. In *Civil Structural Health Monitoring: Proceedings of CSHM-8 Workshop*, pages 177–195. Springer, 2021.
- [60] MJ Nigel Priestley, Frieder Seible, and Gian Michele Calvi. *Seismic design and retrofit of bridges*. John Wiley & Sons, 1996.
- [61] María O Moroni, Ruben Boroschek, and Mauricio Sarrazin. Dynamic characteristics of chilean bridges with seismic protection. *Journal of Bridge Engineering*, 10(2):124–132, 2005.
- [62] Nicolas A Londono. *Use of vibration data for structural health monitoring of bridges*. PhD thesis, Carleton University, 2006.
- [63] CARLO Rainieri, DANILO Gargaro, GIOVANNI Fabbrocino, G Maddaloni, L Di Sarno, ANDREA Prota, and Giuseppe Manfredi. Shaking table tests for the experimental verification of the effectiveness of an automated modal parameter monitoring system for existing bridges in seismic areas. *Structural Control and Health Monitoring*, 25(7):e2165, 2018.
- [64] Yozo Fujino, Dionysius M. Siringoringo, Yoshiki Ikeda, Tomonori Nagayama, and Tsukasa Mizutani. Research and implementations of structural monitoring for bridges and buildings in japan. *Engineering*, 5(6):1093–1119, 2019.
- [65] Jaime Hernandez Jr, Takeshi Miyashita, Hironori Ishii, Phouthaphone Vorabouth, and Yozo Fujino. Identification of modal characteristics of shinkansen rc viaducts using laser doppler vibrometers. 2006.
- [66] Claudia Zelaschi, Ricardo Monteiro, and Rui Pinho. Parametric characterization of rc bridges for seismic assessment purposes. *Structures*, 7:14–24, 08 2016.
-

-
- [67] Camilo Perdomo and Ricardo Monteiro. Extension of displacement-based simplified procedures to the seismic loss assessment of multi-span rc bridges. *Earthquake Engineering & Structural Dynamics*, 50(4):1101–1124, 2021.
-

